Incorporation of metal (silver, copper, iron) chalcogenides (oxide, selenide) nanoparticles into poly(methyl methacrylate) fibers for their antibacterial activity

BY

SIMON BONGINKOSI SIBOKOZA

STUDENT NUMBER: 211080837

MTech: CHEMISTRY

THESIS SUBMITTED IN PARTIAL FULFILMENT OF THE REQUIREMENT FOR THE DEGREE TECHNOLOGIAE DOCTORIS IN THE FACULTY OF APPLIED AND COMPUTER SCIENCES AT VAAL UNIVERSITY OF TECHNOLOGY

PROMOTER : PROF M.J. MOLOTO

CO-PROMOTER (1) : PROF N. MOLOTO

CO-PROMOTER (2) : PROF F. MTHUNZI

ACADEMIC YEAR 2020

Declaration statement

I the undersigned solemnly declare that the project “Incorporation of metal (silver, copper, iron) chalcogenides (oxide, selenide) nanoparticles into poly(methyl methacrylate) fibers for their antibacterial activity.” is based on my work done under the supervision of Professor MJ Moloto during the study. I would like to endorse that the work done is original and has not been submitted to any other institution for any other degree or diploma or certificate. Furthermore, all the material used from other sources is acknowledged and their full details are given in the references.

S.B. Sibokoza (211080837)

……Date: ……...

Supervisor: Prof M.J. Moloto

……Date: …….

Acknowledgements

Great thanks to God almighty for the gift of life and all the provision. I would like to pass my gratitude to my supervisors Prof M.J., Prof N. Moloto, and Prof F Mthunzi for their guidance, motivation and support. I would also like to thank them for the opportunities they presented to me, that helped me in so many ways. Special thanks go to the NCAP group members, and all my friends. My heartfelt gratitude goes to my family: parents and siblings. I cannot find words that can express how important you are to my life.

I am grateful of Vaal University of Technology for allowing me to do my studies at your premises. Sincere thanks to Wits University, and Mintek for allowing me to use their facilities for characterization of the samples of the study. I would also like to thank VUT (Hub and Spokes funding) and NRF for their financial support.

List of abbreviation

Symbols and constant

a	lattice spacing
a.u.	arbitrary unites
°C	degree celsius
cm	centimetre
d	diameter
e	elemental charge
E	energy
E_g	band gap energy
eV	electron volts
h	Planck’s constant
h	hour
m^*	effective mass
nm	nanometer
QDs	quantum dots
R	radius
s	seconds
T	temperature
t	time
a_B	Bohr radius
ε	dielectric constant
λ_{exc}	excitation wavelength
ν	frequency

Instrumentation

FT-IR	Fourier transform infrared
PL	Photoluminescence
TEM	Transmission electron microscopy
TGA	Thermogravimetric analysis
XRD	X-ray diffraction
SEM	Scanning electron microscopy
Uv-Vis	Ultraviolet-visible spectroscopy

Chemical reagents

PMMA	poly(methyl methacrylate)
TOP	tri-n-octylphosphine
MSe	metal selenide
MO	metal oxide
HDA	hexadecylamine
INT	p-iodonitrotetrazolium chloride
DMF	dimethylformamide
M	molecular weight of the polymer
CFU	colony forming unit
IUPAC	International Union of Pure and Applied Chemistry
PEO	poly(ethylene oxide)
PVP	poly(vinylpyrrolidone)
MC	methylene chloride
PVA	poly(vinyl alcohol)
HA	hyaluronic acid
CS	chistosan

CA	cellulose acetate
PLDLA	poly(L-lactide-co-D, L-lactide)
DCM	dichloromethane
PAN	poly(acrylonitrile)
DMSO	dimethyl sulfoxide
ACY	acyclovir
PS	polystyrene
PVAc	poly(vinyl acetate)
PCL	polycaprolactone
PLGA	poly(lactic-co-glycolic acid)

Abstract

Nanoscience receives a lot of attention in the 21 century and is one of the most advancing technology in our days. It provides many new and advanced technological opportunities. This field involves many disciplines which include chemical, physical, and biological related fields. The advancement of nanoscience makes life to be better and bring about new inventions which can solve many problems in our day to day life. Although there are reservations about the use of these materials in other fields. Some researchers believe that these materials can be a problem to the environment and humanity at large. Therefore, more research needs to be done to fully understand these materials. Polymer science is another field that has been advancing every day. Many problems in our lives require material which have properties from nanomaterials and polymers. The combination of these technologies can leads to new materials which have many possibilities in solving most problems. Some researchers have taken advantage of these two powerful fields and merge them. There has been a lot of work done that involves combination of nanotechnology and polymer science.

The current project is an initiative to manufacture nanofibers. These fibers are prepared using polymer solution mixed with metal oxide and metal selenide nanomaterials. The polymer solution is incorporated with nanoparticles and electrospunned to make nanofibers. The electrospinning afford the material prepared to be at nanoscale. The fact that the material formed is at nanoscale opens many possibilities to be used in various fields. The study is about fabrication of polymer nanofibers embedded with metal chalcogenide nanoparticles. The metal oxide and metal selenide nanoparticles were prepared using complexes. These complexes contain both the metal and the chalcogenide of interest. The complexes are prepared from oxygen-based (urea), and selenium-based (diphenyldiselenide) ligands. The urea complexes co-ordinates with metal using oxygen for iron, however in silver complexes both nitrogen and oxygen are used. These complexes allow easy control of reaction parameters, and thermal decomposes to form metal oxide, metal selenide, and metal. The complexes are very stable and decomposes at about 200 °C. These compounds are thermal decomposed to form metal chalcogenides, and metal nanoparticles. The complexes are characterized with FTIR, TGA, and elemental analysis.

The metal chalcoginedes (copper oxide, iron oxide, silver oxide, copper selenide, iron selenide, and silver selenide) nanoparticles were prepared using thermal decomposition of a single source (complexes or metal salts). The prepared chalcogenides nanoparticles have good absorption and emission properties consistent with small sizes. These nanoparticles are composed of various phased and stoichiometry. Some metal chalcogenides have a mixture of stoichiometry and phase. The metal chalcogenides nanoparticles are dominated by spheres, and other shapes such as rods. These metal chalcogenides have a particles size in the range of 1-36 nm. The metal chalcogenides nanoparticles were tested against bacteria and fungi. These nanoparticles show highest activity in gram positive compared to gram negative bacteria. Metal oxide nanoparticles show the highest activity compared to metal selenide. All the metal chalcogenides show the highest against fungi. The nanoparticles are able to inhibit the fungi at lowest concentration. The nanoparticles are characterized with various instruments which includes UV-Vis, PL, XRD, and TEM.

Nanofibers of poly(methyl methacrylate) (PMMA) incorporated with metal selenide and metal oxide nanoparticles were prepared by electrospinning. The nanofibers incorporated with metal chalcogenide are more thermal stable than PMMA nanofibers. Therefore, incorporation of metal chalcogenides nanoparticles leads to more thermal stability nanofibers. The PMMA are coordinated to the metal oxide and metal selenide through carbonyl oxygen atom. The PMMA incorporated with metal oxide and metal selenide leads to the formation of nanofibers with uneven surface with a diameter in the range of 30 to 200 nm. The prepared fibers are characterized using FTIR, TGA, SEM.

Presentations and publications

Presentations

- MAM-14 International symposium on Macro-And-Supramolecular Architectures and Materials November 2014, Mintek: Oral presentation: 'The effect of temperature and concentration on the synthesis of cobalt sulphide nanoparticles using single source precursors'.
- The 17th SACI Inorganic Conference June 2015, Rhodes: Poster presentation: 'Fabrication and characterization of poly(methyl methacrylate) nanofibers loaded with copper selenide nanoparticles'.
- 42nd National Convention of the South African Chemical Institute Conference December 2015, UKZ: Oral presentation: 'Fabrication and characterization of poly(methyl methacrylate) nanofibers loaded with copper selenide nanoparticles'.
- 1st VUT interdisciplinary research and postgraduate conference November 2016: Oral presentation: Fabrication and characterization of poly(methyl methacrylate) nanofibers with copper selenide nanoparticles.
- Environment, materials and green technology conference November 2016: Poster presentation: fabrication and characterization of poly(methyl methacrylate) nanofibers with copper selenide nanoparticles.

Publications

- S. B. Sibokoza, M. J. Moloto, N. Moloto, P.N. Sibiya, The effect of temperature and precursor concentration on the synthesis of cobalt sulfide nanoparticles using single-source precursor, Chalcogenide Letters, 2017, Vol. 14, No. 2, February 2017, p. 69 - 78
- Sibokoza SB, Moloto MJ, Mthunzi F, Moloto N; Diphenyldiselenide mediated synthesis of copper selenide nanoparticles and their poly(methyl methacrylate) nanofibers, Asian Journal of Chemistry, 2018, 30(7), 1455 – 1459.
- S. B. Sibokoza, M. J. Moloto, N. Moloto; Thermal decomposition of copper acetate at various temperature and time to form copper oxide/ copper nanoparticles, **to be submitted.**

Table of contents

Declaration statement ..... **ii**

Acknowledgements ..... **iii**

List of abbreviation ..... **iv**

Symbols and constant iv

Instrumentation v

Chemical reagents ..... **v**

Abstract ..... **vii**

Presentations and publications ..... **ix**

Presentations ix

Publications ix

List of tables ..... **xv**

List of equations ..... **xvi**

Chapter One **1**

Introduction **1**

Motivation **2**

Aim and Objectives **3**

Chapter Two **4**

2 General background **4**

2.1 Complexes **4**

2.2 Nanomaterials **10**

2.2.1 Surface Effects 11

2.2.2 Quantum Confinement 12

2.3 Nanocomposites **14**

2.3.1 Nanofibers fabrication methods 15

2.3.2 Electrospinning 16

2.3.3 Factors affecting electrospinning 17

2.4 Applications of nanocomposites **25**

2.4.1 Drug delivery 25

2.4.2 Tissue Engineering 25

2.4.3 Antibacterial materials 26

2.4.4 Filters and membranes 26

2.4.5 Sensors 27

2.4.6 Catalysis 27
2.5 Metal oxide, metal selenide, and poly(methyl methacrylate) 27
Chapter Three 30
3 Experimental 30
3.1 Materials 30
3.2 Experimental Procedure 30
3.2.1 Synthesis of copper complexes using diphenyldiselenide ligand 30
3.2.2 Synthesis of iron complexes using diphenyldiselenide ligand 30
3.2.3 Synthesis of silver complexes using diphenyldiselenide ligand 31
3.2.4 Synthesis of iron complexes using urea ligand 31
3.2.5 Synthesis of silver complexes using urea ligand 31
3.2.6 Synthesis of metal selenide nanoparticles 31
3.2.7 Synthesis of copper oxide nanoparticles 32
3.2.8 Synthesis of metal oxide nanoparticles 32
3.2.9 Preparation nanofibers 32
3.2.10 Antibacterial Activity for nanoparticles 32
3.2.11 Antifungal activity for nanoparticles 33
3.3 Characterization 34
3.3.1 Thermogravimetry 34
3.3.2 FT-IR spectroscopy 34
3.3.3 Microanalysis 34
3.3.4 Optical characterization 34
3.3.5 X-ray diffraction analysis 35
3.3.6 Scanning electron microscopy 35
3.3.7 Transmission electron microscopy 35
Chapter four 36
4 Results and discussions 36
4.1 Coordination Complexes 36
4.1.1 Complexes of urea 36
4.1.2 Diphenyldiselenide complexes 42
4.2 synthesis of metal oxide and metal selenide nanoparticles 47
4.2.1 Synthesis of silver oxide nanoparticles 47
4.2.2 Synthesis of silver selenide nanoparticles 50

4.2.3 Synthesis of copper oxide nanoparticles 53
4.2.4 Synthesis of copper selenide nanoparticles 56
4.2.5 Synthesis of iron oxide nanoparticles 58
4.2.6 Synthesis of iron selenide nanoparticles 60
4.3 Fabrication polymethyl methacrylate nanofibers incorporated with metal oxide or metal selenide nanoparticles 63
4.3.1 Synthesis of PMMA-AgO 64
4.3.2 Synthesis of PMMA-AgSe 67
4.3.3 Synthesis of PMMA-CuO 69
4.3.4 Synthesis of PMMA-CuSe 72
4.3.5 Synthesis of PMMA-FeO 74
4.3.6 Synthesis of PMMA-FeSe polymer fibres 77
4.4 Applications of the Nanoparticles: Antibacterial and Antifungal Activities 79
Chapter five 81
5 Conclusions and Recommendations 81
5.1 Conclusion 81
5.2 Recommendations 82
Chapter six 83
6 References 83

List of figures

Figure 2-1: Selenium based ligand which includes: (I) dimethyselenide, (II) dimethyl diselenide, (III) diethyldiselenide, (IV) diphenyl diselenide, (V) 2,2′-dithiennyl diselenide, (V) N-(2-(phenylseleno) ethyl)phthalimide, and (VI) 1,1′-methylene-bis(diphenylphosphine). 5
Figure 2-2: Reaction for the preparation of complex from diphenyl diselenide and metal salts. 6
Figure 2-3: Molecular model structure of urea. 7
Figure 2-4: Structure of urea with its resonance forms. 8
Figure 2-5: Resonance structure of metal-oxygen coordination of urea. 9
Figure 2-6: The bidentate coordination mode of urea towards metal ions. 10
Figure 2-7: Schematic drawing showing how surface-to-volume increased as the size is decreased 12

Figure 2-8: Illustration of energy diagram. 13
Figure 2-9: Absorption and emission. 14
Figure 2-10: Electrospinning setup. 16
Figure 4-1: The FTIR spectra of silver nitrate (a), urea (b), and silver urea complexes (c). 37
Figure 4-2: The graph for silver urea complex TGA (black) and derivative (red). 38
Figure 4-3: The FTIR spectra of copper acetate monohydrate. 39
Figure 4-4: The TGA (black) and derivative (red) spectra of copper acetate monohydrate. 40
Figure 4-5: The FTIR spectra of urea (a) and iron urea complex (b). 40
Figure 4-6: The graph of iron urea complex TGA (a), and derivative (b). 41
Figure 4-7: The FTIR spectra of diphenyldiselenide (a), and silver diphenyldiselenide complex (b). 42
Figure 4-8: The graph (TGA (a), and derivative (b)) of the silver diphenyldiselenide complex. 43
Figure 4-9: The FTIR spectra of diphenyldiselenide (a), and copper diphenyldiselenide complex (b). 44
Figure 4-10: The graph for bis(phenylselenolate) iron(II) complex TGA (a), and derivative (b). 45
Figure 4-11: The FTIR spectra of diphenyldiselenide (a), and bis(phenylselenolate) iron(II) complex (b). 46
Figure 4-12: The graph (TGA (a) and derivative (b)) of bis(phenylselenolate) iron(II) complex. 47
Figure 4-13: The UV-Vis (solid lines)) and PL (doted lines) spectra of silver oxide nanoparticles prepared for 1 hour at 150 °C, and 0.125 g of $Ag_2(U)(NCO)(NO_3)(CH_3OH)$ complex. 48
Figure 4-14: The XRD graph of silver oxide nanoparticles prepared for 1 hour at 150 °C, and 0.125 g of a $Ag_2(U)(NCO)(NO_3)(CH_3OH)$ complex. 49
Figure 4-15: The TEM image of silver oxide nanoparticles prepared for 1 hour at 150 °C, and 0.125 g of a $Ag_2(U)(NCO)(NO_3)(CH_3OH)$ complex. 50
Figure 4-16: The absorption (black) and photoluminescence (red) spectra of silver selenide nanoparticles prepared at 150 °C, for 1 hour, and 0.125 g of $Ag_2(NO_3)(C_6H_5Se)_2$ complex. 51
Figure 4-17: The XRD graph of silver selenide nanoparticles prepared at 150 °C, for 1 hour, and 0.125 g of $Ag_2(NO_3)(C_6H_5Se)_2$ complex. 52

Figure 4-18: The TEM image of silver selenide nanoparticles prepared at 150 °C, for 1 hour, and 0.125 g of $Ag_2(NO_3)(C_6H_5Se)_2$ complex. 53
Figure 4-19: The absorption (black) and photoluminescence (red) spectra of $CuAc_2{\cdot}H_2O$ calcined for 60 minutes at 400 °C. 54
Figure 4-20: The XRD graph of $CuAc_2{\cdot}H_2O$ calcined for 60 minutes at 400 °C. 55
Figure 4-21: The TEM image of $CuAc_2{\cdot}H_2O$ calcined for 60 minutes at 400 °C. 55
Figure 4-22: The absorption (black), and Photoluminescence (red) spectra of copper selenide nanoparticles prepared by using 0.125 g of the $Cu(Cl)_2(C_6H_5Se)_2$ complex, 5 g HDA at 145 °C for 60 minutes. 56
Figure 4-23: The XRD graph of copper selenide nanoparticles prepared by using 0.125 g of the $Cu(Cl)_2(C_6H_5Se)_2$ complex, 5 g HDA at 145 °C for 60 minutes. 57
Figure 4-24: TEM image of copper selenide nanoparticles prepared by using 0.125 g of the $Cu(Cl)_2(C_6H_5Se)_2$ complex, 5 g HDA at 145 °C for 60 minutes. 58
Figure 4-25: The absorption spectra of iron oxide nanoparticles prepared using 0.125 g of $FeCl_2{\cdot}3U{\cdot}4H_2O$ complex at 150 °C, for an hour. 59
Figure 4-26: The XRD patterns of iron oxide nanoparticles prepared using 0.125 g of $FeCl_2{\cdot}3U{\cdot}4H_2O$ complex at 150 °C, for an hour. 59
Figure 4-27: The TEM image of iron oxide nanoparticles prepared using 0.125 g of $FeCl_2{\cdot}3U{\cdot}4H_2O$ complex, at 150 °C, for an hour. 60
Figure 4-28: The absorption spectra of iron selenide nanoparticles prepared using 1.0 g of bis(phenylselenolate) iron(II) complex, at 150 °C for an hour. 61
Figure 4-29: The XRD graph of iron selenide nanoparticles prepared using 1.0 g of bis(phenylselenolate) iron(II) complex, at 150 °C for an hour. 62
Figure 4-30: The TEM image of iron selenide nanoparticles prepared using 1.0 g bis(phenylselenolate) iron(II) complex, at 150 °C for an hour. 63
Figure 4-31: The FTIR for PMMA-AgO nanofiber prepared by varying weight of AgO nanoparticles: 0 % (a), 0.1% (b), 2 % (c). 65
Figure 4-32: The TGA graph of PMMA-AgO nanofibers prepared by varying weight of AgO: 1% (a), and 2% (b). 66
Figure 4-33: The SEM image of PMMA-AgO nanofibers prepared by varying the weight of AgO: 0% (a), 0.1% (b), 2 % (c). 67
Figure 4-34: The FTIR spectra for PMMA-AgSe prepared by varying the weight of AgSe: 0% (a), 0.1% (b), 2 % (c). 68

Figure 4-35: The TGA graph of PMMA-AgSe prepared by PMMA loaded with 0.1 % AgSe (a), and 2 % AgSe. 68
Figure 4-36: The SEM image of PMMA-AgSe prepared by PMMA loaded with varying weight of AgSe: 0% (a), 0.1% (b), 2 % (c). 69
Figure 4-37: The FTIR spectra of PMMA (a), PMMA-0.1% CuO (b), and PMMA-2% CuO (c). 70
Figure 4-38: The TGA graph of PMMA-CuO prepared by PMMA incorporated with 0.1% CuO (a), and 2% CuO (b). 71
Figure 4-39: The SEM image of PMMA (a), PMMA-CuO (b), and PMMA-0.2% CuO (c). 71
Figure 4-40: The FTIR spectra of PMMA (a), PMMA-0.1% CuSe (b), and PMMA-2% CuSe (c). 72
Figure 4-41: The TGA graph of PMMA-0.1% CuSe (a), and PMMA-2% CuSe (a). 73
Figure 4-42: The SEM image of PMMA (a), PMMA-CuSe (b), and PMMA-0.2% CuSe (c). 74
Figure 4-43: The FTIR spectra of PMMA (a), PMMA-0.1% FeO (b), PMMA-2% FeO (c). 75
Figure 4-44: The TGA graph of PMMA-0.1% FeO (a), and PMMA-2% FeO (b). 76
Figure 4-45: The SEM image of PMMA (a), PMMA-FeO (b), and PMMA-0.2% FeO (c). 76
Figure 4-46: The FTIR spectra of PMMA (a), PMMA-0.1% FeSe (b), PMMA-2% FeSe (c). 77
Figure 4-47: The TGA graph of PMMA-FeSe prepared by PMMA incorporated with 0.1%FeSe (a), and 2% FeSe (b). 78
Figure 4-48: The SEM image of PMMA (a), PMMA-FeSe (b), and PMMA-0.2% FeSe (c). 78

List of tables

Table 4-1 Characteristic infrared frequency and assignment of urea, silver and iron complexes. 37
Table 4-2: Summary of wavenumber (cm^{-1}) and functional group of PMMA/Metal Oxide (Selenide) nanofibers. 64

Table 4-3: MIC (mg/mL) of metal oxide and metal selenide nanoparticles against various microorganisms..... 80

List of equations

Equation 2-1: Structural resonance of urea..... 6
Equation 2-2: Reaction for industrial preparation of urea 7

Chapter One

Introduction

Nanotechnology is the design, characterization, production and application of structures, devices, and systems by controlling shape and size at the nanometer scale. It deals with the creation of functional materials, devices, and systems through control of matter on the nanometer scale (1–100 nm). It is the self-assembly of individual atoms, molecules, or molecular clusters into structures to create materials and devices with new or enhanced properties. By harnessing these new properties, researchers can develop materials, devices, and systems that are superior to those in use today.

The developments of these materials could result in technological advantages. The nanoparticle is a small amount of the particles (size of 1-100 nm), which have a finite number of atoms (~100 to ~10,000 atoms).[1] Nanomaterials have been exploited because of their new or enhance properties than those of their bulk counterparts.[2] They are obtainable as a dispersion of a solid in a liquid (colloidal sol). Metal sols possess fascinating colors and have long been used as dyes. In 1857, Faraday established that dyes consist of tiny metal chunks.[3] Semiconductor nanocrystals were discovered a century later.[4] Nanoparticles possess high surface area, a large fraction of the atoms in a nanocrystal are on its surface. The sizes of the nanomaterials have drastic effects on the surface properties. The decrease in nanomaterials size results to more atoms being at the surface.[5] A small nanoparticle of 1 nm diameter will have as much as 30% of its atoms on the surface, while a larger nanocrystal of 10 nm (~1000 atoms) will have around 15% of its atoms on the surface.[6] However, this causes their surface effects to become more significant due to an increase of surface atoms ratio in the volume fraction.[7] Furthermore, the small size of nanoparticles results in higher reactivity due to more atoms in the surface. This has a large contribution to the thermodynamic characteristics and could have a profound effect on the shape of nanoparticles.[8] The nanoparticles show new or enhance properties such as physical, biological, electronic, optical, electrical, magnetic, chemical and mechanical.[6] These new or enhanced properties of nanoparticles have resulted in a wide range of application in various fields.[9]

This research is an interdisciplinary work aimed at obtaining new nanocomposites synthesized from polymeric materials modified with nanoparticles of different composition. The developments of these materials could result in technological advantages such as water

purification. Most material used in water purification target removal of contaminants such as heavy metal and organic waste. The bacterial contaminants are often killed by adding chlorine after removal of heavy metal and organic contaminants. The chlorine byproducts are associated with cancer.[10] The higher chloride is not safe for human consumption. Some metal oxide nanoparticles such as copper oxide, silver oxide are known to be anti-bacterial.[11] Nanoparticles can be used for removal of heavy metal.[12] The new material which can remove organic and heavy metals and kill bacteria at the same time is needed. However, an enormous exposure to nanoparticles can lead to environmental hazards as these materials can be toxic to organisms. A massive industrial production of nanoparticles could lead to release into the environment and their toxicity on both humans and another organism has raised concerns to both public and science. This is found to be paradoxical when one considers the environmental risks of nanoparticles and understands their potential to produce more environmentally friendly process and their use to deal with environmental contaminants.[5] Hence, this study is an initiative to develop a method to fabricate materials which can be applied in wastewater treatment. Polymers have been used as membranes in water treatment.[13] The nanoparticles can be incorporated into the polymer matrix. This will play a major role in the stability of the material. Thus, the mobility of this material will be preventing by being attached to the polymer. Therefore, enhance easy recovery from the environment. Thus, the project is based on synthesis and characterization of iron oxide, iron selenide, copper selenide, copper oxide, silver selenide and silver oxide nanofibers from the poly(methyl methacrylate) by using single-source precursors. The nanoparticles will be exploited for their magnetic, antimicrobial and antibacterial activities. The polymer will play a significant role in the removal of inorganic waste in the water. The research involves the synthesis of diphenyl diselenide and urea complexes of iron, copper, zinc and silver. The compounds will be used to synthesize Fe_xO_y, Fe_xSe_y Cu_xSe_y, Cu_xO_y, AgSe and AgO nanoparticles. These nanoparticles will be mixed with copolymers and electrospun to get nanocomposites.

Motivation

Advanced engineering applications often require multifunctional materials with a wide range of tunable properties. Such a technological demand is usually difficult to fulfill using single-phase materials. Hence, there is an increasing need to combine materials with unique properties, in a synergetic manner, to achieve certain technological goals. This has prompted

the development of novel types of composite materials and the implementation of innovative processing routes. Present-day materials used for cleaning water have only one capability. They use the polymer as filters to remove inorganic-organic waste. These polymers are less activity in killing bacteria. Hence, the water will need further treatment in order kill bacteria. By using these nanocomposites, the properties of the polymers will be improved dramatically. These composite materials are designed to have two capabilities, antibacterial activities as well as removal of heavy metals from water.

Aim and Objectives

The aim of the study is to prepare nanofibers materials by using poly(methyl methacrylate) solutions incorporated with nanoparticles (Cu_xSe_y, Cu_xO_y, AgSe, AgO, Fe_xSe_y, and Fe_xO_y), and their use as bactericidal and water treatment material.

Objectives:

- To synthesize and characterize Cu, Fe, and Ag complexes from the selenium-based ligand.
- To synthesize and characterize Fe, Cu, and Ag complexes from oxygen-based ligands.
- To synthesize and characterize Fe_xSe_y, Cu_xSe_y and AgSe nanoparticles from Cu, Fe, and Ag complexes of selenium-based ligands.
- To synthesize and characterize Cu_xO_y, Fe_xO_y and AgO nanoparticles from Cu, Fe and Ag complexes of oxygen-based ligands.
- To study the ant-microbial effect of the prepared nanoparticles.
- To synthesize nanofiber from poly(methylmethacrylate) solutions incorporated with nanoparticles of Cu_xSe_y, Fe_xSe_y, AgSe, Cu_xO_y, Fe_xO_y, AgO.

Chapter Two

2 General background

2.1 Complexes

Selenium is an essential element in the biology of the vertebrate. Selenium atoms are known to accompany or substitute sulfur atom in most organisms, and coordination sites. Selenium-base (organo-selenium) ligands can exist as both aliphatic and aromatic compounds (Figure 2-1). Selenium can be used to prevent cancer, and cardiovascular diseases.[14] Some organo-selenium compounds are found in living tissues such as selenocoenzyme A, selenobiotine, Se-methyl selenocysteine, Se-methylselenomethionine, selenocystathione, selenohomocytine, selenocystine, selenomethionine,[15] and glutathionperoxidase.[14] Organo-selenium compounds are known for their antimicrobial, antifungal, antiviral, and antioxidant activities.[16] Selenoproteins, and organoselenium derivatives are utilized in the redox process of living systems.[17] Organoselenium compounds are also used to catalyze the formation of superoxide radicals which prevent the microorganism attachment to the solid surface.[18] Selenocynate and diselenide are regarded as an antileishmanial compounds.[19] Dibeptyldiseleide has attracted a lot of interest in biochemists and pharmacology because of their antitumor activity.[20] Diselenides are known as mediators, redox catalysts, and essential precursors in organic electrosynthesis.[14]

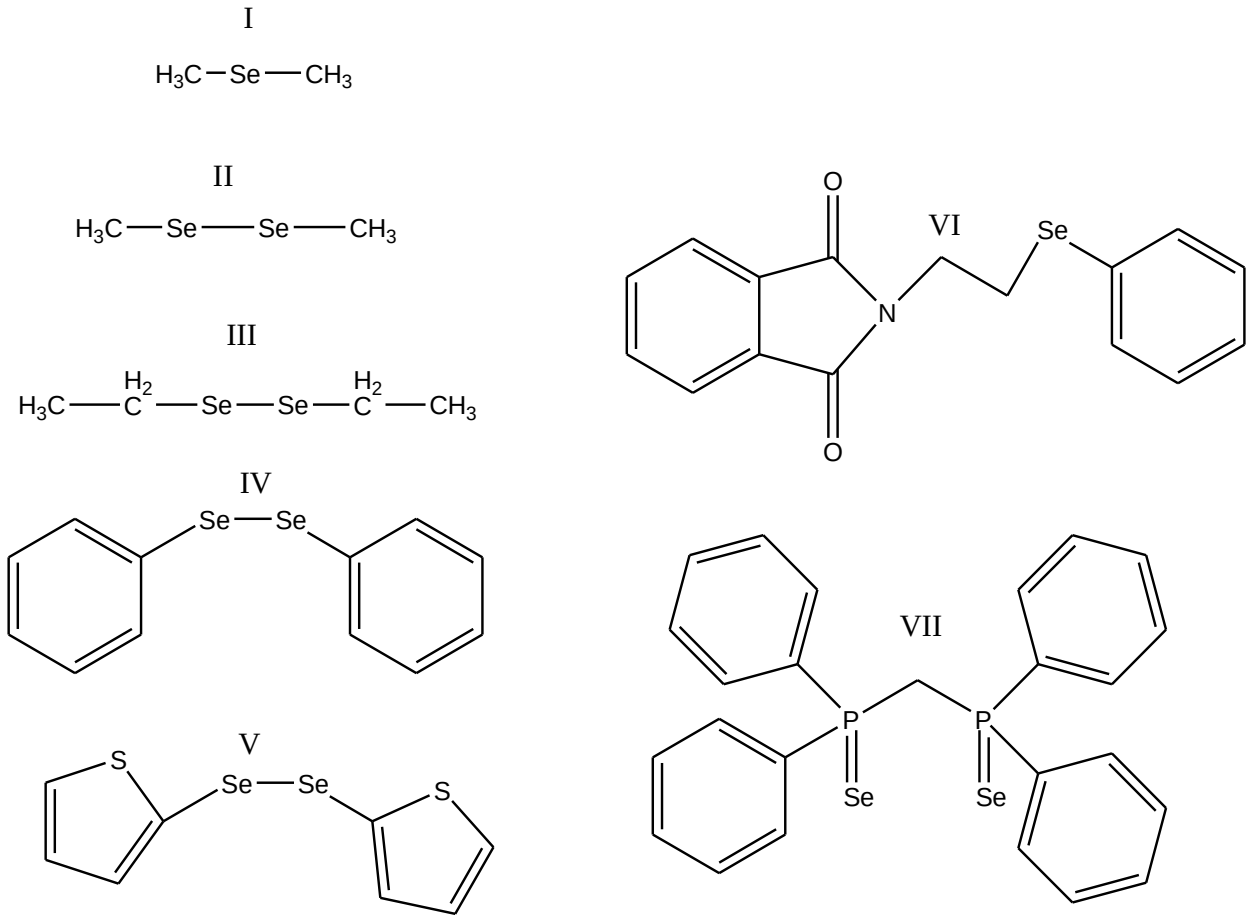


Figure 2-1: Selenium based ligand which includes: (I) dimethyselenide, (II) dimethyl diselenide, (III) diethyldiselenide, (IV) diphenyl diselenide, (V) 2,2′-dithiennyl diselenide, (V) N-(2-(phenylseleno) ethyl)phthalimide, and (VI) 1,1′-methylene-bis(diphenylphosphine).

Metal selenide based compounds are known for their importance in biological systems.[21] These compounds are characterized by metal atom bonded to selenium donor ligands such as metalloproteins. The complexes of metal-selenide are often utilized as precursors for metal selenides.[22] Diphenyl diselenide has been widely used in the preparation of organoselenium complexes with some metals. Diselenide ligands can coordinate to the metal atom as mono-dentate and bidentate. Diselenide ligands (diphenyl diselenide, dimethyl diselenide, diethyl diselenide) undergo reduction to form organoselenide anion. The organoselenide anion reacts with the metal salts to form complex (Figure 2-2).[23] However, diphenyl diselenide can use two selenium atoms to bridge between metal atoms.[24] Furthermore, diselenide derivative [$Ph_2P(Se)$-CH_2-$P(Se)Ph_2$] can form bidentate using two selenium atoms to coordinate to the metal.[25] Other organoselenide derivative may contain more than one type of donor atoms (Se, N) or (Se, N, O), which can be used to coordinate to the metal atoms.[23]

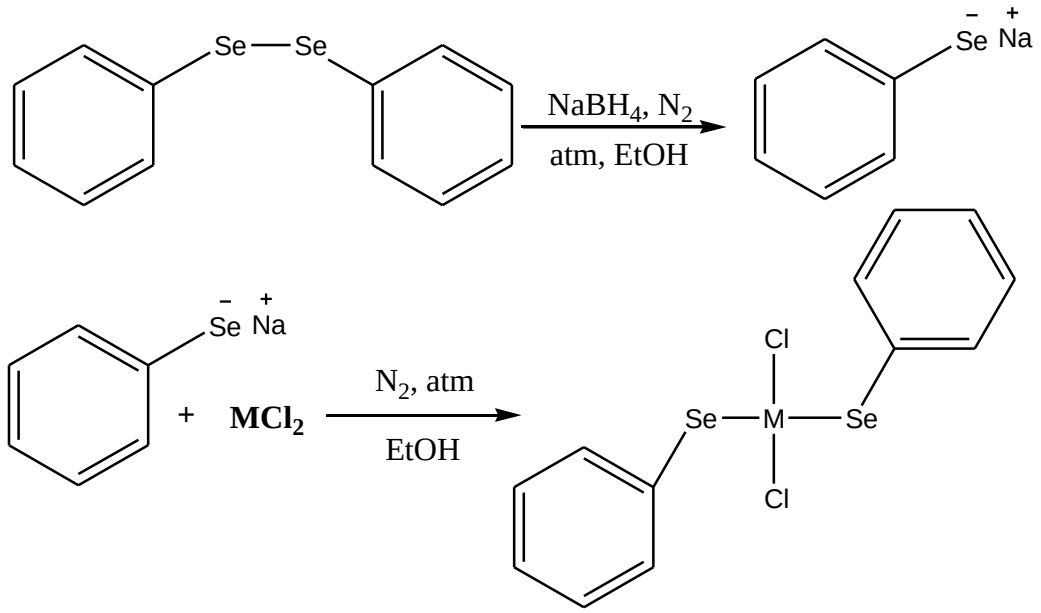
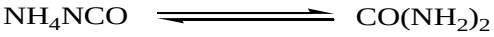


Figure 2-2: Reaction for the preparation of complex from diphenyl diselenide and metal salts.

Some researchers used electrochemical oxidation technique to prepare phenylselenolato complexes M(SePh)n.[21] The electrochemical oxidation of anodes of selected metals (Zn, Cd, Cu, Ag, TI, Sn) in non-aqueous solutions of diphenyl diselenide with platinum foil as the cathode gives the corresponding M(SePh), compounds in high yields.[21] The selected metals (Zn, Cd, Cu, Ag, TI, Sn) were used as an anode in the solution of diphenyl diselenide (non-aqueous) and platinum foil as the cathode.

Urea (Figure 2-3) is known by many chemical names which include: diaminomethanal (IUPAC), carbonyldiamine. Wohler and coworkers used potassium isocyanate and ammonium sulfate solution to prepare urea for the first time.[26] The formed ammonium isocyanate undergoes molecular rearrangement to give urea (Equation 2-1).



Equation 2-1: Structural resonance of urea.

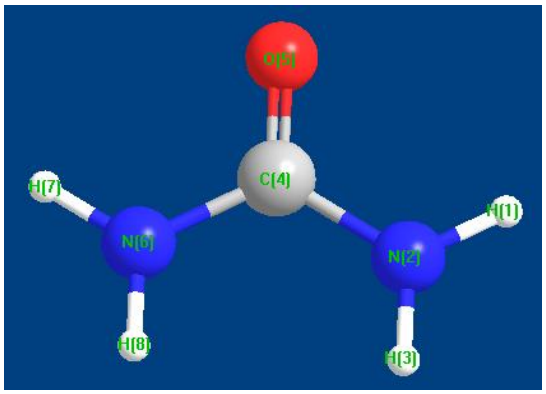


Figure 2-3: Molecular model structure of urea.

Urea has been prepared in the laboratory using ammonia and carbonyl chloride, alkyl carbonates, chloroformates or urethans. It can also be prepared industrially by liquid carbon dioxide and liquid ammonia (Equation 2-2), and the formed ammonium carbamate decomposed at 130-150 °C under 35 atmospheric pressure to urea and water.[27]

$$2NH_3 + CO_2 \longrightarrow NH_2COONH_4 \longrightarrow CO(NH_2)_2 + H_2O$$

Equation 2-2: Reaction for industrial preparation of urea.

Urea is excreted as the byproduct of protein metabolism. Human (adults) excretes about 30 g of urea as urine each day.[28] Urea is a water-soluble compound with a melting point of 132 °C.[28] It has been used in the preparation of formaldehyde-urea resin (plastic),[28] barbiturates,[28] fertilizers,[29] paper industry, and medical applications.[30] Urea is regarded as the weak base which can react with acids to form salts.[31] It is characterized by three resonance structures (: Structure of urea with its resonance forms.

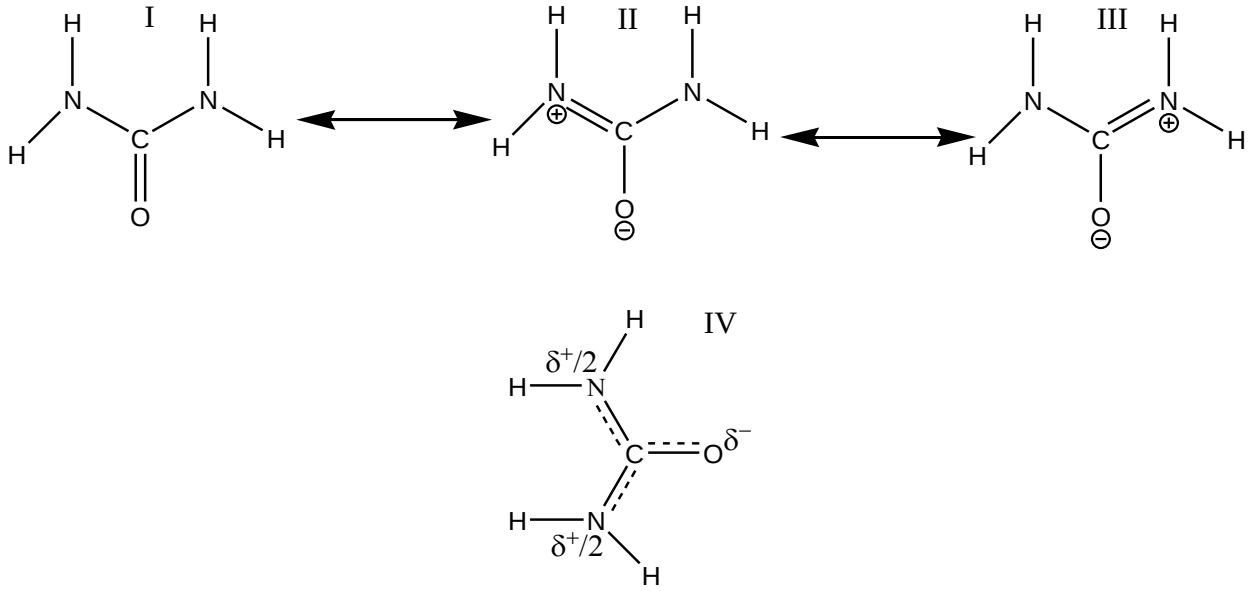


Figure 2-4: Structure of urea with its resonance forms.[31]

The two-equivalent form with charges (Figure 2-4 :(II) and (III)), leads to greater stability of urea. The crystal structure of urea shows an interatomic distance of 1.26 ± 0.01 A (C-O), and 1.34 ± 0.01 A (N-C).[32] These interatomic distances are associated with double bond character 20-30% for the carbon-nitrogen, and 50-60% for the carbon-oxygen bond.[33]

The three structures can be represented by an average structure (Figure 2-5 : (IV) (hybrid)).[31] The hybrid resonance structure has been reported in literature.[34] This hybrid structure shows that the CO bond is less than double bond.[31] Furthermore, the charged resonance structures (Figure 2-5: (II) and (III)) are induced by the hydrogen bonding between carbonyl oxygen atoms and the hydrogen atoms, C=O···HN.[35] These effects lead to an increase in the C-N force constant, while C-O force constant is decreased.[36] The same effect was observed in the stretching frequency of urea and uranium cation.[31] The CO stretching frequency is at 1689 cm^{-1} for urea, and at 1310 cm^{-1} for the uranium cation. This show that $C\text{-}O^{-}$ change to the single bond character. Furthermore, the C-N stretching frequency is shifted from 1446 cm^{-1} for urea, and to 1553 cm^{-1} for uranium cation. This due to C-N bond changing to be a double bond character. In general, when urea changes to uranium cation the NH and CN bonds increase in frequency, while CO bond decreases in frequency.[31]

Complexes of urea with some metal ions are used as fertilizers,[28] pharmaceutical application,[37] antibacterial and antifungal agents.[38] Urea can be characterized by three coordination sites with the metal which include carbonyl oxygen, and two nitrogen atoms. In most cases, urea can coordinate with oxygen atom with many metal atoms to form monodentate oxygen-metal

(C=O···M) with an angle less than 180°, by sp^2 hybridization of the O atom.[38] The formation of unidentate oxygen-metal bods between urea molecules and metal ions show minor changes on the infrared spectra of urea. The infrared spectra change observed less effect on the N-H stretching frequency, a lowering of the C=O stretching frequency. The metal-urea complexes (O-M) show resonance that contributes to their stability. The stability is associated with resonance structures, as demonstrated one urea ligand bound to the metal through O-M. The complexes are less affected by the oxidation of the metal ions.[31] Moreover, urea and its substituted can form extended hydrogen-bonded frameworks and have been used in the frame of organic crystal engineering. Symmetrically substituted urea (RHNCONHR) can form α-networks using two hydrogen atoms to form a hydrogen bond with the carbonyl oxygen of the nearby molecule in a network.[39] Urea complexes have hydrogen bonding interaction due to intermolecular or interionic, which results in frameworks. This hydrogen bonding leads to greater stability of the complexes.[39]

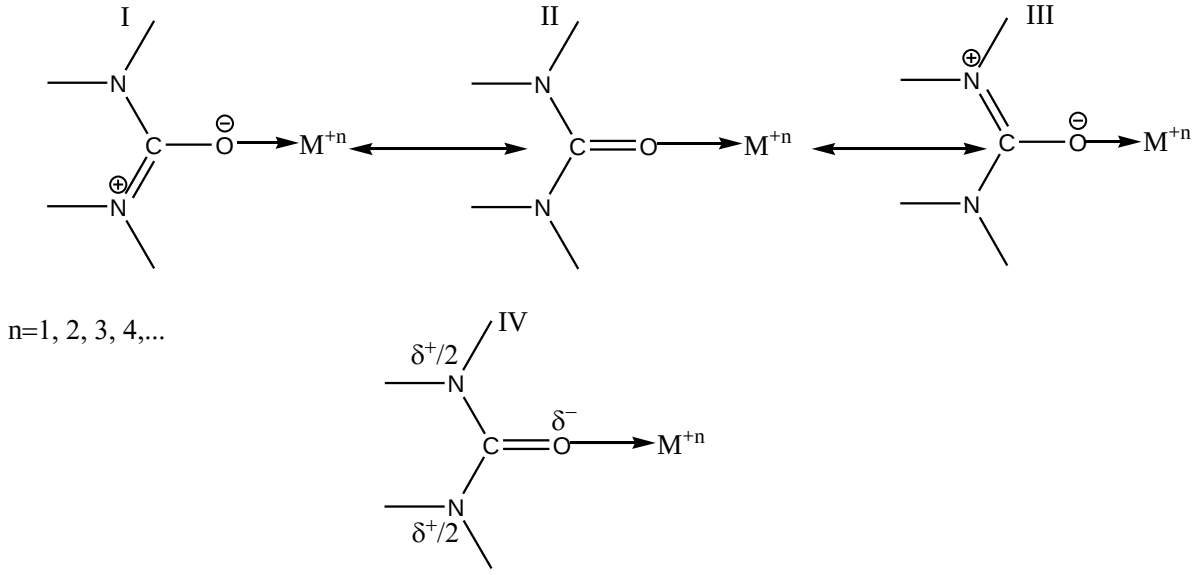


Figure 2-5: Resonance structure of metal-oxygen coordination of urea.[39]

However, urea can bond to the metal through nitrogen as both a bidentate (N-M, O-M), and unidentate (N-M). The formation of an M-N bond leads to more electrons needed of the nitrogen, and hinder the resonance.[31] Hence, an increase in the C=O stretching frequency, and lowering of CN stretching frequency. Urea can coordination with both oxygen and nitrogen atoms (Figure 2-6: I).[40] Urea can also use oxygen atom to bridges two Hg^{II} ions in $[Hg_2(CON_2H_4)_2]$ (Figure 2-6 :(II). Furthermore, urea attracts more interest in chemical/ biology

activities because of its ability to undergo metal-promoted deprotonation.[27] Urea as anionic ligand H_2NCONH^- can coordinate with both nitrogen and oxygen to bridge two metal ions (μ_2 mode), and with two nitrogen and oxygen to bridge three metal ions (μ_3) in Figure 2-6: (III), and (IV) respectively.

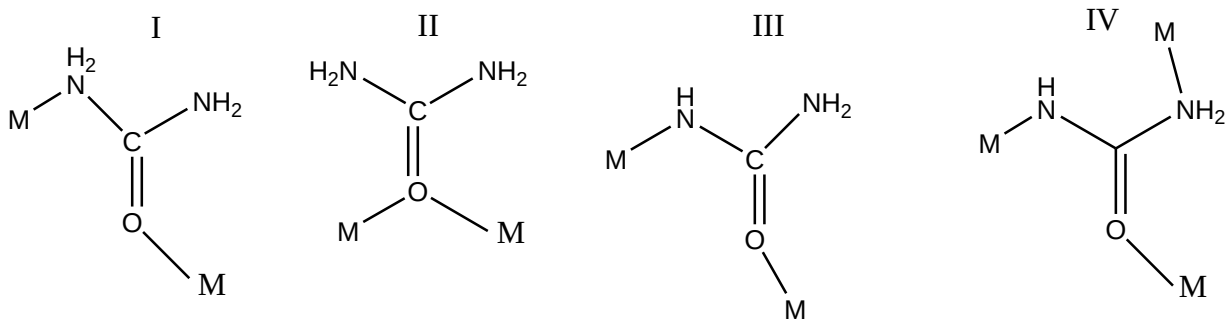


Figure 2-6: The bidentate coordination mode of urea towards metal ions.[27]

The first-row transitional metal-urea complexes have been intensively studied. In most of the first-row metal, atoms are bound to urea ligand through an oxygen (metal-oxygen bond).[31] The M-O interatomic bond distance was increased with metal atom size.[27] Cadmium and antimony are the only second and third-row transition-metals crystal structure reported.[27] However, in metal-urea complexes, IR spectra can be used to confirm if the interaction of the metal atom is through the oxygen atom or nitrogen atom. An increase of the *ν*C=O stretching vibration and a decrease of the NH_2 stretching vibrations can be associated with nitrogen-metal bonding in the complex. A decrease of the *ν*C=O stretching vibration and an increase of the NH_2 stretching vibrations can be related to oxygen-metal bonding in the complex. In general; hard Lewis acids, alkali and alkaline-earths can bond urea through the oxygen atom (metal-oxygen bond). On the contrary, soft Lewis acids can bind to urea using nitrogen atom (metal-nitrogen bond). Some metal atoms (Co and Pt) can use both oxygen, and nitrogen atom bond (M-O, and M-N).

2.2 Nanomaterials

Nanomaterials are the materials with one of its dimensions in the range of nanometer scale (1-100 nm). Nanomaterials can be classified as metals based materials, carbon-based, and polymer materials. Nanomaterials can be nano-sized along one (films), two (rods), and three (dot) dimensions. Nanomaterials exhibit superior properties which are specific to their nanoscale size.[41] The nanomaterials have revealed advanced physical, electrical, magnetic and biological properties compared to their bulk counterparts.[42] These properties can be attributed to surface

effects and quantum confinement.[43] These are two size dependent factors yield nanomaterials with the higher surface area, high surface energy, spatial confinement and reduced imperfection, which do not exist in larger dimension materials.

2.2.1 Surface Effects

Nanoparticles have increased surface area compared to their bulk counterparts. If a bulk sphere is subdivided into an ensemble of individual nanoparticles, the total volume of the sphere remains the same, and the collective surface area is greatly increased.[9] Figure 2-7 show a schematic drawing to illustrate surface-to-volume increase as the size is decreased. With the decrease in particle size, a large proportion of atoms is found on particle's surface compared to those within the inside core. For example, a material with a size of 30 nm have 5% of atoms in their surface, 10 nm have 20 % of atoms in their surface, and 3 nm have 50% of atoms in their surface.[6] As a consequence, nanoparticles have high surface-to-volume ratio compared to that of bulk parent material. Thus nanomaterials surfaces and surface properties (physical and chemical interactions) will have more influence on interfacial characteristics and agglomerations.[44] Hence, this will have more effect on reactions that occur at the surface such as catalysis, detection and physical adsorption of certain species at the material's surface. The optical and chemical properties of nanoparticles are associated with the large surface area to volume ratio of nanoparticles.[45] The relative surface area per unit volume is inversely proportional to the diameter. Therefore, a large fraction of surface atoms, the inter-particle forces such as a Vander Waal force, electrostatic force, and magnetic attraction become stronger resulting in higher surface energy in nanomaterials.

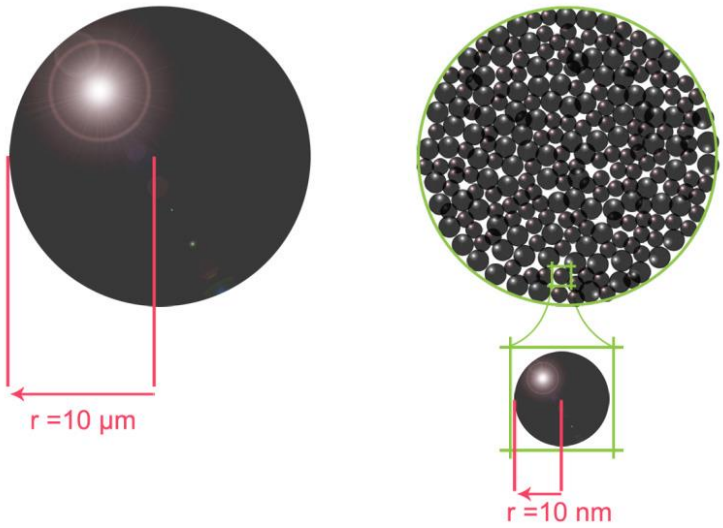


Figure 2-7: Schematic drawing showing how surface-to-volume increased as the size is decreased [9].

2.2.2 **Quantum Confinement**

In general, materials can be classified into conductors, semiconductors, and insulators. The classification of the materials is based on the energy separation of their energy bands. These energy bands are called valence bands (VB) and conduction bands (CB). The energy bands are formed from atomic orbital mixing between atoms in the crystal lattice. The valance bands are formed by the overlap of bonding orbital, whereas the conduction bands are formed by the overlap of antibonding orbitals. The valance bands are composed of the highest occupied molecular orbitals (HOMO). The conduction bands in composed of lowest unoccupied molecular orbital (LUMO). The band gap is the energy separation between the VB and CB. In conducting materials (metals), the VB and CB overlap and band gap energy (E_g) is small. The thermal energy is enough to stimulate electron to move to the conduction band. Insulators have a large bandgap that requires large amount of energy to overcome the threshold. Hence, in insulators, there is no electron excitation to the CB and very low electrical conductivity. Semiconductors are characterized by an important and small band gap. If an applied energy exceeds the bandgap energy, electron jump from VB to the CB, thereby forming electron-hole pairs called exciton.

In nanomaterial, quantum confinement occurs when the particles size of a nanocrystal is smaller than the exciton Bohr radius of the bulk semiconductor of the same compound. The spatial confinement effect is more pronounced in nanomaterials due to their size, which leads

to stronger quantum effect. The nano-sized semiconductor has quantized energy states. Therefore, CB and VB bands split up and become discretized Figure 2-8. Hence, the motion of electrons is highly confined, and their energy is quantized. The charge transfer occurs between discrete levels, and the only wavelength of a certain dimension is absorbed and monochromatic emission. The chemical and physical properties of nanomaterial are determined by the type of motion allowed for its electron. The allowed types of motion in atomic or molecular orbitals have well-defined energies that are well separated from one another. Thus, as consequence of the quantum confinement, the bandgap energy becomes large and more energy will be needed to be absorbed and emitted by the nanomaterial.[46] The energy of the band gap absorption (nanoparticle color) and emission become sensitive to the size and shape of nanoparticles.[47] Hence, the optical, physical and chemical properties of semiconductors nanomaterials are dependent on the size and shape of the particles Figure 2-9.

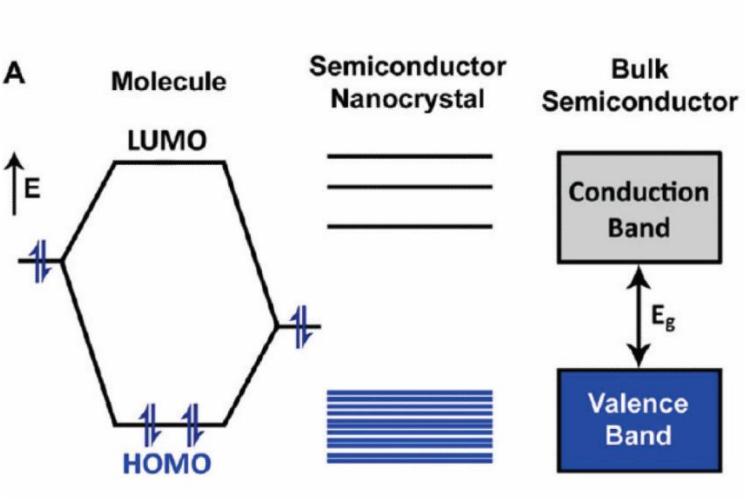


Figure 2-8: Illustration of energy diagram.[2]

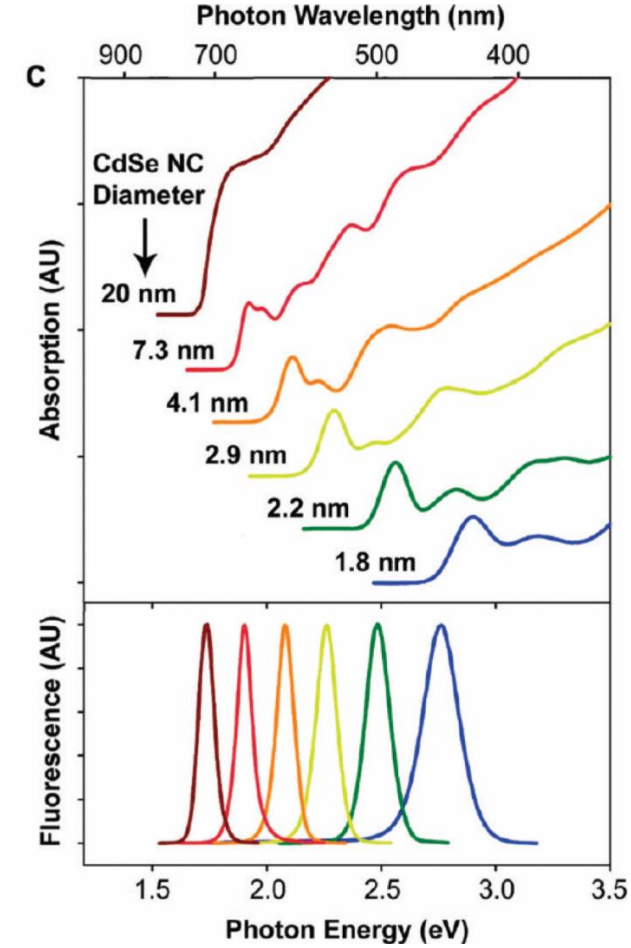


Figure 2-9: Absorption and emission.[2]

2.3 Nanocomposites

Composites are a multiphase material with a sizable proportion of each phase. Composites are formed by incorporating multiple phase components to get new material with unique properties. The materials are combined with the object of obtaining desired properties. In most case, the constituents are chemically dissimilar and separated by district interface. The properties of composites are characterized by the constituent phase, their relative amounts, and the geometry of the dispersed phase.[48] The phase can be composed of the following matrix: metal,[49] ceramic,[50] and polymer.[51] Metal matrix increases the yield stress, tensile strength, creep resistance. Ceramic matrix plays role fracture toughness. The polymer matrix is associated with an increased modulus, yield stress, tensile strength, and creep resistance. The dispersion could be classified as particles, fibers and structural.

The nanocomposite is classified as the materials in which one or more phase with nanoscale dimension (0-D, 1-D, and 2-D).[52] The nanocomposites are embedded with a metal, ceramic or polymer matrix. The primary goal behind the addition of the nanoscale second phase is to create a synergy between the various constituents, such that novel properties capable of meeting or exceeding design expectations can be achieved.[53] The properties of nanocomposite are affected by a range of variables such as matrix material, loading, the degree of dispersion, size, shape, and orientation of the nanoscale second phase with the matrix of the polymer.

Polymer-matrix nanocomposite has a matrix made from polymeric material. The second phase is composed of nanoscale dimension material (usually a few percent by weight) and dispersed in polymer matrix. The smaller size of the second phase leads to different properties.[54] The presence of nanoscale size material act as the reinforcing points to the higher significance of the interface-to-volume ratio compared to conventional composites. As a result, the volume fraction of the second phase can be reduced, without degradation of the desired properties. The nanoscale reinforcing phase can be classified into nanoparticles (0-D), nanotubes (1-D), Nanoplates (2-D).[9] The particles size and distribution play a significant role in nanoparticle reinforcement. The nanoparticles added into polymer nanocomposite can alter properties such as mechanical, electrical, optical, and thermal properties of the polymer material.[55]

The nanofibers can be significantly enhanced by reinforcing with nanoparticles. Fiber reinforcement using particles is a well-known method in textile and composite industries.[56] The fibers with reinforcement show new material with unique or enhanced properties.[57] Nanofibers are defined as the fibers with the diameter less than or equal to 1000 nm.[58] Nano-size fillers materials provide new opportunities for improving plastic composite materials different from conventional standard fillers.[59] Nanocomposites materials require only a minimal amount of nano-filler (less than 5 %) to yield marked improvement in mechanical, thermal, electrical, and other properties such as gas impermeability, dimensional stability, and flame retardance.[57] All of these benefits are available without sacrifices in composite density or light transmissions of matrix resign.[60] Nano-filler provides one to three orders of magnitude more interfacial area per particle than conventional mineral filler.[61]

2.3.1 **Nanofibers fabrication methods**

Nanofiber technology has been widely receiving a lot of attention, because of availability of techniques that can create nanoscale fibers from a broad range of polymers. Nanofiber shows unique properties such as low density, extremely high surface area to weight ratio, high pore volume, and controllable pore size. The various methods that have been employed to generate

nanoscale fibers include drawings, template synthesis, phase separation, self-assembly, and electrostatic spinning (electrospinning).

2.3.2 **Electrospinning**

Electrospinning has been extensively used because of its ability to fabricate nanostructures with a diameter in the range of nanometer to few micrometers.[62] Electrospinning is user friendly, versatile and can be used to prepare non-woven mats of ultrafine fiber.[63] This method has been used to make nanofibers using various types of raw material ranging from natural and synthetic polymers to make composites (consisting of organic and inorganic components).[64] The electrospinning setup has four significant parts as shown in Figure 2-10: power supply connected to anode and cathode, a capillary tube (glass syringe or pipette) containing a polymer solution, metallic needle (copper wire), and metallic collector (non-metallic collector covered with aluminum foil).

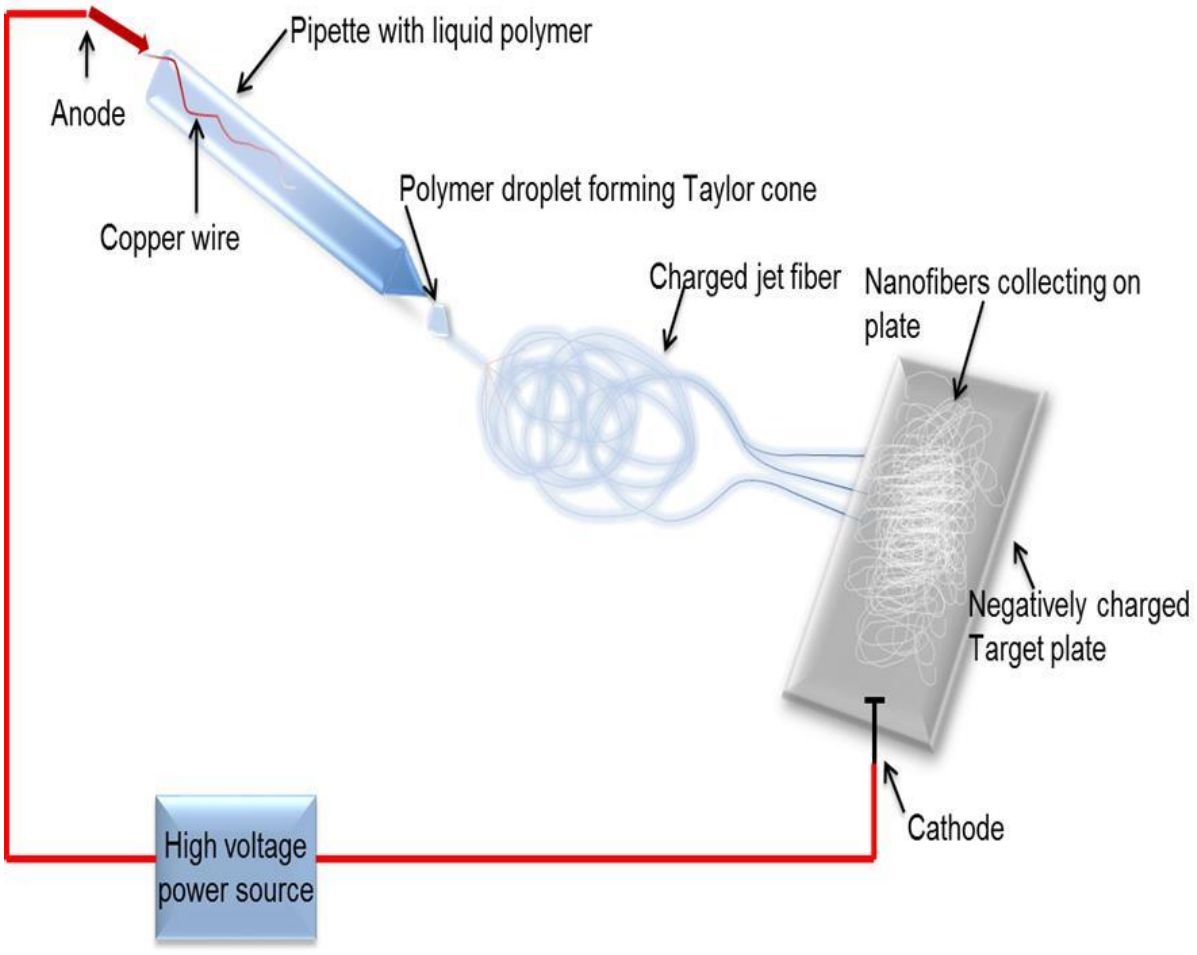


Figure 2-10: Electrospinning setup.

In the electrospinning method, a high electric field is applied to viscous polymer solution held in the capillary tube and induces a charge density on the liquid surface. Mutual charge repulsion

causes a force directly opposite to the surface tension. When the electric field is sufficiently high, the surface of the solution in the proximity of the tip of the capillary tube elongates and forms a Taylor cone. When a critical value of the electric field is reached, a repulsive electrical force overcomes the surface tension. The charged jet of the solution is ejected from the tip of the Tailor cone. As the jet accelerates and thins in the electric field, radial charges repulsion results in the splitting of the primary jet into multiple filaments that are called spraying. The solvents evaporate, and the filaments solidify in the collector. The filaments dry and form nanofibers.

2.3.3 Factors affecting electrospinning

Electrospinning is one of the preferred methods for producing continuous nanofiber from the range of materials. In electrospinning, the nanofiber is dependent on the preparation parameters which includes processing, ambient, and solution parametrs.

(a) Solution parameters

The molecular weight of a polymer is an important parameter that affects the electrospun nanofiber morphology. Molecular weight reflects the polymer chain entanglement, which has a direct effect on the solution viscosity, surface tension, and conductivity.[64] The polymers with very low molecular leads to the formation of beads.[65] An increase in the molecular weight of polymer solution results in smooth nanofibers.[66] However, polymers with high molecular weight lead to the formation of fibers with a larger diameter.[67]

Polymer concentration plays a significant role in the stretching of a jet in electrospinning. The stretching of the charged jet is affected by changing of concentration. At low concertation, the applied electric field and surface tension result into the breaking of an entangled polymer into fragments before reaching the collector.[68] These fragments lead to the formation of beads and beaded nanofibers.[69] An increase in the polymer concentration leads to an increase in the viscosity, which in turn increases the chain entanglement of the polymer solution. The entanglement will overcome the surface tension and result in uniform bead free nanofibers.[69] Furthermore, an increase of solution concentration beyond a critical value will result in a viscous solution which may prevent the flow of solution through the needle tip or beaded nanofibers.[68] Higher viscosity resists jet elongation and thinning and results in larger fiber diameter.[70] The concentration of the polymer has a significant effect on the morphology of the beads as well. The morphology of beads changes from a spherical droplet-like shape (with low viscosity) to a stretched droplets or ellipse to smooth fiber (with sufficient viscosity) as the solution viscosity changes.[71] Fong and coworkers explored the relationship of polyethylene

oxide (PEO) solution viscosity and bead formation. Their results indicated that solution viscosity is linked to the bead and density. A viscous solution resulted in less spherical and more spindle-like beads followed by nanofiber formation with occasional bead defects.[72]

The solvent of polymer solution plays a crucial role in electrospinning. The most important properties of the solvent are related to polymer solubility and its boiling point. The solvent should be able to dissolve the polymer completely. The solvent should have a moderate boiling point. The solvent with low boiling point are classified as volatile. The volatile solvent is not ideal options due to rapid evaporation and dehydration of the nanofibers.[73] The high evaporation rate of the low boiling solvent leads to rapid evaporation, which can cause the drying of the jet at the needle tip.[69] In contrast, high boiling points solvents may not dehydrate entirely before hitting the target resulting in flat ribbon shaped fibers instead of round fibers.[74] The volatility of solvent may affect the microscopic feature of electrospinning fiber including porosity, shape, and size hence, care must be taken during the evaluation and selection of electrospinning solvents.[74]

Solution viscosity is an important parameter in electrospinning for nanofiber morphology. The viscosity of the solution is dependent on the molecular weight and polymer concentration. The polymer viscosity can be easily adjusted by changing the polymer concentration. In general, low viscosity solution tends to have a higher surface tension which results in beads and beaded fibers.[75] However, polymers with a higher viscosity result in larger fiber or difficult in the ejection of the jet from the polymer solution of too high viscosity.[76] Fong et al. obtained different morphologies of PEO fiber at different viscosity.[72]

Solution conductivity is linked to Taylor cone formation and can be used to control the diameter of nanofibers. The solution with lower conductivity results to a droplet with no surface charge to form a Taylor cone, hence no electrospinning takes place.[69] However, an increase in conductivity to a critical value leads to the rise of the surface charge of the droplet. This result to the formation of the Taylor cone and smaller diameter nanofibers.[77] Hence, high conductivity yield greater tensile force, corresponding to applied voltage and reduction in the nanofiber diameter. The conductivity can be increased by addition of an electrolyte. Fong et al[72] reported that addition of sodium chloride in polymer solution leads to higher net charge density of electrospinning jet. The increased charge density results in the formation of smooth and uniform nanofiber.[72] Zong and co-workers also reported that addition of salts to the poly-DL-lactic acid (PDLLA) solution leads to smooth and bead-free fine diameter nanofibers.[78] Alternatively, the conductivity of polymer solution can be enhanced using surfactants.[79]

Modification using surfactants revealed comparable results with uniform and smaller diameter nanofiber.[80]

Surface tension is directly associated with the polymer and solvent. The surface tension can be varied by varying the solvents. The surface tension drives the formation of beads or beaded nanofibers.[72] The higher surface tension leads to the smaller surface area per unit mass, as result beads or beaded nanofibers are formed from spherical jet (droplets).[72] The formation of these droplets is a result of the capillary breakup of the spinning jet by surface tension.[72] However, low surface tension is associated with an excess charge which leads to increase in surface area. Hence, the thinner jet is formed which results in smoother nanofibers.[72] Yang and co-workers observed different surface tension on poly(vinyl pyrrolidone) PVP electrospun nanofiber morphology using ethanol, DMF, and MC as solvents. The reduction of surface tension results in the formation of smoother nanofibers while keeping other parameters fixed.[81] The reduction of surface tension contributes to the formation of nanofibers without beads.[82] Fong and co-workers study the effect of surface tension on poly(ethylene oxide) (PEO) by varying distil water and ethanol. They observed that by changing the solvent from pure water to a water-ethanol mixture, smooth fibers with larger diameter were produced. The increase of ethanol concentration has led to an increase in solution viscosity and the surface tension lower.[72] This has increased the filament diameter, which is associated with the decrease in net charge density and smaller charge repulsion force.[72]

The molecular weight of a polymer is an important parameter that affects the electrospun nanofiber morphology. Molecular weight reflects the polymer chain entanglement, which has a direct effect on the solution viscosity, surface tension, and conductivity.[64] The polymers with very low molecular leads to the formation of beads.[65] An increase in the molecular weight of polymer solution results in smooth nanofibers.[66] However, polymers with high molecular weight lead to the formation of fibers with a larger diameter.[67] Polymer concentration plays a significant role in the stretching of a jet in electrospinning. The stretching of the charged jet is affected by changing of concentration. At low concertation, the applied electric field and surface tension result into the breaking of an entangled polymer into fragments before reaching the collector.[68] These fragments lead to the formation of beads and beaded nanofibers.[69] An increase in the polymer concentration leads to an increase in the viscosity, which in turn increases the chain entanglement of the polymer solution. The entanglement will overcome the surface tension and result in uniform bead free nanofibers.[69] Furthermore, an increase of

solution concentration beyond a critical value will result in a viscous solution which may prevent the flow of solution through the needle tip or beaded nanofibers.[68] Higher viscosity resists jet elongation and thinning and results in larger fiber diameter.[70] The concentration of the polymer has a significant effect on the morphology of the beads as well. The morphology of beads changes from a spherical droplet-like shape (with low viscosity) to a stretched droplets or ellipse to smooth fiber (with sufficient viscosity) as the solution viscosity changes.[71] Fong and coworkers explored the relationship of polyethylene oxide (PEO) solution viscosity and bead formation. Their results indicated that solution viscosity is linked to the bead and density. A viscous solution resulted in less spherical and more spindle-like beads followed by nanofiber formation with occasional bead defects.[72]

The solvent of polymer solution plays a crucial role in electrospinning. The most important properties of the solvent are related to polymer solubility and its boiling point. The solvent should be able to dissolve the polymer completely. The solvent should have a moderate boiling point. The solvent with low boiling point are classified as volatile. The volatile solvent is not ideal options due to rapid evaporation and dehydration of the nanofibers.[73] The high evaporation rate of the low boiling solvent leads to rapid evaporation, which can cause the drying of the jet at the needle tip.[69] In contrast, high boiling points solvents may not dehydrate entirely before hitting the target resulting in flat ribbon shaped fibers instead of round fibers.[74] The volatility of solvent may affect the microscopic feature of electrospinning fiber including porosity, shape, and size hence, care must be taken during the evaluation and selection of electrospinning solvents.[74] Solution viscosity is an important parameter in electrospinning for nanofiber morphology. The viscosity of the solution is dependent on the molecular weight and polymer concentration. The polymer viscosity can be easily adjusted by changing the polymer concentration. In general, low viscosity solution tends to have a higher surface tension which results in beads and beaded fibers.[75] However, polymers with a higher viscosity result in larger fiber or difficult in the ejection of the jet from the polymer solution of too high viscosity.[76] Fong et al. obtained different morphologies of PEO fiber at different viscosity.[72]

Solution conductivity is linked to Taylor cone formation and can be used to control the diameter of nanofibers. The solution with lower conductivity results to a droplet with no surface charge to form a Taylor cone, hence no electrospinning takes place.[69] However, an increase in conductivity to a critical value leads to the rise of the surface charge of the droplet. This result

to the formation of the Taylor cone and smaller diameter nanofibers.[77] Hence, high conductivity yield greater tensile force, corresponding to applied voltage and reduction in the nanofiber diameter. The conductivity can be increased by addition of an electrolyte. Fong et al[72] reported that addition of sodium chloride in polymer solution leads to higher net charge density of electrospinning jet. The increased charge density results in the formation of smooth and uniform nanofiber.[72] Zong and co-workers also reported that addition of salts to the poly-DL-lactic acid (PDLLA) solution leads to smooth and bead-free fine diameter nanofibers.[78] Alternatively, the conductivity of polymer solution can be enhanced using surfactants.[79] Modification using surfactants revealed comparable results with uniform and smaller diameter nanofiber.[80] Surface tension is directly associated with the polymer and solvent. The surface tension can be varied by varying the solvents. The surface tension drives the formation of beads or beaded nanofibers.[72] The higher surface tension leads to the smaller surface area per unit mass, as result beads or beaded nanofibers are formed from spherical jet (droplets).[72] The formation of these droplets is a result of the capillary breakup of the spinning jet by surface tension.[72] However, low surface tension is associated with an excess charge which leads to increase in surface area. Hence, the thinner jet is formed which results in smoother nanofibers.[72] Yang and co-workers observed different surface tension on poly(vinyl pyrrolidone) PVP electrospun nanofiber morphology using ethanol, DMF, and MC as solvents. The reduction of surface tension results in the formation of smoother nanofibers while keeping other parameters fixed.[81] The reduction of surface tension contributes to the formation of nanofibers without beads.[82] Fong and co-workers study the effect of surface tension on poly(ethylene oxide) (PEO) by varying distil water and ethanol. They observed that by changing the solvent from pure water to a water-ethanol mixture, smooth fibers with larger diameter were produced. The increase of ethanol concentration has led to an increase in solution viscosity and the surface tension lower.[72] This has increased the filament diameter, which is associated with the decrease in net charge density and smaller charge repulsion force.[72]

(b) Processing parameters

Processing conditions such as voltage, distance between the needle and collector, applied voltage, volumetric flow rate, and type of collector can affect the electrospinning process. The applied voltage has more effect on the formation of the droplets shape, and jet released to the collector during the electrospinning process. An increase in the applied voltage leads to the polymer jet discharged with strong repulsion, causing it to undergo higher levels of drawing

stress.[83] High voltage induces more charges to form in the solution. Hence more jet is released from the needle. Higher voltage accelerates more volume with relative small Taylor cone, thereby an increase in the flow rate of the solution and faster electrospinning process.[34] High applied voltage leads to a less control of electrospinng process, and small fibers with a wide diameter distribution. An optimal voltage is required to initiate the polymer jet from the Taylor cone apefex.[42] To stabilize the Taylor cone, the flow rate needs to be adjusted in a correct range. Vacuum usually form due to slow rate in the needle, causing the Taylor cone to disappear and temporarily stop the electrospinning process. Faster flow rate may build up solution at the needle tip. As flow rate increases, the surface charge density decreases. Hence, the charge withdrawal into the solution depends on the resident time of ions in contact with the needle. A constant and stable flow rate is required to minimize the bead formation in electrospinning materials.[84] Slow flow rate reduced the diameter of electrospun nanofibers.[76] Also, slow flow rate resulted in fewer numbers of beads and smaller diameter compared to faster flow rate.[85]

The needle tip to collector distance is another parameter which affect the diameter and morphology of fibers. The fiber morphology could be easily affected by the distance as a result of deposition time, evaporation rate, and the whipping.[86] Ghelich and co-workers studied the effect of the needle tip to collector distance (8, 10, and 15 cm) using a composite of polyvinyl alcohol/nickel oxide-gadolinium doped ceria (PVA/NiO-$Ce_{0.8}Gd_{0.2}O_{1.9}$).[87] At smaller needle tip to collector distance (8 cm), nanofibers with networks were formed because of bind between the inner and outer layers. This can be attributed to remaining solvent residue because of little time for evaporation to take place. When the distance was increased to10 cm, the solvent had enough time to evaporate. This leads to the formation of well-separated fibers. When the distance was increased to 15 cm, the average fiber diameter and the fibers were tangled together. The increase in diameter was attributed to the reduction of the electrostatic field strength, and hence fibers were less stretched.[87] Some researchers reported that imperfect and larger diameter nanofibers are formed at smaller distance.[88] On the other hand, an increase in distance results in a decrease in diameter of the nanofibers.[86] This can be attributed to the complete solvent evaporation and more stretching which leads to the formation of thinner fibers.[89] However, others reported that there is no effect on the morphology of the nanofibers observed with change in the distance between the metallic needle and collector.[90]

(c) Environmental parameters

Environmental parameters such as relative humidity, temperature, and air velocity can also affect diameter and morphology of the nanofibers.[91] Humidity is associated with solidification

process of the charged jet. However, this phenomenon is dependent on the chemical nature of the polymer. The change in humidity can lead to the different size of nanofiber diameter.[92] Pelipenko's group studied the change in nanofibers diameter with a change in humidity using PVA, PEO and their blend solution PVA/hyaluronic acid (HA), PEO/chitosan (CS)). The diameter of nanofibers decreased from 667 to 161 nm (PVA), and 252 nm to 75 nm (PEO) with an increase in humidity from 4% to 60%. The decrease in fiber diameter with humidity was even more in the blend, from 231 to 46 for PVA/HA, and from179 to 41 for PEO/CS from 4% to 50% respectively. Further increase in humidity led to beads fiber for individual polymers and almost no electrospinning for blends.[92] Vrieze and co-workers used poly(vinylpyrrolidone) (PVP) and cellulose acetate (CA) to study the effect of humidity on electrospinning.[93] The average diameter of PVP nanofibers was decreased with increase in relative humidity due to thinner nanofibers. However, at higher relative humidity (60%) no fiber formation, because PVP-ethanol solution absorbs ambient moist during electrospinning. The nanofibers were combining leading to a larger diameter or beaded. For CA nanofibers, it was observed that the diameter of nanofibers was increased with relative humidity. This was associated with polymer precipitation of CA solution in acetone: N, N-dimethylacetamide as water is being added. It was concluded that the relative humidity results in thinner or thicker nanofibers depending on the chemical nature of the polymer.[93]

Humidity also plays a crucial role in the creation of porous nanofibers when the binary solvent system is used. Jeun group studied the effect of humidity on the electrospinning of poly(L-lactide-co-D, L-lactide) fibres.[94] The fibers prepared at low humidity (30%) resulted into smooth, and non-porous PLDLA fibers. A further increased in humidity (50%) resulted into fibers with pore randomly distributed on the surface. At humidity (70%) has led to a formation of non-uniform shaped fibers with a larger pore on the surface. They observed that an increase of humidity was associated with an increase in the number of pores on the surface, the pore diameter, and the pore size distribution.[94] When a hydrophobic polymer is electrospun, water acts as a non-solvent. Due to solvent evaporation, a dry polymer film is formed around the liquid jet. Consequent, pores are formed to enable the evaporation of trapped solvent molecules and complete nanofiber solidification.[95] Bae et al. used PMAA and binary solvent system (dichloromethane (DCM): dimethylformamide (DMF) in 8:2 ratio to produce highly porous nanofibers.[96] The creation of the pores was attributed to the different evaporation rate of the solvent. The more volatile solvent (DCM) start to evaporate faster than the less volatile solvent (DMF) (while the fibers are flying towards the collector). This difference in rates of

evaporation of the two solvents causes a cooling a phenomenon like perspiration. This cooling effect results in the condensation of water vapor into water droplets (as also observed during cloudy conditions or in fog). The water droplets settle on the fibers. As water is immiscible with DMF, hence the two mix well with each other in the inner and outer surface of the fiber. The complete evaporation of the solvents and the water droplets from the fibers results in the formation of porous PMAA electrospinning fibres.[96]

Temperature is the most studied ambient parameter, because of its influence on the solution viscosity and solvent evaporation rate.[93] Temperature causes two opposite effects to change the average diameter of the nanofiber: (i) it increases the rate of evaporation of solvents and (ii) it decreases the viscosity of the solution. The increase in the evaporation of the solvent and the decrease in the viscosity of the solution work by two opposite mechanisms, however, both lead to decrease in the mean fiber diameter. A similar observation was reported by Vrieze et al, using cellulose acetate (CA) and poly(vinylpyrrolidone) (PVP).[93]The effect of temperature was attributed to: first, the evaporation rate of the solvent was decreased (ethanol) exponentially with temperature (at a lower temperature). Thus, the jet takes a longer time to solidify and continuing the elongation of the jet. Second the rigidity of the polymer chain. The polymer chains have more freedom to move at higher temperatures, resulting in lower viscosity. This leads to higher stretching rate and thinner fibers.[93]

Cheng group used Acyclovir(ACY)-loaded PAN fibers dissolved in dimethyl sulfoxide to study the effect of temperature.[97] As the temperature was increased, the viscosities and surface tension of the solution gradually increased. The conductivities of the solution were increased with temperature. When the electrospinning temperature was raised, the solution became less viscous, the solvent DMSO was easier to evaporate, and the presence of ACY could increase the electronic conductivity. This resulted in the improved electrospinning ability of the solution.[97] Thus raising the temperature of the spinning solution can control the evaporation rate of the organic solvent, and smoothen the electrospinning process.[97]

Desai group studied the effect of spinning temperature on the chitosan/poly(acrylamide) blends fibers.[98] The blowing of stifling air around charged polymer solution increases the temperature, which leads to a reduction in viscosity, and an increased evaporation rate of the solvent. Thus, air blowing rate improved fiber formation as the spin-draw ration allowed further stretching of the charged polymer jet during the whipping process.[99]

Yang group studied the effect of working temperature on the polyacrylonitrile (PAN) and polyvinylpyrrolidone (PVP) nafibers.[100] The formed nanofibers became smooth, and their size

decreased as the temperature was increased from 20 to 60 °C.[100] However, as the temperature was further raised to 80 °C, the average size if PAN nanofiber increased. An increase in temperature results in a decrease in viscosity of polymer solution. The same trend was observed with PVP nanofibers. This is associated with a decrease in viscosity and surface tension as the working temperature was gradually increased. These decreases result to an easy electrical drawing of polymer solution jet and fine nanofiber. However, as the temperature increases to an inflection point, the rapid solvent evaporation dominates and increases nanofibers.[100]

Kim and co-workers studied the effect of collector temperature on the poly(L-lactide), polystyrene (PS), and poly(vinyl acetate) (PVAc) nanofibers.[101] The pore size nanofibers increased with collector temperature, and this behavior can be attributed to the boiling point of the solvent used methylene chloride (CM). The topology such as pore size, pore depth, and distribution of the pore was strongly dependent to both boiling point of the solvent and the Tg of the polymer.[101]

2.4 Applications of nanocomposites

2.4.1 **Drug delivery**

Electrospinning can provide the ability to conveniently incorporate therapeutic compounds into the electrospun fibers for preparing useful drug delivery devices. Electrospun fibers have high surface area to volume ratio, high porosity and can be easily functionalized.[102] Hence, fiber mats can overcome drug loading limitations encountered in with other drug delivery systems. Many methods are using in loading drugs such as coating, embedding, and encapsulating.[102] These techniques can be used to control the drug release kinetics.[74] Nanofibers loaded with drugs can be prepared in both degradable and non-degradable polymers.[102] Many material such as antibiotics,[103] anticancer drugs,[104] proteins,[105] and DNA[106] can be encapsulated with different types of drugs. Kenawy and coworkers[107] pioneered the use of poly(ethylene-co-vinyl acetate), poly (lactic acid) fiber mats in the release of tetracycline hydrochloride.

2.4.2 **Tissue Engineering**

Electrospun fibers can mimic extracellular matrix and are often used as the scaffold for cell growth in the area of tissue engineering and tissue regeneration.[108] Nanofibers can find more application in tissue engineering, because of their highly porous structure with large surface area, and their surface properties can be modified. Hence, there are suitable for tissue engineering. Qiu group[109] prepared copolymer nanofibers of caprolactone and lactide as

scaffolds for vascular tissue engineering. Ma and co-workers[110] prepared surface modified electrospun PET fibers for use in blood vessel engineering. Zhu group prepared highly porous nanofibers mats for skin tissue engineering.[111] Chen and co-workers[112] used collagen/chitosan polymers to prepared biocompatible nanofibers, which had an activity for wound healing. Prabhakaran and coworkers[113] prepared PCL/collagen nanofibers for nerve tissue engineering. Fibers of Hydroxyapatite (HA) were highly crystallized and were capable of guiding bone regeneration.[114] Researchers also immobilized growth factors on electrospun poly(lactic-co-glycolic acid) (PLGA) as tendon and cartilage tissue scaffolds.[115]

2.4.3 Antibacterial materials

Electrospinning techniques can allow preparation of nanofibers with antibacterial properties.

Electrospun nanofibers can be easily tailored to have antibacterial property by incorporating antibacterial agents such as silver and copper metals.[116] Nanofibrous mats incorporated with silver nanoparticles in the solution show excellent biocidal activity.[117] Son and coworkers prepared cellulose acetate/silver fibers using cellulose acetate solution with silver nitrate and further reduce to into Ag nanoparticles.[118] Silver-imidazole complexes were loaded in the electrospun fibers to enhance their antibacterial activity.[119] These fiber mats can be used to control the release of nanosilver, which leads to better antibacterial activity.[120] Ren group prepared polyacrylonitrile nanofibers loaded with N-calamine as rechargeable antibacterial activity.[11]

2.4.4 Filters and membranes

Electrospinning allows preparation of fiber mats with controllable porous structure and surface morphology. These materials have potential application in filtration and ultrafiltration.[120] Many polymers which include Polysulfone,[121] poly(vinyl alcohol),[122] poly(acrylonitrile)[123] has been used in the filtration of both particles and solvent. Amongst many techniques used, multi-layers setup is the most efficient and reliable.[123] Yoon and coworkers used a membrane with multi-layer which includes: water permeable and nonporous hydrophilic coating (chitosan), an electrospun nanofibrous support layer (polyacrylonitrile) for mechanical strength, and a non-woven microfibrous substrate (polyethylene terephthalate).[123] The membrane was used to separate water and oil and had rejection efficient of higher than 99.9%. The superhydrophobic membranes can be fabricated by using nanoparticle[124] and co-axial electrospinning.[125] This membrane can be used in ultrafiltration, self-cleaning textiles, and construction materials.[120]

2.4.5 **Sensors**

Electrospun nanofibers have been used as a sensory device, because of their enhanced charge transport, and high functionality.[126] Many sensors which including chemical sensors,[127] optical sensors,[128] and biological sensors[129] have been fabricated using electrospun fibers. Electrospinning of polymers can fabricate the sensor devices with sensor properties or without sensor properties and loaded with a compound having sensor properties (nanomaterials, fluorescent dyes, and enzymes). Wang group used polyvinyl alcohol embedded with Zinc Oxide nanofibers for gas sensors. They show high selectivity and sensitivity to ethanol.[130] Yoon and coworkers[128] used poly(ethylene oxide) and tetraethyl orthosilicate embedded with polydiacetylene to prepare nanofibers. The sensors fabricated from these nanofiber mats can be used to differentiate colors of some common solvent.[128]

2.4.6 **Catalysis**

Electrospun nanofibers are versatile and widely used in catalysts or as catalyst support.[131] Nanofiber mats are characterized by high surface area to volume ration and small inter-fibrous pores with high porosity. These properties have led them to be used as catalyst or catalyst support. Electrospun nanofibers can be loaded with both organic and inorganic catalyst. The activity of nano-catalyst can be protected by the polymer matrix of the nanofiber.[132] The Fe-TO_2/SnO_2 nanofibers were used as the photocatalyst in many environmental problems.[133] Sakai group prepared nanofibrous mats of polystyrene incorporated with an enzyme (lipase) to enhance its performance.[134]

2.5 Metal oxide, metal selenide, and poly(methyl methacrylate)

Silver is known for its antibacterial property, low cytotoxicity, excellent stability, and less development of resistance strains.[135] Many studies have focused on the use of silver-based nanomaterials in medical materials and devices to prevent infection which includes wound dressing,[136] burn ointments,[137] catheters,[138] vascular grafts,[139] and bone fixation devices.[140] Oxide of silver is known for their conductivity and exist in many oxidation states (Ag^+, Ag^{2+}, Ag^{3+}).[141] Ag_3O_4 has a mixed valence state (Ag_2O_3 and AgO). It can undergo electrochemical redox reaction to the form metallic silver ($Ag_3O_4 \rightarrow AgO \rightarrow Ag_2O \rightarrow Ag$).[142] Silver oxide nanomaterial can find its application in many fields such as catalysis,[143] sensors,[144] antibacterial materials,[145] photovoltaic devices,[146] optical storage devices,[147] plasmonic photonic devices,[148] and drinking water.[149] It is an intrinsic p-type semiconductor with a band gap of about 1.5 eV.[150]

Silver selenide (Ag_2Se) undergoes a polymorphic transition to a low-temperature orthorhombic structure (β-Ag_2Se) and high-temperature body-centered cubic structure (α-Ag_2Se) at about 409 K.[151] The β-Ag_2Se phase is characterized as an n-type semiconductor, narrow bandgap with an energy gap between 70 meV and 150 meV.[152] It has high see beck coefficient, low lattice thermal conductivity, and high electrical conductivity.[153] It can be used as the photosensitizer in photographic films, in thermochromic materials and thermo electronics [154]. The α-Ag_2Se is a superionic conductor. It has been used as a solid electrolyte in photo chargeable secondary batteries, the additive in highly conductive composite glasses for batteries, sensors, and displays.[155] Nonstoichiometric $Ag_{2+\delta}Se$ show giant magneto-resistance comparable to the colossal magneto-resistance observed in manganese perovskites.[156] It can be used in magnetic field sensing devices, more specific to low field sensors.[157]

Copper-based compounds are known for their biocidal properties which include antimicrobial, antibiotic and antifungal agent.[158] Copper oxide exists in three stoichiometric which include: cuprous oxide (Cu_2O, cuprite), cupric oxide (CuO, tenorite), and Cu_4O_3 (paramelaconite) with their crystalline forms.[159] Copper oxide is a p-type semiconductor with a narrow band gap in the range between 1.2 to 2.5 eV depending on their stoichiometry.[160] Copper oxide shows unique physical, electronic, and photonic properties[161] which lead to its application in sensors, catalysis, batteries, high-temperature superconductors, solar energy, and magnetic storage media.[162] Copper selenide can exist in various stoichiometry (Cu_2Se, Cu_5Se_4, Cu_7Se_5, $Cu_{2-x}Se$, CuSe, $CuSe_2$, and Cu_3Se_2) with many structural forms which include cubic, hexagonal, tetragonal, orthorhombic, and monoclinic.[163] Copper selenide is p-type semiconductors characterized by direct bandgap between 2.0 eV and 3 eV, and indirect band gap in the range of 1.1-1.7 eV.[164] Copper selenide has been widely applied in fields such as quantum-dots sensitized solar cell, window material, the optical filter, superionic conductor, lithium or sodium-ion batteries, electrocatalysis, electro-optical devices and thermoelectric converter.[165]

The iron-based material is less toxic, biodegradable, environmentally friendly, biocompatible, and tunable magnetic properties.[166] Iron oxide is known to exist in many forms which include Magnetite (Fe_3O_4), maghemite(γ-Fe_2O_3), hematite (α-Fe_2O_3), wustite (FeO), β-Fe_2O_3, and ε-Fe_2O_3.[167] Magnetite (Fe_3O_4), maghemite(γ-Fe_2O_3), hematite (α-Fe_2O_3) are the most dominant because of their temperature-induced phase transition polymorph.[168] Hematite (α-Fe_2O_3) is the most stable and is an n-type semiconductor with a band gap of 2.3 eV. It is a low cost and show high resistant to corrosion. It can be used in the synthesis of magnetite and maghemite. Magnetite has both divalent and trivalent iron. It is both an n- and p-type semiconductor with

a small bandgap of 0.1 eV. It is known to have low resistivity. Maghemite is an n-type semiconductor with a band gap of 2.0 eV.[167] They are widely applied in many fields which include catalysis, magnetic recording, high performance electromagnetic, spintronic devices, magnetic resonance imaging (MRI), cell and protein separation, information storage, sensors, lithium-ion battery, supercapacitor electrode material, wastewater purification, and drug delivery.[169] Iron selenide has many phase compositions which include Fe_7Se_8, Fe_3Se_4, $FeSe_2$, α-FeSe, and β-FeSe, with their crystallographic structures such as hexagonal, monoclinic, tetragonal, and orthorhombic.[170] Iron selenide can be a semiconductor or superconductor due to its ferro/ferromagnetic behavior depending on phase.[171] It has also been used in solar cell ($FeSe_2$).[172] It has a band gap of either 0.14 or 3.0 eV depending on the phase. FeSe exhibit two transitions which are dependent on growth temperature, below 450 °C as α-FeSe (tetragonal) and above 450 °C as β-FeSe (hexagonal).[173] They show both n- to p-type conduction behavior depending on their atomic ration.[174]

Poly(methyl methacrylate) can be recognized as both hydrocarbon and ester, and named as poly[1-(methoxycarbonyl)-1-methyl ethylene], and poly(methyl-2-methyl propanoate) respectively.[175] Poly(methyl methacrylate) is an amorphous, optically clear thermoplastic belonging to the acrylate.[176] It can be synthesized using methyl methacrylate monomer.[177] It has a moderate thermal stability with a glass transition temperature range of 100 to 130 °C and can withstand temperature between 100 and -70 °C.[176] PMMA exhibit high impact strength, lightweight, shatter-resistance with favorable processing conditions.[178] These properties have led to PMMA being used as the substitute for inorganic glass.[179] It has high resistance to sunshine exposure, and high scratch resistance.[175] It is very resistance to most chemicals, and low resistance to chlorinated, aromatic hydrocarbons, esters and ketone.[180] It is widely applied in many fields which includes optical, pneumatic actuation, sensor, analytical separation, conductive devices, biomedical, polymer electrolytes, polymer viscosity, and drug deliver.[181] It is commercially known with different trade names such as lucite, oroglas, Perspex and Plexiglas.[179] The fiber of PMMA can be limited because of its thermal stability and inability to filter ultraviolet light.[182] However, polymers reinforced with nanoparticles,[183] micro-sized fiber,[184] and cellulose nanocrysatls[185] show enhance thermal and mechanical properties.

Chapter Three

3 Experimental

3.1 Materials

Copper chloride (97 %), silver nitrate (99.2 %), methanol (99.5 %), hexadecylamine (HDA) (90 %), trioctylphosphine (TOP) (90 %), toluene (99.5 %), p-iodonitrotetrazolium chloride (INT), and poly(methylmethacrylate) (M =350000) were purchased from Sigma Aldrich. Sodium borohydride (95 %), urea (99 %), dimethylformamide (DMF) (99.5 %) and diphenyl diselenide (97 %) were purchased from Merck. Ethanol (99.9 %) and diethyl ether (99 %) were purchased from CC Imelmann, and Rochelle Chemicals. Muller-Hinton broth and Muller-Hinton agar were purchased from Neogen (Michigan). Staphylococcus aureus (ATCC 25923) and Enterococcus faecalis (ATCC 29212) (Gram positive bacteria strain). Klepsiella pneumoniae (ATCC 13883), and Pseudomonas aeruginosa (ATCC 15442) (gram negative bacteria strain). Candida albicans (ATCC 14053) and Crytococcus neoformans (ATCC 14116) (yeasts) were bought from Anatech (South Africa). These chemicals were used without any further purification.

3.2 Experimental Procedure

3.2.1 Synthesis of copper complexes using diphenyldiselenide ligand

Diphenyl diselenide (3.14 g, 10 mmol) was dissolved in ethanol (20 ml). Sodium borohydride (0.25 g) was added into the solution. This solution was refluxed while stirring under inert environment until the yellow solution became colorless. Copper chloride (0.67 g, 5 mmol) dissolved in ethanol (20 ml) was mixed with diphenyl diselenide solution. The mixture was refluxed for four hours. The resultant precipitates were filtered, washed with diethyl ether and allowed to dry in the desiccator.

3.2.2 Synthesis of iron complexes using diphenyldiselenide ligand

Diphenyl diselenide (3.14 g, 10 mmol) was dissolved in ethanol (20 ml). Sodium borohydride (0.25 g) was added into the solution. This mixture was refluxed while stirring under inert environment until the yellow solution became colorless. Iron (III) chloride hexahydrate (1.35 g, 5 mmol) dissolved in ethanol (20 ml) was mixed with diphenyl diselenide solution. The

mixture was refluxed for four hours. The resultant precipitates were filtered, washed with diethyl ether and allowed to dry in the desiccator.

3.2.3 Synthesis of silver complexes using diphenyldiselenide ligand

Diphenyl diselenide (3.14 g, 10 mmol) was dissolved in ethanol (20 ml). Sodium borohydride (0.25 g) was added into the solution. This mixture was refluxed while stirring under inert environment until the yellow solution became colorless. Silver nitrate (0.85 g, 5 mmol) dissolved in ethanol (20 ml) was mixed with diphenyl diselenide solution. The mixture was refluxed for four hours. The resultant precipitates were filtered, washed with diethyl ether and allowed to dry in the desiccator.

3.2.4 Synthesis of iron complexes using urea ligand

Iron(III) chloride (2.70 g, 0.01 mol) dissolved in 25 ml of methanol was mixed with solution of urea (6.0 g, 0.1 mol) dissolved in 25 ml. The mixture was allowed to reflux at 60 °C for six hours. The resultant precipitates were filtered, washed with diethyl ether and allowed to dry in the desiccator.

3.2.5 Synthesis of silver complexes using urea ligand

Silver nitrate (1.7 g, 0.01 mol) dissolved in 25 ml of methanol was mixed with solution of urea (6.0 g, 0.1 mol) dissolved in 25 ml of methanol. The mixture was allowed to reflux for six hours. The resultant precipitates were filtered, washed with diethyl ether and allowed to dry in the desiccator.

3.2.6 Synthesis of metal selenide nanoparticles

Copper selenide nanoparticles were synthesized by thermal decomposition of copper complex. A mass of the complex (0.125 g) was dissolved into trioctyphosphine (TOP) (5 ml). The solution was injected into hot hexadecylamine (HDA) (5.0 g) which was heated and maintained at temperature of 150° C under nitrogen atmosphere. This reaction was maintained at this temperature with constant stirring for an hour minutes. Then, the solution was cooled to 70 °C and an excess of methanol was added. The precipitates formed were isolated by a centrifuge, washed with methanol three times to remove some of the capping agent and allowed to dry. In the preparation of iron selenide nanoparticles, the copper complex was replaced by iron complexes. The same procedure was done for silver selenide nanoparticles. The other conditions were kept the same as for copper selenide nanoparticle preparation.

3.2.7 Synthesis of copper oxide nanoparticles

Copper acetate monohydrate (0.125 g) was placed inside a small, square piece of aluminum foil. The foil was placed in the glass tube and put into the furnace purged with nitrogen. The sample was calcined for 1 hour at a temperature of 400 °C. After 1 hour, the sample was cool to room temperature while inside the furnace. Then, the sample was ready to be characterized.

3.2.8 Synthesis of metal oxide nanoparticles

Silver oxide nanoparticles were synthesized by thermal decomposition of silver complex. Silver complex (0.125 g) was dissolved into trioctyphosphine (TOP) (5 ml). The solution was injected into hot hexadecylamine (HDA) (5.0 g) which was heated and maintained at temperature of 150° C under nitrogen atmosphere. This reaction was maintained at this temperature with constant stirring for an hour. Then, the solution was cooled to 70 °C and an excess of methanol was added. The precipitates formed were isolated by a centrifuge, washed with methanol three times to remove some of the capping agent and allowed to dry. The same procedure was adopted for the preparation of iron oxide nanoparticles, the silver complex was replaced by iron complexes respectively. The other conditions were kept the same.

3.2.9 Preparation nanofibers

Poly(methyl methacrylate) in dimethylformamide (PMMA/DMF) (2 g in 20 mL corresponding to 10 wt %) solution were mixed for 12 h by stirring at room temperature. Copper selenide nanoparticles (0.02 and 0.4 g corresponding to 0.1 and 2 wt % respectively) were separately added into PMMA solutions and stirred for 12 h. The PMMA/DMF solutions containing CuSe nanoparticles were loaded into a glass pipette. A copper wire was inserted into the polymer solutions and connected to the positive electrode of high voltage. The negative electrode was connected to the plastic plate rapped with aluminum foil and used as a collector. The separation distance between the needle and collection plate, and applied voltage were held constant at 20 cm, and 20 kV, respectively. The electrospinning process was done in a horizontal mode in a fume hood at room temperature.

The same procedure was used to prepared PMMA-AgSe and PMMA-FeSe, PMMA-CuO, PMMA-AgO and PMMA-FeO, by replacing CuSe nanoparticles with AgSe, FeSe, CuO, AgO, and FeO respectively.

3.2.10 Antibacterial Activity for nanoparticles

The Muller Hinton Broth (20 g) was dissolved into 1 liter of distilled water. The mixture was sterilized in the autoclaved for 45 minutes. The nutrient broth (50 mL) was transferred into

each four Erlenmeyer flasks. The bacteria (S. aureus, E. faecalis, K. pneumoniae, and P. aeruginosa) were subculture to four flasks with nutrient broth respectively. The flasks were covered with cotton wool and aluminum foil, and then autoclaved for 45 minutes. The flasks were cooled to 60 °C and inoculate into the safety cabinet to avoid contamination. The bacteria were added into each flask respectively to get about 10^6 colony forming unit (CFU/mL). The solutions were incubated for 24 hours.

The antibacterial activity of silver selenide, silver oxide, copper selenide, copper oxide, iron selenide, and iron oxide nanoparticles were studied using the Microbroth dilution test. The method involves the use of polystyrene tray containing 96-wells microliter. The nutrient broth (100 µL) was transferred to each well. The nanoparticle solution (100 µL) was also added to each well with nutrient broth on the first row except for the controls (positive and negative). Then, two-fold serial dilution were prepared by transferring 100 µL solution in the first row to the following well in the next row in a serially descending concertation. On the last raw 100 µL solution was removed on the last row, so that all the 96-well had the same volume. Bacterial solution (100 µL) was added to each well, except the column for the control (no bacteria). The positive control column contains nutrient broth (100 µL), and neomycin (100 µL) in place of nanoparticles. The negative control column had only nutrient broth (200 µL) and is free of antibiotics or nanoparticles. The no bacteria control column contains nutrient broth (100 µL), and nanoparticles (100 µL) without any bacterial solution. The three controls were serial diluted using two-fold serial dilution method. All the plates were cover with parafilm and incubated at 37 °C for 24 hrs. The p-iodonitrotetrazolium chloride (INT) solution (50 µL of 0.2 mg. mL^{-1}) was added to all the well as the indicator. The plates were further incubated at 37 °C for another 24 hrs.

3.2.11 **Antifungal activity for nanoparticles**

The yeasts (C. albicans, and C. neoformans) (400 µL) were added to the 4 mL of sterile saline respectively. The absorbances of the solutions were measured and adjusted to be the same as McFarland standard solution. Fungi Mat Extract Broth (yeast) (20 g) was dissolved into 1 liter of distilled water. The mixture (50 mL) was transferred into each of the two Erlenmeyer flasks. The flasks were covered with cotton wool and aluminum foil and autoclaved for 45 minutes. Then, cooled to 60 °C and inoculate in the safety cabinet to avoid contamination. The yeasts (50 µL) was added to the Erlenmeyer flask respectively and incubated at 37 °C for 24 hours.

The 96-well was labelled rows (A to H) and columns (1 to 12). The yeast broth (100 µL) was transferred to each well. The nanoparticle solution (100 µL) was also added to each well with nutrient broth on the first row (A) except for the controls (positive: column 7, and negative: column 8). Then, two-fold serial dilution were prepared by transferring 100 µL solution in the first row (A) to the following well in the next row (B) in a serially descending concertation until column (H). On the last row 100 µL solution was removed on the last row (H), so that all the 96-well had the same volume. Bacterial solution (100 µL) was added to each well, except for no bacteria control (column 9). The positive control column contains amphotericin B (100 µL) in place of nanoparticles. The water was used as the negative control. The no fungi control column contains yeast broth (100 µL), and nanoparticles (100 µL) without any bacterial solution. The three controls were serial diluted using two-fold serial dilution method. All the plates were cover with parafilm and incubated at 37 °C for 24 hrs. The p-iodonitrotetrazolium chloride (INT) solution (50 µL of 0.2 mg. mL^{-1}) was added to all the well as the indicator. The plates were further incubated at 37 °C for another 24 hrs.

3.3 Characterization

3.3.1 Thermogravimetry

The sample preparation for thermogravimetric analysis (TGA) and derivative thermogravimetry (DTG) was done by weighing 10 mg of the complexes. These complexes were decomposed at temperature range of 50 to 800 °C. This analysis was performed on a Perkin Elmer Pyris 6 TGA under an inert atmosphere of dry nitrogen, and at a heating rate of 20 °Cmin^{-1}.

3.3.2 FT-IR spectroscopy

Infrared spectra were recorded on FT-IR Perkin Elmer 400 spectrometer. Spectra were collected over the range from 400 to 4000 cm^{-1}.

3.3.3 Microanalysis

Elemental analyses (C, H, N) were performed on a Thermo Scientific Flash 2000 CHNS-O analyzer fitted with auto sampler.

3.3.4 Optical characterization

Absorption spectra of the nanoparticles were measured using Perkin Elmer Lambda 25 UV-VIS spectrophotometer in the spectral range of 190-900 nm. The samples were placed in a quartz cuvette (1 cm path length) with toluene as the solvent. Emission spectra of the particles were recorded on a Perkin Elmer LS 45 photoluminescence (PL) spectrometer with a xenon

lamp at room temperature. The samples were placed in glass cuvettes (1 cm) with toluene as solvent.

3.3.5 X-ray diffraction analysis

Powder X-ray diffraction patterns of the samples were recorded using a Shimadzu XRD 700 X-ray diffractometer with Cu Kα radiation (λ=1.54 Å) under the conditions of 40 kV and 40 mA. The samples were mounted flat and scanned between 5◦ and 90◦ in a step size of 0.05◦ with a count rate of 9 s.

3.3.6 Scanning electron microscopy

The fibrous mats were examined by scanning electron microscopy (SEM) (FEI Quanta ESEM). A small section of the mat was mounted to a metal sample stub using double stick electrically conductive carbon tape. The sample was sputter coated with gold.

3.3.7 Transmission electron microscopy

Transmission electron microscope (TEM) analysis was performed using HITACHI JEOL 100S operated at 80 kV. The samples were prepared by placing a drop of dilute solution of sample in toluene on to a copper grid. The sample was allowed to dry completely at room temperature.

Chapter four

4 Results and discussions

4.1 Coordination Complexes

Complexes form coordinate bond between the transition metal and the ligand. Generally, the chalcogens are known to bind to the metals more preferable than other atoms especially those used on the study such as copper, silver and iron. This provides relatively stable bonds that are useful in the thermolysis of the complexes in the approach called single-source precursor to give rise to metal chalocogenides.

4.1.1 Complexes of urea

The urea can coordinate to metal atom with either carbonyl oxygen atom or amide nitrogen atoms.[186] The mode of coordination of urea with metal ion depends upon the type and the nature of metal.[26] In urea-metal complexes, the vibrational spectrum of the complex differs significantly from that of the urea molecule. The N-H, and C-N and C=O stretching frequencies would shift to higher or lower frequencies depending on the coordination of urea to metal ion through oxygen or nitrogen atom. Figure 4-1, and Figure 4-5 represent the infrared spectra of Ag(I), and Fe(II) complexes respectively, and are compared with urea molecule. The infrared spectra show two curves: urea molecule (a) and metal-urea complex (b). Table 4-1 show the most characteristic band vibrations of metal-urea complexes and propose assignments. The urea is characterized by band associated to $\nu(NH_2)$, and C=O functional groups. The $\nu(NH_2)$ exhibits bands at 3429-3320, and 1675 cm^{-1}, associated to the stretching and bending of $\nu(NH_2)$ bonds. In silver complex, the $\nu(NH_2)$ appears at 3466-3168 cm^{-1} higher and lower bands. This wide range indicate that some urea is coordinated through oxygen, while other is coordinated through nitrogen atoms. The $\nu(NH_2)$ bands are higher for urea coordinated through oxygen, and lower for urea coordinated with nitrogen atom. Furthermore, the complex exhibits two bending modes ($\delta_s(NH_2)$ and $\delta_{as}(NH_2)$). This indicates that there are two coordination mode.[187] However, the ν(CO) bands exhibits broad bands at relatively the same range as that of the ligand. This is consistent with the existence of both coordinated and uncoordinated oxygen atom. In iron complex, the $\nu(NH_2)$ bands appears at relatively the same bands as the free ligand.

This indicates that the nitrogen atom was not used in the coordination to iron. However, the *v*(CO) exhibits bands at lower stretching frequency than the free ligand. This indicate that the oxygen is used to coordinate to iron.

Table 4-1: Characteristic infrared frequency and assignment of urea, silver and iron complexes.

Assignments	Urea	Ag(I)	Fe(III)
$\nu_{as}(NH_2)$, *v*(OH), CH_3OH	3429	3466	3427
	3257	3168	3219
	3220		
$\nu_s(NH_2)$, CH_3OH	3330	3377	3328
$\nu(CH_3)$		2980	2928
		2902	2852
$_{\delta}(NH_2)$	1675	1673	1672
		1642	
$_{\nu}$(C=O)	1590	1590	1551
$_{\nu}$(C-N)	1454	1442	1460
	1052	1063	1020

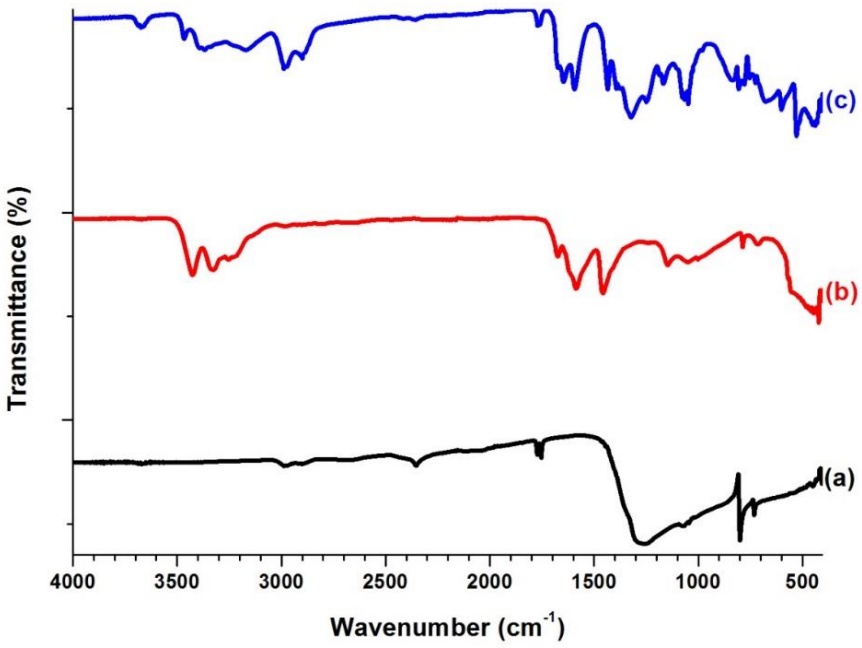


Figure 4-1: The FTIR spectra of silver nitrate (a), urea (b), and silver urea complexes (c).

Figure 4-2 shows the TGA spectra of $Ag_2(U)(NCO)(NO_3)(CH_3OH)$ complex. This complex decomposes into three major steps. The first decomposition occurs at about 183-296 °C. This decomposition leads to a mass loss of 22.83 %, which can be associated with methanol (7.78 %), and nitrate (15.05 %). The nitrate decomposes at slightly higher temperature from methanol. The second decomposition occurs at 387-426 °C and leads to a mass loss of 14.58 % due to urea. The last decomposition at 452-523 °C, which leads to mass loss of nitrogen and carbon dioxide gases. This result to a final residue of 52.03 %, which is quite comparable with two silver metal (52.38 % theoretical). Derivative thermogravimetry confirms three major endothermic peaks of $Ag_2(U)(NCO)(NO_3)(CH_3OH)$ complex. However, there are many small peaks that can be associated with intermediate decomposition of silver complex.

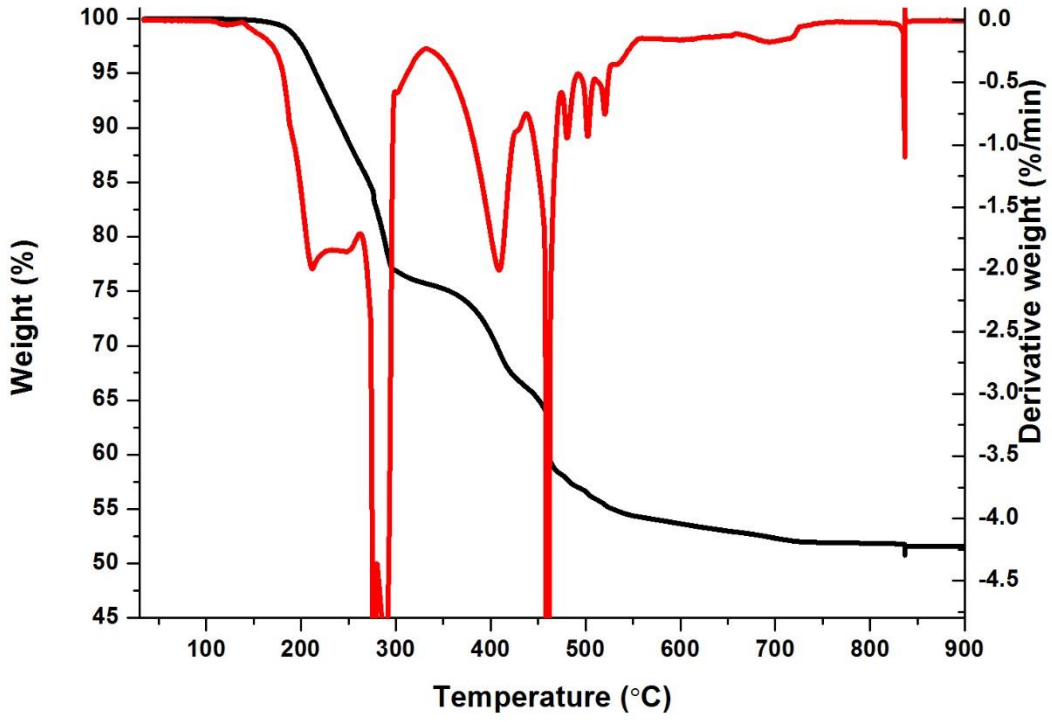


Figure 4-2: The graph for silver urea complex TGA (black) and derivative (red).

Figure 4-3 shows the FTIR spectra of copper acetate monohydrate. The FTIR show three absorption peaks of interest: the first peaks at 3465 -3268 cm^{-1}, due to a hydroxyl group of water and acetic acid.[188] Second peaks at 2993, and 2945 cm^{-1} (weak), which are attributed to methyl group. Third absorption peaks at 1594 and 1417 cm^{-1}, which can be associated to symmetric and antisymmetric carboxylate stretching mode.[189]

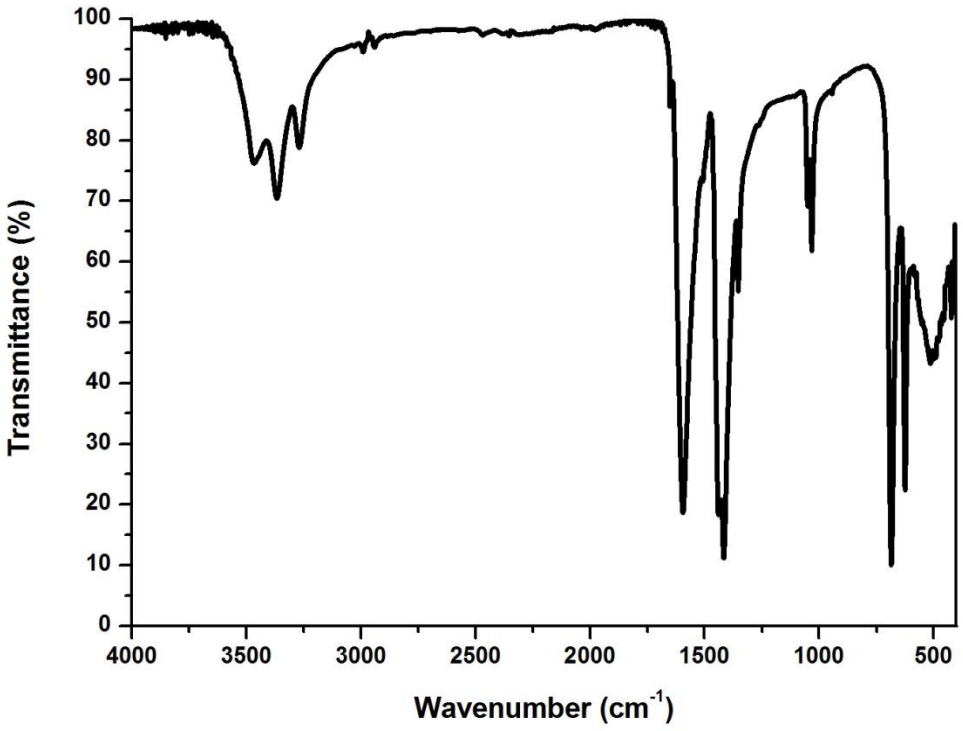


Figure 4-3: The FTIR spectra of copper acetate monohydrate.

Figure 4-4 shows the TGA (black) and DTG (red) curves of copper acetate monohydrate. Copper acetate monohydrate decomposes into two steps.[190] The first decomposition occurs between 111 and 159 °C which is associated with dehydration.[188] The dehydration leads to a mass loss of 8.28 %, and comparable with water molecule theoretical (9.02 %). The second decomposition occurs between 208 and 317 °C, and is due to acetate moiety.[191] The decomposition of acetate results into a mass loss of 59.29 % which is in good agreement with theoretical (59.16 %). A copper residue with a mass of 32.43 % is comparable with theoretical (31.83 %). The DTG (red) shows two endothermic peaks at 143, and 288 °C. The DTG peaks are consistent with dehydration, and decomposition of acetate moiety respectively.[192]

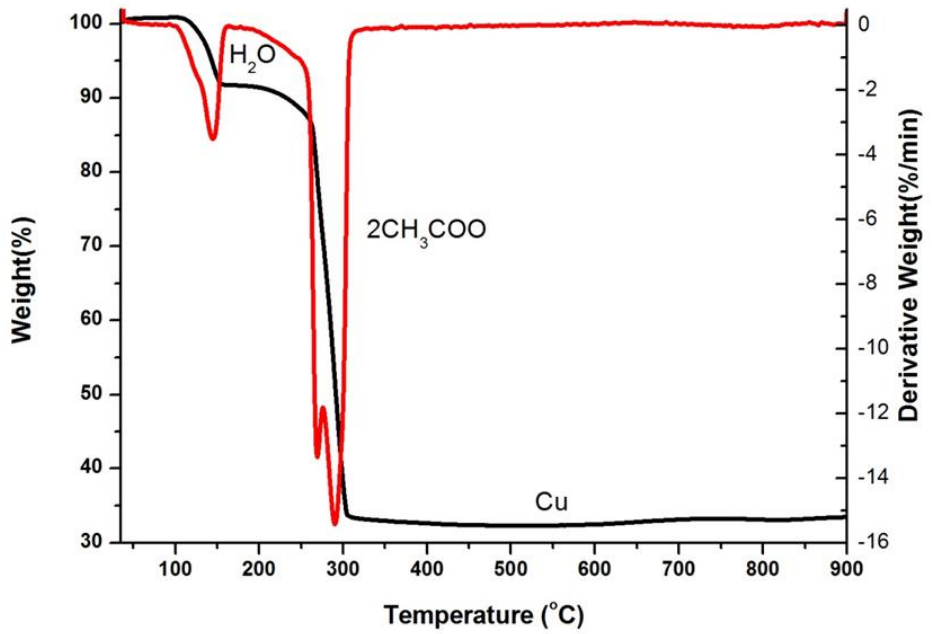


Figure 4-4: The TGA (black) and derivative (red) spectra of copper acetate monohydrate.

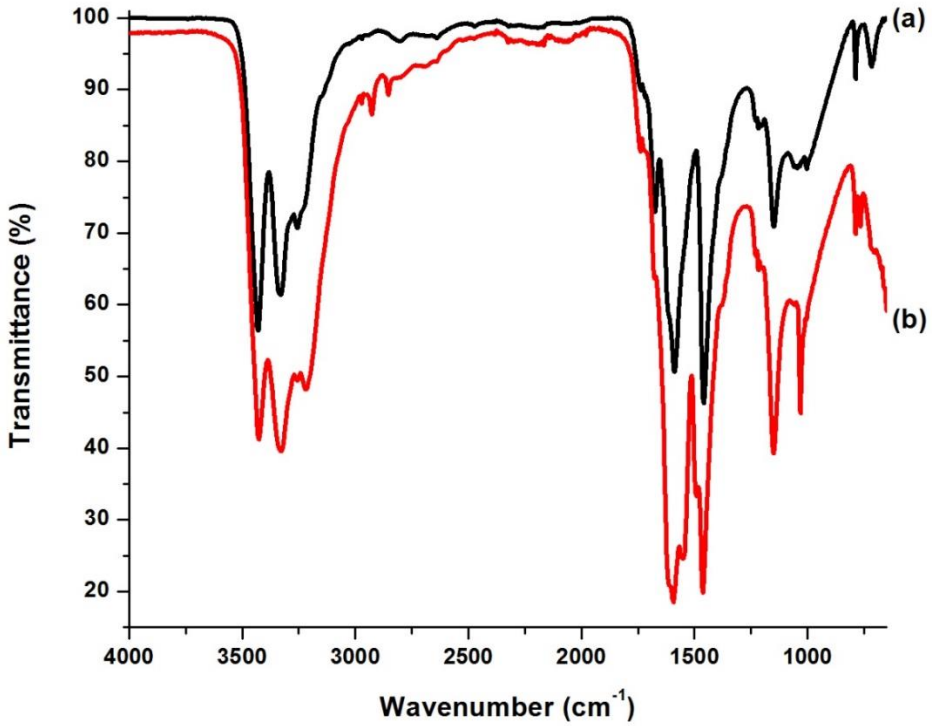


Figure 4-5: The FTIR spectra of urea (a) and iron urea complex (b).

Figure 4-6 shows the TGA graph for iron urea complex. The TGA curve for iron urea complex $[Fe(Cl)_2(U)_3(H2O)_4]$ has four stages of mass loses within the temperature range 34-748 °C and maximum DTG peaks at 44, 237, 335, 690 °C. The first stage is between 34-65 °C and has an experimental mass loss of 3.9 % that is comparable with a theoretical mass loss of 4.75 %. This is consistent with the mass loss of 1 molecular water due to moisture. The second stage is between 136-260 °C and has a mass loss of 37.6 % that is comparable with theoretical mass loss of 36.44 % due to 2 moles of urea and 3 moles of water. The third stage is between 291-429 °C. This decomposition results to an experimental mass loss of 21.79 %, and is comparable with a theoretical mass 20.18 %. This is associated the loss of half Cl_2, half N_2, half H_2, and CN, and results in a residue of FeO. The fourth stage occurs between 661-748 °C, and results in the decomposition of half O_2. This decomposition leads to a final residue of iron. The derivative thermogravimetry shows four major endorthemic peads wich are associated with decomposition of the iron complex. This is in good agreement with the TGA.

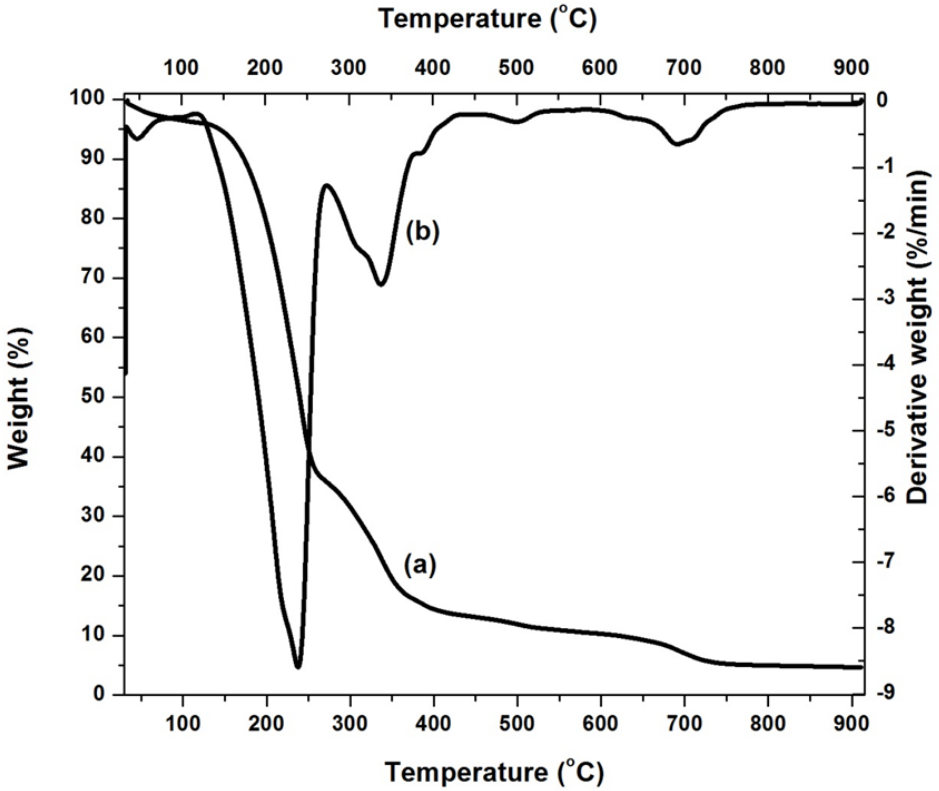


Figure 4-6: The graph of iron urea complex TGA (a), and derivative (b).

4.1.2 **Diphenyldiselenide complexes**

The free ligand diphenyldiselenide exhibits multiple bands in the range of 3069-662 cm^{-1}. The free ligand displays aromatic band vibration at 3069-2983 cm^{-1}, which can be assigned to aromatic stretch of C-H group. An overtone bands at 1975-1633 cm^{-1} and can be associated with C=C stretching frequency. An aromatic band at 1500-1426 cm^{-1}, which can be due to C-C stretch. The bands at 1325-987, and 723-667 cm^{-1} which is associated with C-H in plane bands, and C-H out of plane respectively.

The silver complex shows similar peaks to free ligand (Figure 4-7). An aromatic C-H band occurs at 3055-2851 cm^{-1}. An overtone occurs at 1949-1637 cm^{-1} and can be associated with C=C stretching frequency. A band at 1557-1434 cm^{-1} and can be due to C-C stretching. A broad band at 1364 cm^{-1}, which can be attributed to N-O band. A band at 1283-988 cm^{-1}, and 725-671 cm^{-1} which can be due to in plane and out of plane C-H band respectively.

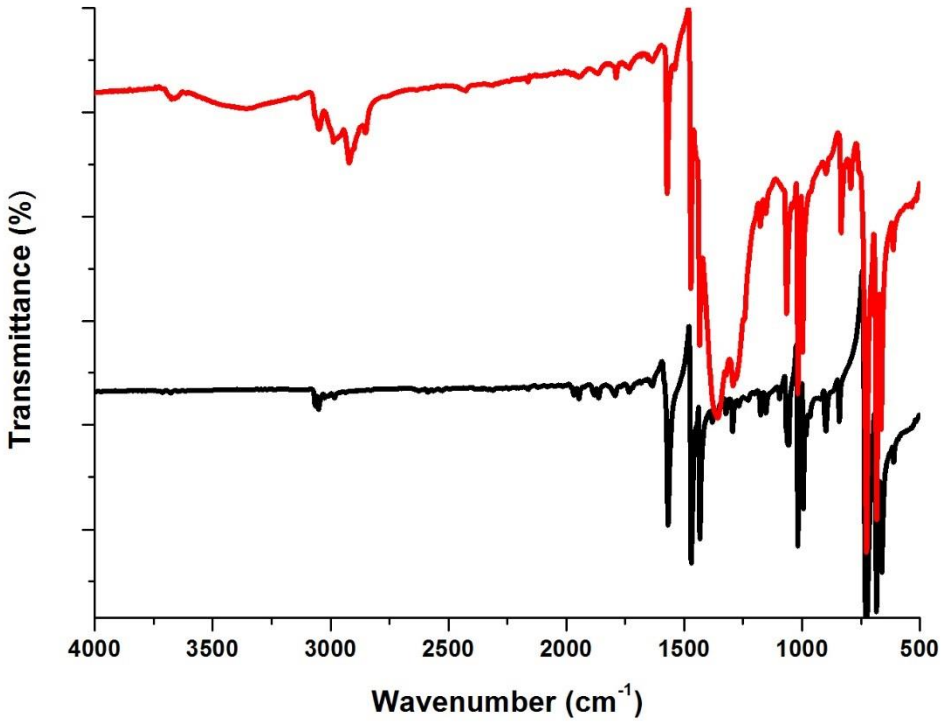


Figure 4-7: The FTIR spectra of diphenyldiselenide (a), and silver diphenyldiselenide complex (b).

Figure 4-8 shows the TGA spectra of silver diphenyldiselenide complex. The complex $(Ag_2(NO_3)_2(C_6H_5Se)_2$ decomposes into three steps. The first decomposition occurs at 95-148 °C. This decomposition was very small (2.74 %) and can be due to solvent attached at surface of the complex. The second decomposition occurs at 221-335 °C. This leads to a major decomposition of the ligand moiety (nitrate and phenyl selenide anion). This results to a residue of 45.88 %, which agrees well with Ag_2Se theoretical mass (45.21%). Another decomposition occurs at 454 °C, and gradual degrade with increase in temperature. The DTG shows three endothermic peaks associated with TGA spectra.

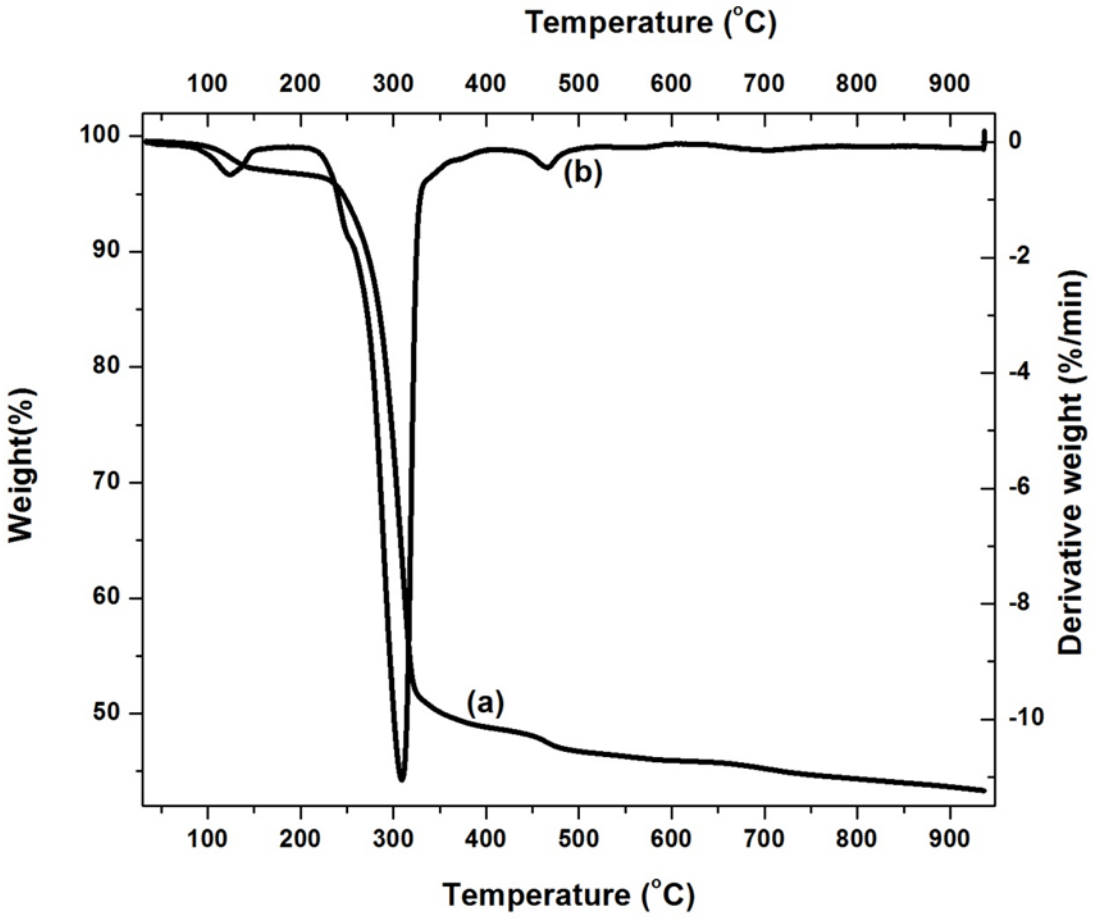


Figure 4-8: The graph (TGA (a), and derivative (b)) of the silver diphenyldiselenide complex.

The copper complex is compared with diphenyldiselenide ligand (Figure 4-9). The spectra show similar bands. There is a band at 3442-3350 cm^{-1}, that can be attributed to O-H group of water molecule. A second band occurs at 3061 cm^{-1} and is assigned to an aromatic C-H stretching. A third band is an overtone at 2158-1976 cm^{-1} and is assigned to C=C stretching. A

fourth band appears at 1627 cm^{-1} and can be due to O-H bending. A firth C-H band appears at 1074-993, and 736-682 cm^{-1}, and are due to in plane, and out of plane stretching respectively.

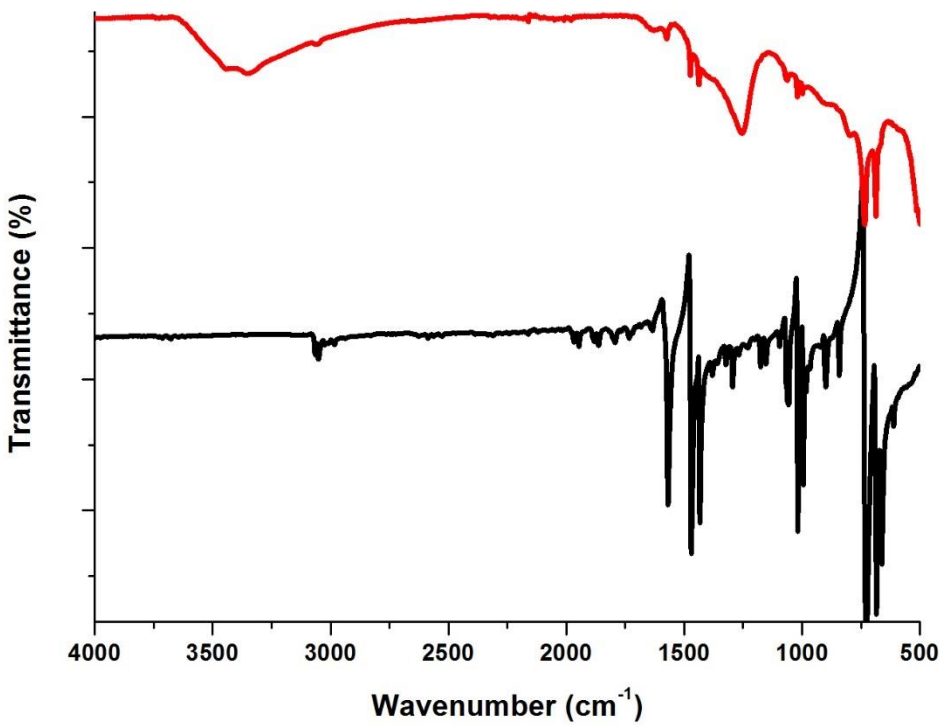


Figure 4-9: The FTIR spectra of diphenyldiselenide (a), and copper diphenyldiselenide complex (b).

Figure 4-10 shows the TGA graph of copper diphenyldiselenide complex. The complex $Cu(Cl)_2(C_6H_5Se)_2$ shows three major pathways. First decomposition occurred at about 139-242 °C. This decomposition results to a mass loss of 15.67 % and can be associated with two moles of chloride. The major decomposition occurs at about 256-383 °C. This decomposition can be associated with loss of phenyl and phenyl selenate anion ligands.

This decomposition results to a residue of 32.80 and is comparable with copper selenide theoretical mass of 31.97%. The last decomposition occurs at 480-646 °C and leads to degradation of the whole compound. This results to a final residue less than 1% which could be remains of decomposed copper metal.

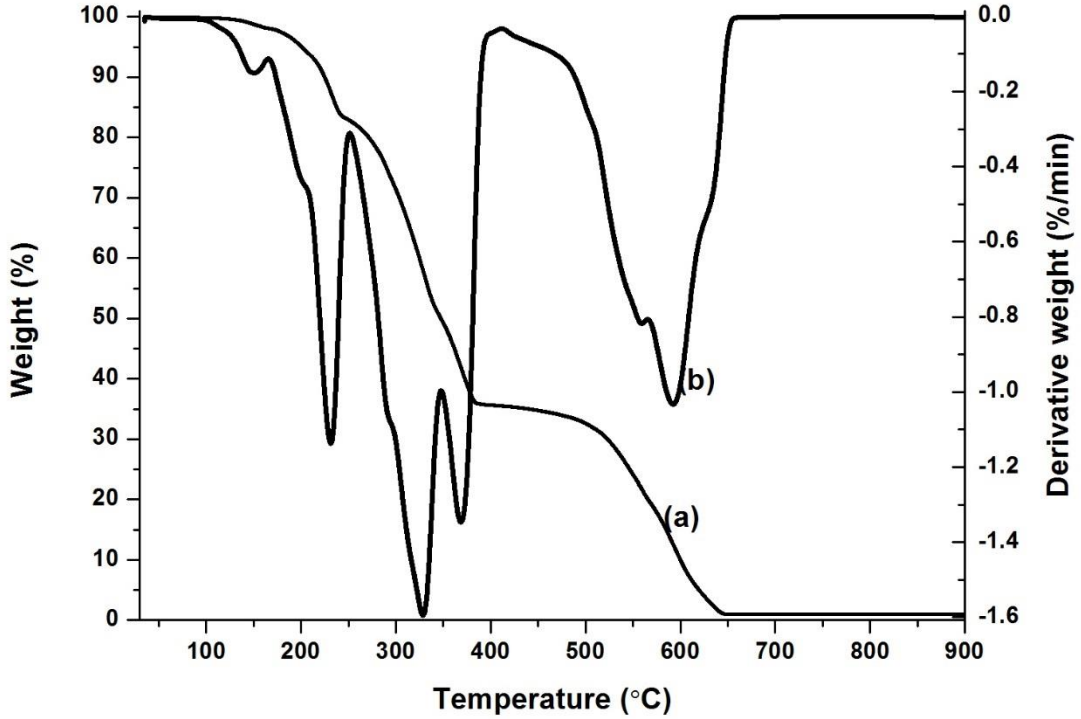


Figure 4-10: The graph for bis(phenylselenolate) iron(II) complex TGA (a), and derivative (b).

The bis(phenylselenolate) iron(II) complex spectra (Figure 4-11) show multiple bands from 3275-655 cm^{-1}. Most of the band are the same as the one for the ligand due to same functional group between them. The spectra exhibit a broad band at 3275 cm^{-1} which can be attributed to O-H stretching frequency. This band can be due to water molecules in the complex. An aromatic band appears at 2980-2899 cm^{-1} and is attributed to C-H stretching frequency. An overtone is exhibited at 1938-1734 cm^{-1} and is due to C=C stretching frequency. A O-H band is exhibited at 1632 cm^{-1} and is attributed to O-H bending. Another band is exhibited at 1562-1455 cm^{-1} and are due to C-C stretching. Furthermore, the C-H bands are exhibited at 1058-983, and 789-650 cm^{-1} which are due to C-H in plane and out of plane band respectively.

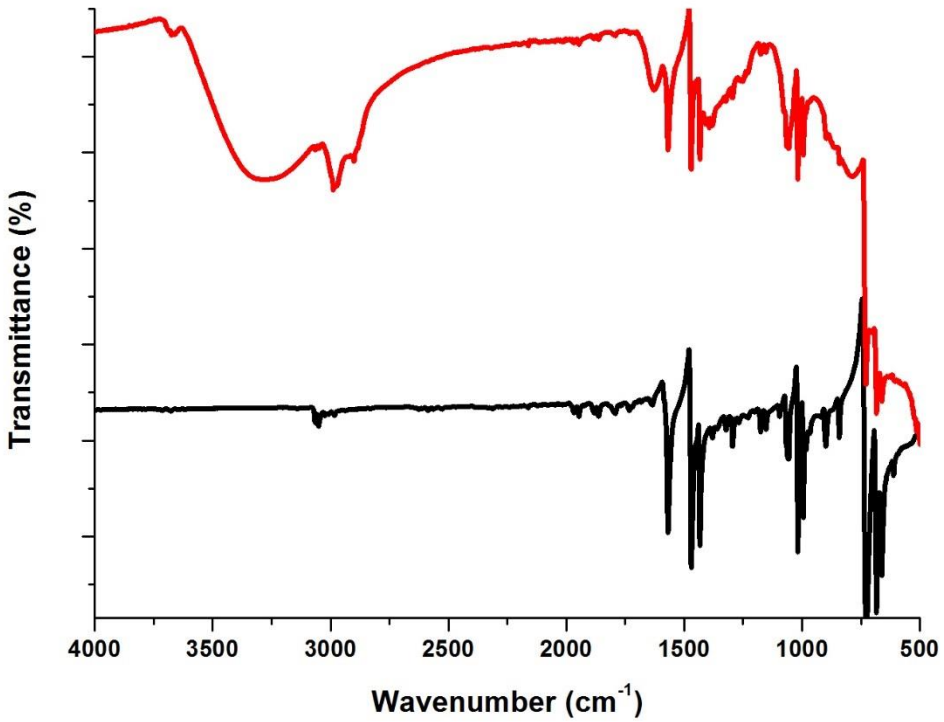


Figure 4-11: The FTIR spectra of diphenyldiselenide (a), and bis(phenylselenolate) iron(II) complex (b).

Figure 4-12 shows the TGA graph of bis(phenylselenolate) iron(II) complex to study its decomposition pattern. The complex undergoes a single step decomposition pathway. The decomposition occurs at approximately 152-289 °C. The final residual mass was significantly lower (5.2 %) than expected mass of the formation of FeSe compound and indicate that the precursor was volatile. The DTG shows the endothermic peak that is associated with decomposition of the ligand moiety.

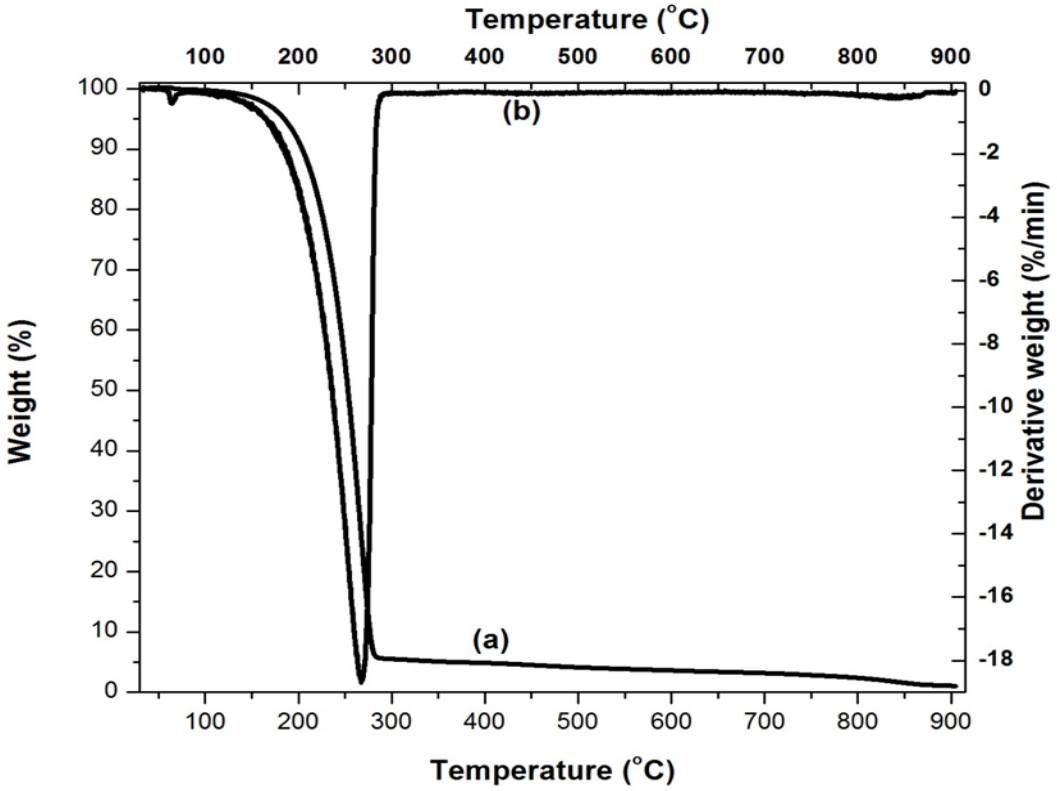


Figure 4-12: The graph (TGA (a) and derivative (b)) of bis(phenylselenolate) iron(II) complex.

4.2 synthesis of metal oxide and metal selenide nanoparticles

Metal chalcogenide nanoparticles also referred to as semiconducting nanoparticles have very controllable size as manipulated through varying synthetic conditions. These generally yields particles with varied sizes and shapes and hence affects their optical properties due to quantum confinement. The control of nucleation and growth of particles are influenced by the types of complex as precursors as well as other conditions such as temperature, time and concentration of starting materials and solvent or capping agents.

4.2.1 **Synthesis of silver oxide nanoparticles**

Figure 4-13 shows the absorption (solid line) and photoluminescence (broken lines) spectra of silver oxide nanoparticles. The UV-Vis of silver oxide nanoparticles shows a band gap energy at 2.265 eV. The band gap is more than their bulk counterparts [193]. This can be attributed to the small size of the prepared silver oxide nanoparticles. The photoluminescence spectra show

emission maxima at 449.16 nm. The emission maximum is red shifted from their absorption spectra of 491.77 nm. The photoluminescence spectra are slightly broad due to agglomeration of the prepared silver oxide nanoparticles.

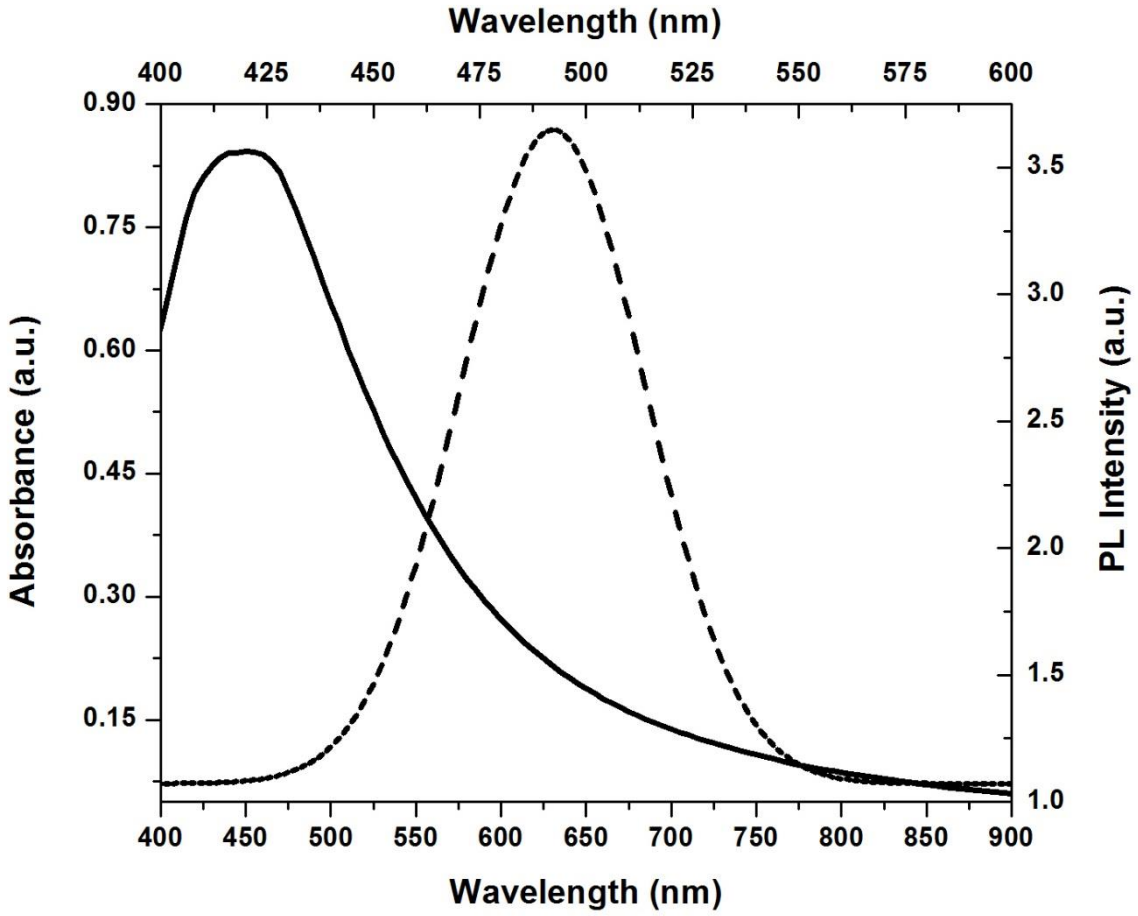


Figure 4-13: The UV-Vis (solid lines)) and PL (doted lines) spectra of silver oxide nanoparticles prepared for 1 hour at 150 °C, and 0.125 g of $Ag_2(U)(NCO)(NO_3)(CH_3OH)$ complex.

Figure 4-14 shows the XRD graph of prepared silver oxide nanoparticles. The XRD shows a mixture of silver and silver oxide diffraction patterns. The first pattern shows four major diffractions at 38.74°, 44.72°, 64.97° and 77.77° which can be indexed to (111), (200), (220), and (311) planes of face-centered cubic silver (JCPDS file no 04-0783). A similar pattern of XRD was reported for metallic silver nanoparticles synthesized by other researchers using biosynthesis [194]. Furthermore, diffraction patterns at 54°, and 68 are indexed to silver oxide nanoparticles of powder diffraction standards (JCPDS no: 12-0793) [195].

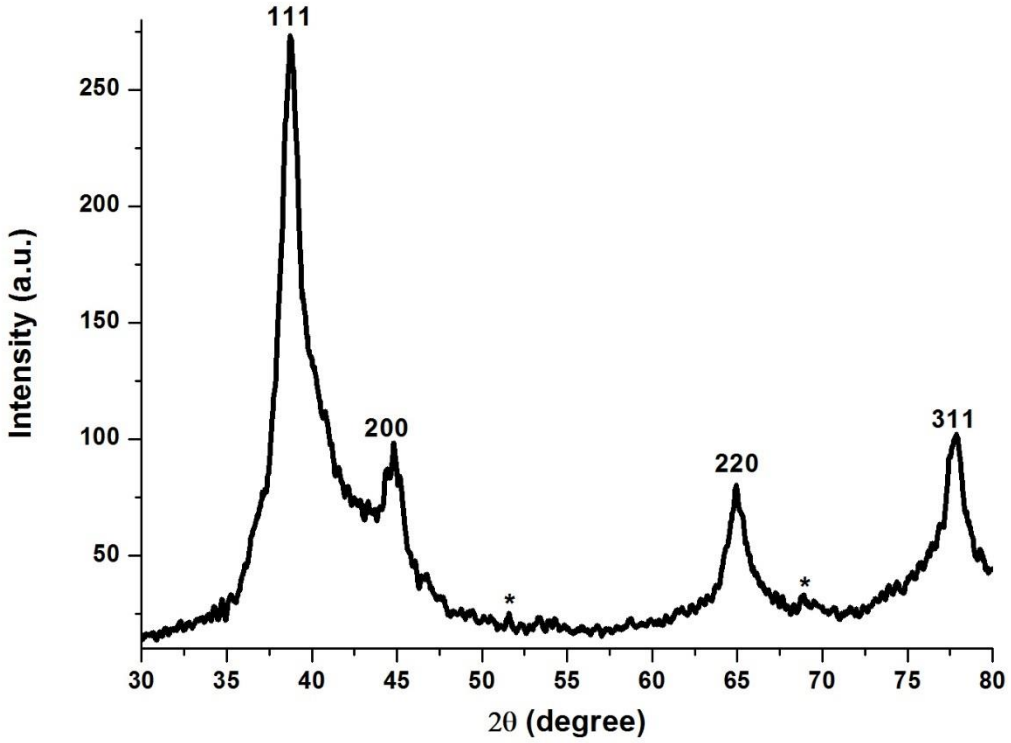


Figure 4-14: The XRD graph of silver oxide nanoparticles prepared for 1 hour at 150 °C, and 0.125 g of a $Ag_2(U)(NCO)(NO_3)(CH_3OH)$ complex.

Figure 4-15 shows the TEM image of the prepared silver oxide nanoparticles. The image shows spherical nanoparticles with smaller, and slightly bigger particles sizes. These particles have a particles size in the range of 2-12 nm. The smaller spheres are more dominant with particles size of 5, and 6 nm. The bigger spheres are formed from the small spheres through Ostwald ripening. Therefore, these nanoparticles are poly-dispersed with two population of spheres. The histogram shows that silver oxide has widely distributed particles size. These particles are mostly dominated with a size the between 5-7 nm.

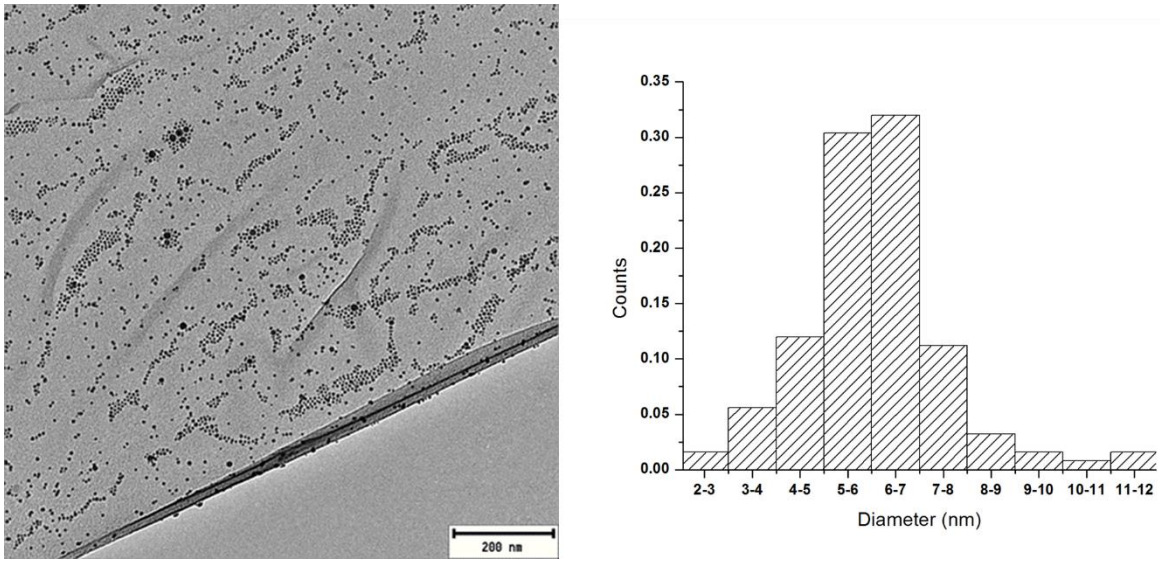


Figure 4-15: The TEM image of silver oxide nanoparticles prepared for 1 hour at 150 °C, and 0.125 g of a $Ag_2(U)(NCO)(NO_3)(CH_3OH)$ complex.

4.2.2 **Synthesis of silver selenide nanoparticles**

Figure 4-16 shows the absorption (solid line) and photoluminescence (red) spectra of silver selenide nanoparticles. The UV-Vis of silver selenide nanoparticles shows a band gap energy at 2.973 eV. This band gap is greater than their bulk counterpart and can be attributed to the small size of the prepared silver selenide nanoparticles[196]. The photoluminescence spectra show emission maxima at 381.92 nm. The emission maximum is red shifted from their absorption spectra of 287.84 nm. The photoluminescence spectra are very broad and are attributed to agglomeration. The broad emission is associated with a mixture of shapes, and various size of particles.

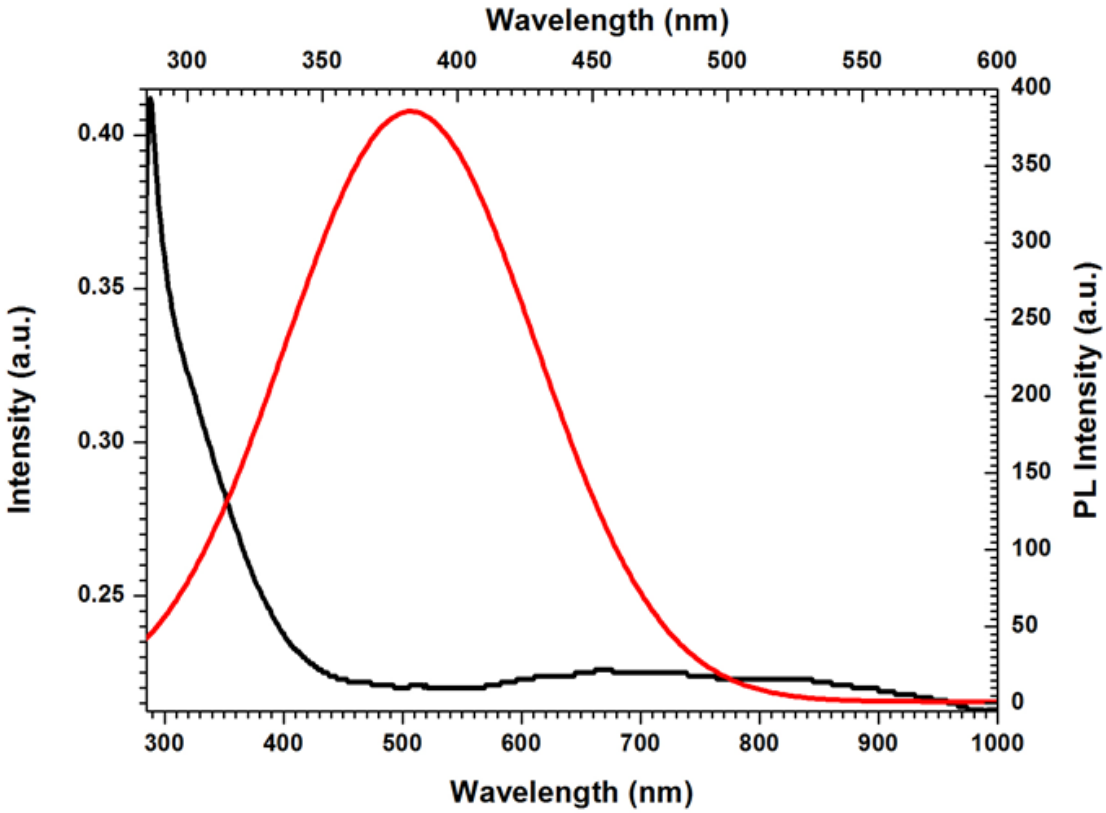


Figure 4-16: The absorption (black) and photoluminescence (red) spectra of silver selenide nanoparticles prepared at 150 °C, for 1 hour, and 0.125 g of $Ag_2(NO_3)(C_6H_5Se)_2$ complex.

Figure 4-17 shows the XRD spectra of silver selenide nanoparticles. The XRD shows diffraction pattern due to the face-centered cubic lattice structure of crystalline silver (JCPDS file no.:04-0783). The diffraction peaks are indexed to (111), (200), (220) and (311) plane. Other peaks at 2 theta of 25 and below can be due to other impurities.

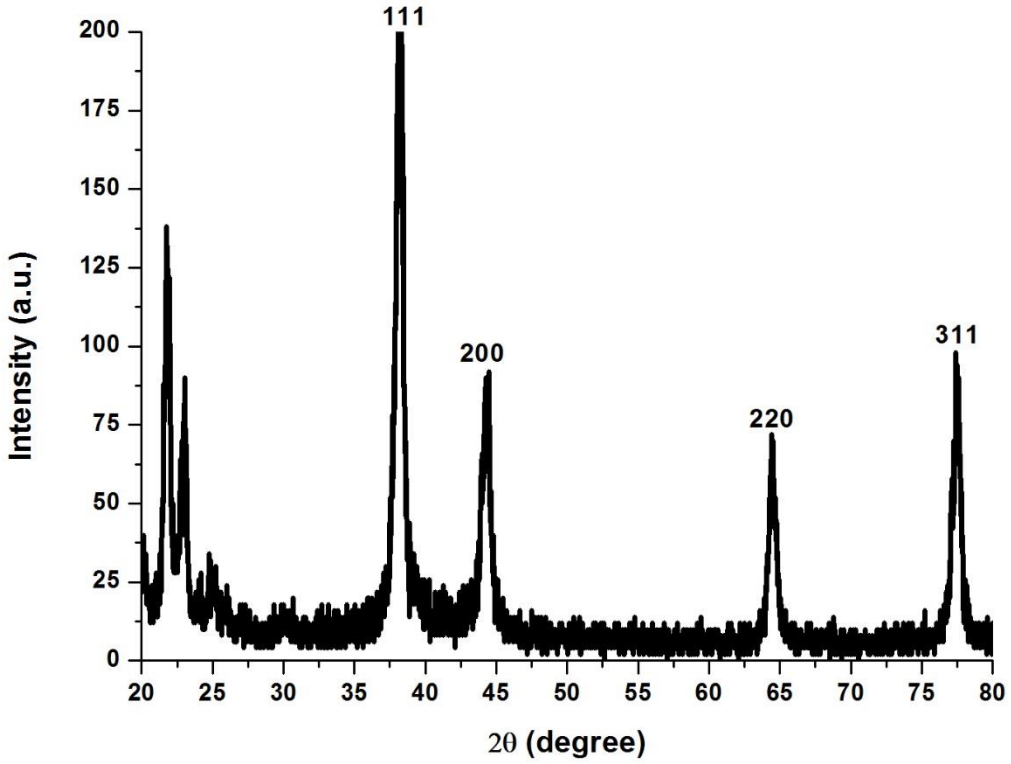


Figure 4-17: The XRD graph of silver selenide nanoparticles prepared at 150 °C, for 1 hour, and 0.125 g of $Ag_2(NO_3)(C_6H_5Se)_2$ complex.

Figure 4-18 shows the TEM image of the prepared silver selenide nanoparticles. The image shows a mixture of sphere, hexagon and rods particles. The spheres have a smaller size, while hexagon and rods are slightly bigger. It appears as if spheres grow to form hexagon and rods. The diameter of the particles is in the range of 3-23 nm. The histogram shows a broad distribution of spherical particles with a major size between 11-13 nm. The broad distribution in the particle size can be due to polydispersity.

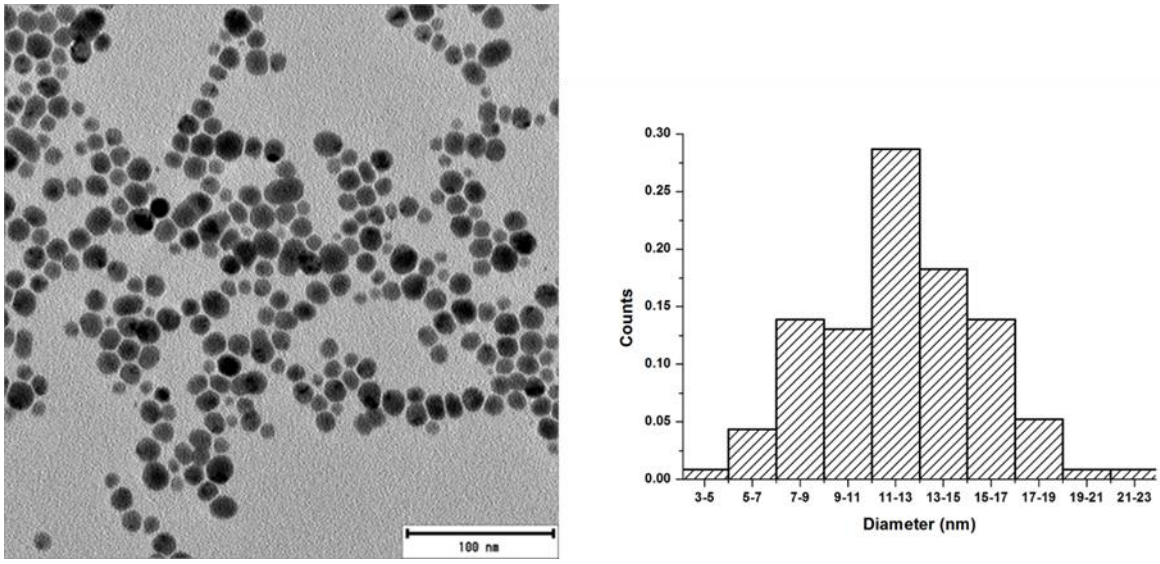


Figure 4-18: The TEM image of silver selenide nanoparticles prepared at 150 °C, for 1 hour, and 0.125 g of $Ag_2(NO_3)(C_6H_5Se)_2$ complex.

4.2.3 **Synthesis of copper oxide nanoparticles**

Figure 4-19 shows the absorption and photoluminescence spectra of $CuAc_2{\cdot}H_2O$ calcined for 1 hour at 400 °C. The absorption spectra are broad and has an optical peak at 476 nm. The broad absorption is associated with polydisperse and coexistence of many phases of copper oxide nanoparticles. The photoluminescence spectra show a broad emission peak at 537 nm. The emission peak is red shifted from its absorption.

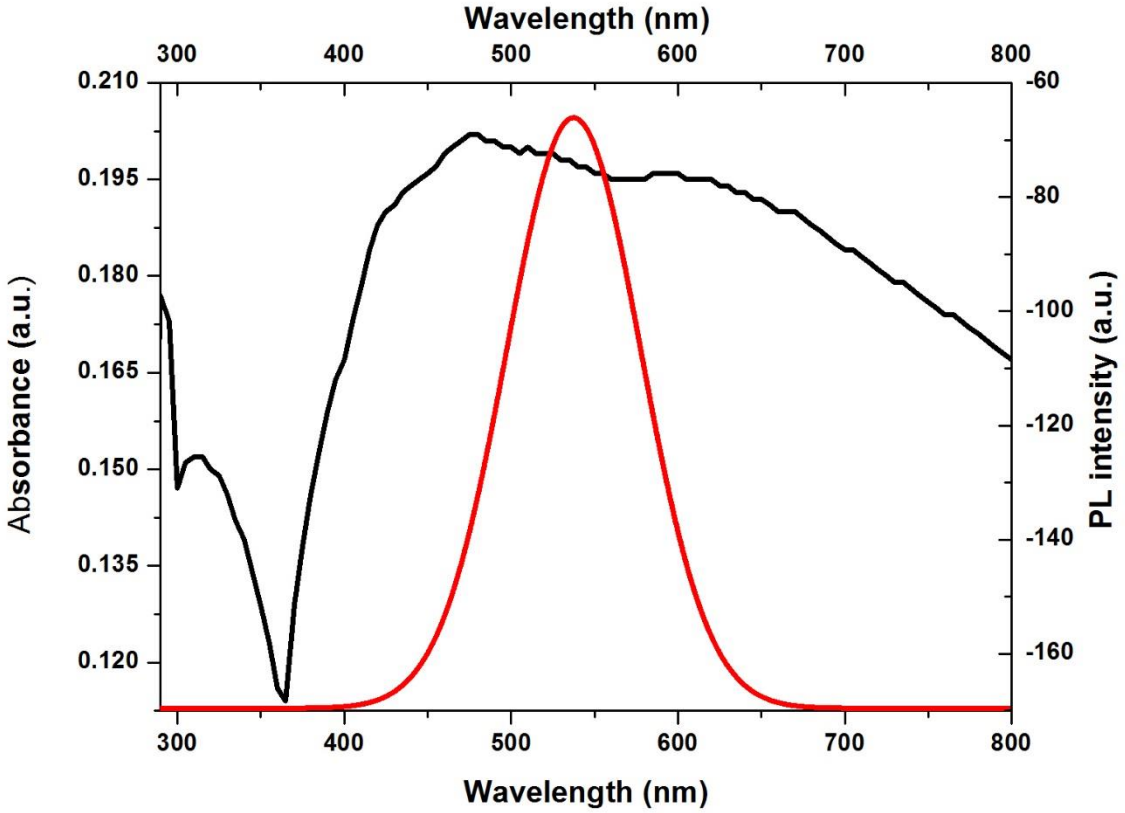


Figure 4-19: The absorption (black) and photoluminescence (red) spectra of $CuAc_2 \cdot H_2O$ calcined for 60 minutes at 400 °C.

Figure 4-20 shows the XRD pattern of $CuAc_2 \cdot H_2O$ calcined for 1 hour at 400 °C. The spectra show a combination of three phases of copper which includes: cuprous oxide (Cu_2O, cuprite), cupric oxide (CuO, tenorite), and copper. The cuprous oxide peaks are consistent with cubic phase Cu_2O (JCPDS card number: 75-1531). However, the cupric oxide peaks are indexed to a monoclinic structure of CuO (JCPDS card number: 80-1916). Furthermore, the XRD pattern for Cu can be indexed to the face-centered cubic Cu (JCPDS card number 85-1326) [197].

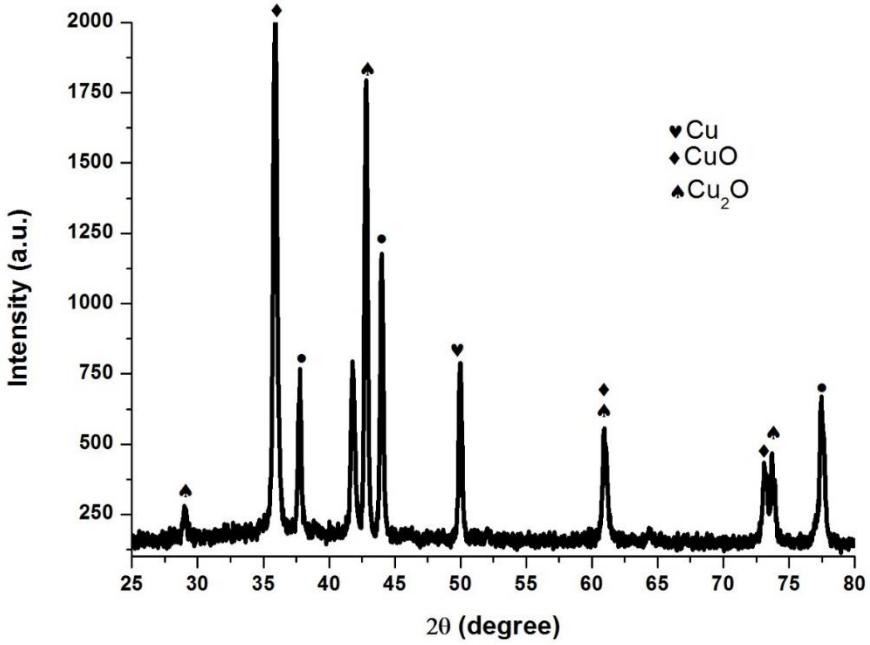


Figure 4-20: The XRD graph of $CuAc_2 \cdot H_2O$ calcined for 60 minutes at 400 °C.

Figure 4-21 shows the TEM image of $CuAc_2 \cdot H_2O$ calcined for 60 minutes at 400 °C to prepare copper oxide nanoparticles. The images show polydisperse spherically shaped nanoparticles with a diameter in the range of 2-9 nm. These nanoparticles are slightly agglomerated, and this is due to the fact that there is no passivating agent used to separate them from each. However, the particles size is very smaller, and good especial that there was no capping molecule. The histogram shows that most particles were in the size range of 4-5 nm.

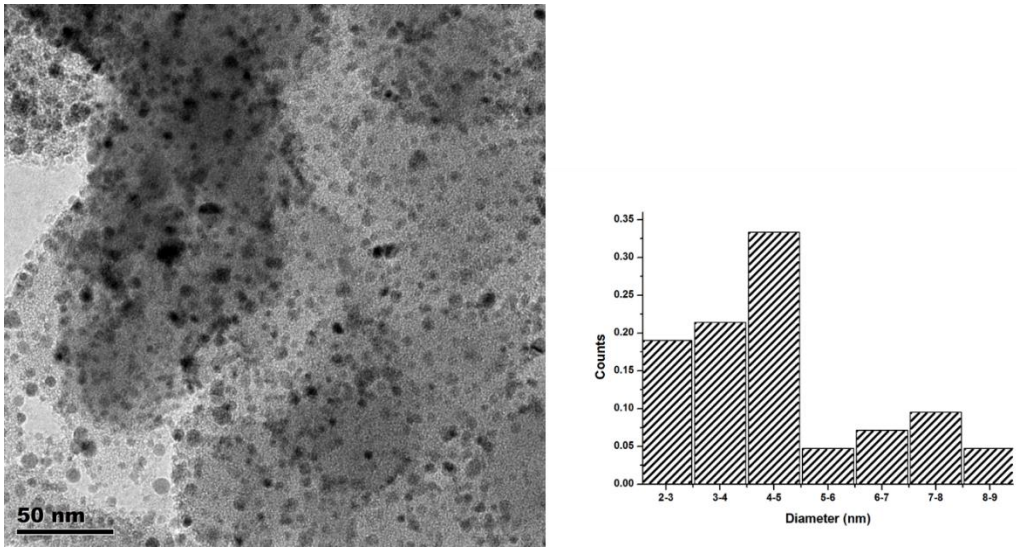


Figure 4-21: The TEM image of $CuAc_2 \cdot H_2O$ calcined for 60 minutes at 400 °C.

4.2.4 **Synthesis of copper selenide nanoparticles**

Figure 4-22 shows the absorption (black) and photoluminescence (red) spectra of copper selenide nanoparticles. The UV-Vis of copper selenide nanoparticles shows a band gap energy of 4 eV [163]. The band gap energy is more than their bulk counterparts. This can be attributed to the small size of the prepared copper selenide nanoparticles. The photoluminescence spectra show emission maxima at 346 nm. The emission maximum is red shifted from their absorption spectra of 274 nm. The photoluminescence shows well distributed and monodispersed copper selenide nanoparticles.

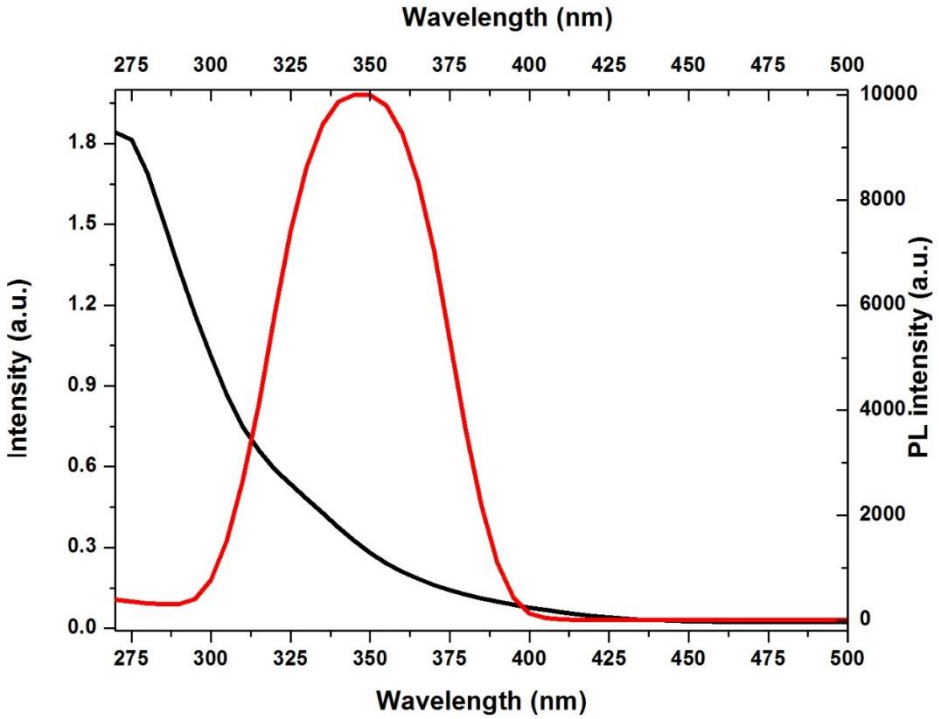


Figure 4-22: The absorption (black), and Photoluminescence (red) spectra of copper selenide nanoparticles prepared by using 0.125 g of the $Cu(Cl)_2(C_6H_5Se)_2$ complex, 5 g HDA at 145 °C for 60 minutes.

Figure 4-23 shows the XRD graph of copper selenide nanoparticles. The XRD pattern shows the co-existence of two-phase α-Cu_2Se and β-Cu_2Se phases. The main diffraction patterns can be indexed to orthorhombic Cu_2Se (JCPDS no: 19-0401). The orthorhombic phase was more dominated. The second phase is indexed to β-Cu_2Se (JCPDS no: 88-2044).[198]

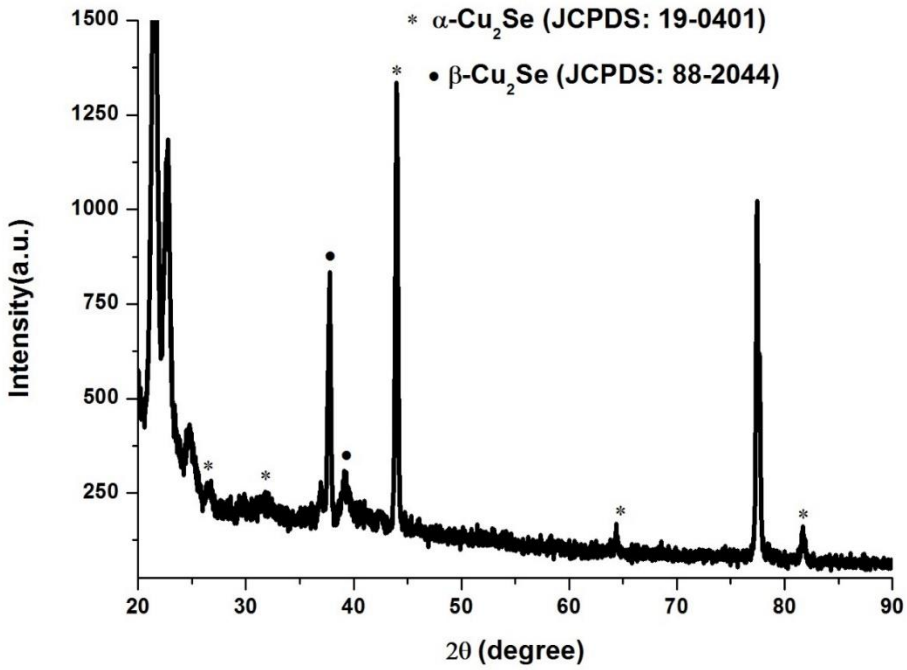


Figure 4-23: The XRD graph of copper selenide nanoparticles prepared by using 0.125 g of the $Cu(Cl)_2(C_6H_5Se)_2$ complex, 5 g HDA at 145 °C for 60 minutes.

Figure 4-24 shows the TEM image of the prepared copper selenide nanoparticles. The image shows spherical nanoparticles with size in the range of 1-5 nm. These sphere have two populations: smaller, and slightly bigger size. In general, the smaller size dissolves and for larger particles that are more stable. The copper selenide nanoparticles are well dispersed without any agglomeration. The histogram shows wide distribution of copper selenide nanoparticles with most particles at 3-3.5 nm.

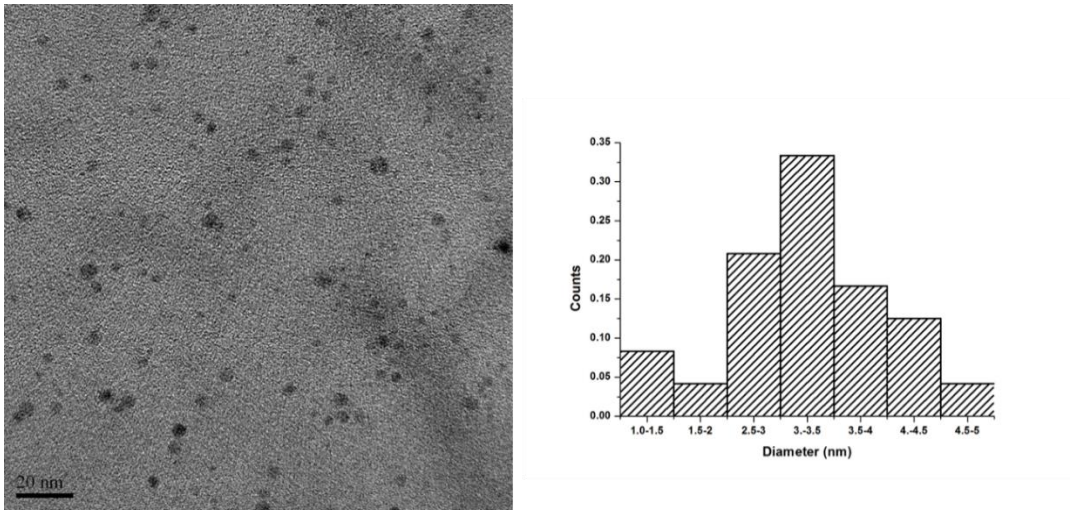


Figure 4-24: TEM image of copper selenide nanoparticles prepared by using 0.125 g of the $Cu(Cl)_2(C_6H_5Se)_2$ complex, 5 g HDA at 145 °C for 60 minutes.

4.2.5 **Synthesis of iron oxide nanoparticles**

Figure 4-25 shows the absorption (black) and photoluminescence (red) spectra of silver oxide nanoparticles. The UV-Vis of iron oxide nanoparticles shows a band gap energy at 2.85 eV. The band gap is blue shifted from their bulk counterparts of 2.0 eV.[199] This can be attributed to the small size of the prepared silver selenide nanoparticles. The photoluminescence spectra show emission maxima at 378.52 nm. The emission maximum is red shifted from their absorption spectra of 361.68 nm. The photoluminescence spectra are broad, widely distributed, and are associated with poly-dispersed iron oxide nanoparticles.

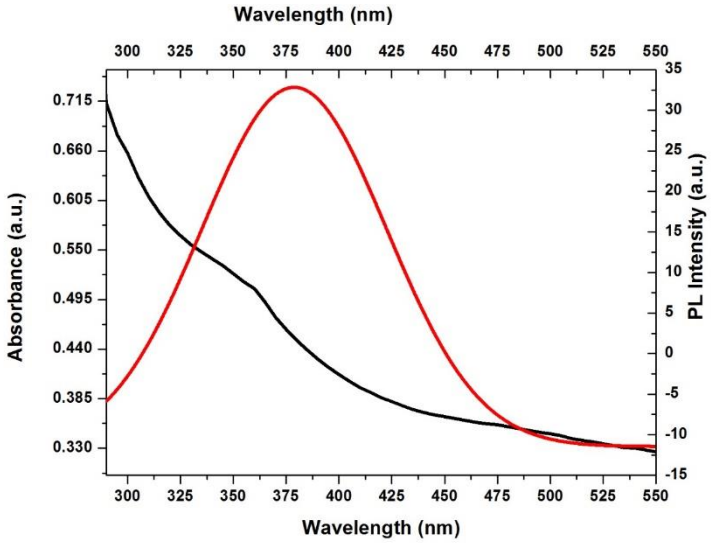


Figure 4-25: The absorption spectra of iron oxide nanoparticles prepared using 0.125 g of $FeCl_2{\cdot}3U{\cdot}4H_2O$ complex at 150 °C, for an hour.

Figure 4-26 shows the XRD graph of iron oxide nanoparticles. The diffraction patterns show broad peaks, and are associated with smaller particles size of iron oxide nanoparticles. The XRD pattern is matched well with the reflection of (220), (311), (400), (422), (511), and (440) planes. These particles are consistent with maghemite (γ-Fe_2O_3) (JCPDS file no. 25-1402).[200] The other peaks are attributed to the sample holder due to the small sample yield.

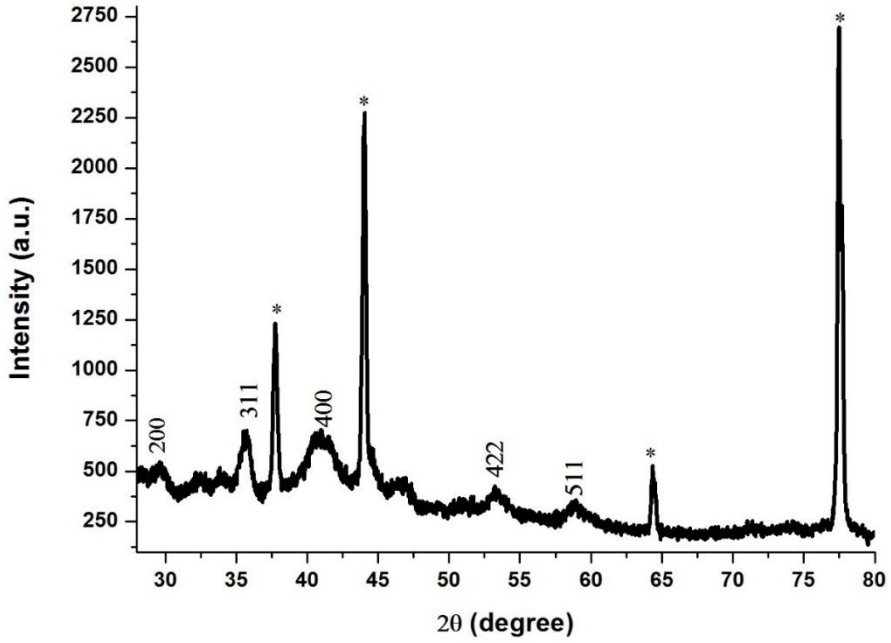


Figure 4-26: The XRD patterns of iron oxide nanoparticles prepared using 0.125 g of $FeCl_2{\cdot}3U{\cdot}4H_2O$ complex at 150 °C, for an hour.

Figure 4-27 shows the TEM image of the prepared iron oxide nanoparticles. The image shows a mixture of rod-like and spherically shaped nanoparticles. However, the two rodes are composed of spherically shaped nanoparticles with size in the range of 6-27 nm. The particles are agglomerated in some areas. The histogram shows that the major size of the particles was between 9-12 nm.

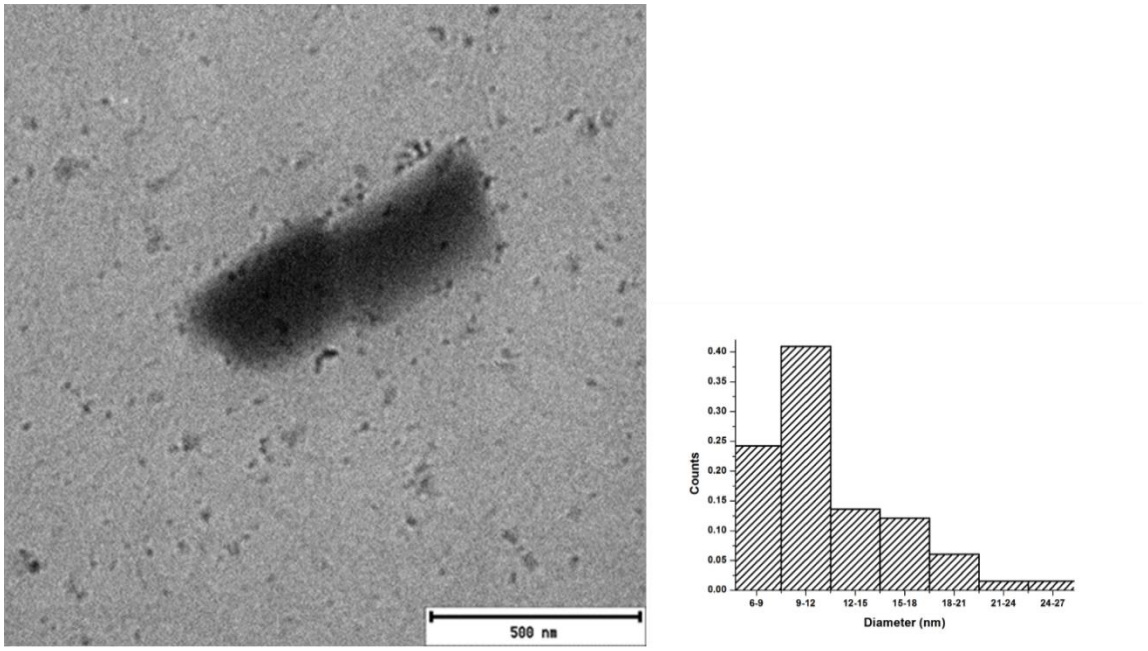


Figure 4-27: The TEM image of iron oxide nanoparticles prepared using 0.125 g of $FeCl_2{\cdot}3U{\cdot}4H_2O$ complex, at 150 °C, for an hour.

4.2.6 **Synthesis of iron selenide nanoparticles**

Figure 4-28 shows the absorption (black) and photoluminescence (red) spectra of iron selenide nanoparticles. The UV-Vis of iron selenide nanoparticles shows a band gap energy at 3.45 eV. This band gap is greater than its bulk of 1.23 eV.[201] This can be attributed to the small size of the prepared iron selenide nanoparticles. The photoluminescence spectra show very broad emission with a maximum at 548 nm. The emission maximum is red shifted from their absorption spectra of 470 nm. The broad emission is attributed to wide size distribution, and a mixture of morphology and phase for the prepared iron selenide nanoparticles.

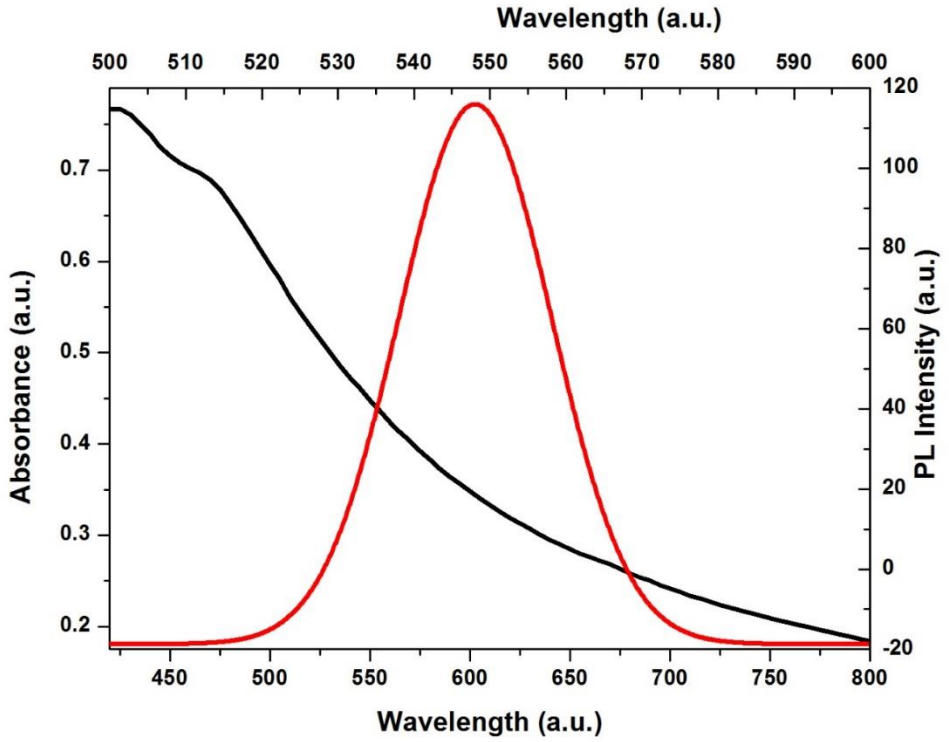


Figure 4-28: The absorption spectra of iron selenide nanoparticles prepared using 1.0 g of bis(phenylselenolate) iron(II) complex, at 150 °C for an hour.

Figure 4-29 shows the XRD graph of iron selenide. The XRD pattern shows two phases of orthorhombic ferroselite ($FeSe_2$). The major phase is indexed to (110), (101), (111), (120), (211), (031), and (122) of orthorhombic ferroselite ($FeSe_2$) (ICDD no: 00-021-0432) and another to orthorhombic ferroselite ($FeSe_2$) (ICDD no:01-074-0247). Akhtar group obtain similar phases when thermal decomposition of bis(tetraisopropyldiselenoimidodiphosphinato) iron(II).[171]

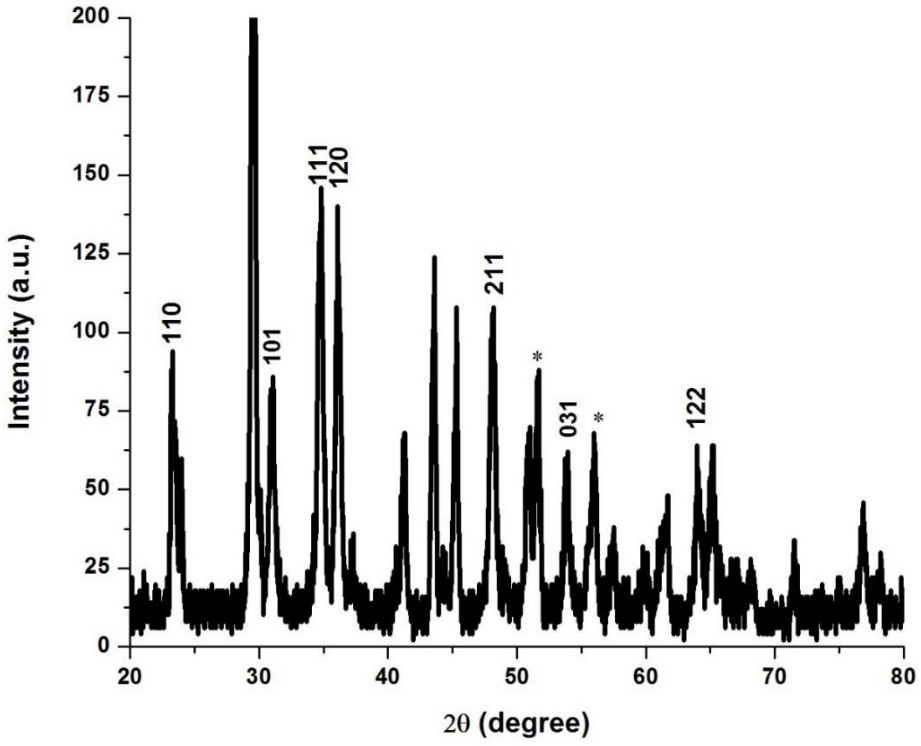


Figure 4-29: The XRD graph of iron selenide nanoparticles prepared using 1.0 g of bis(phenylselenolate) iron(II) complex, at 150 °C for an hour.

Figure 4-30 shows the TEM image of the prepared iron selenide nanoparticles. The image shows irregular shape, and spherical nanoparticles. The spherical particles have size in the range of 8-36 nm. These irregular shape are quite bigger, and agglomerated. The histogram shows that the smaller sphere is dominated with the size between 20-24 nm.

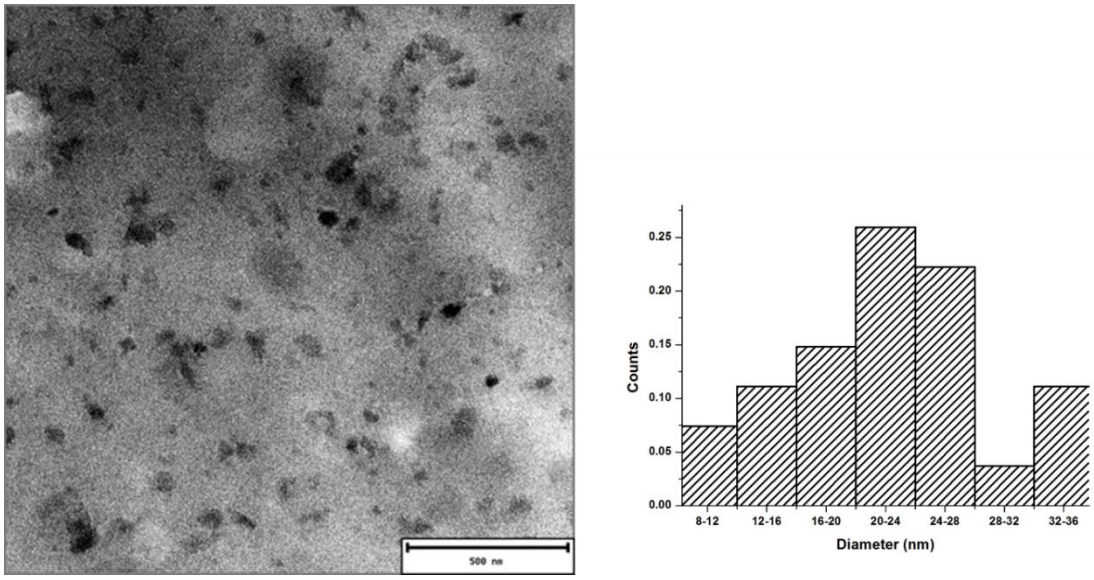


Figure 4-30: The TEM image of iron selenide nanoparticles prepared using 1.0 g bis(phenylselenolate) iron(II) complex, at 150 °C for an hour.

4.3 Fabrication polymethyl methacrylate nanofibers incorporated with metal oxide or metal selenide nanoparticles

The nanofibers are fabricated using poly(methyl methacrylate) solution incorporated with metal oxide and metal selenide nanoparticles. The FTIR spectra for both pure PMMA nanofibers and PMMA incorporated metal chalcogenide nanoparticles are compared. Figures (a) for 31, 34, 37, 37, 40, and 43 represent the FTIR spectra for all PMMA nanofibers without any incorporation. The skeleton structure of poly(methyl methacrylate) (PMMA) spectra is characterized by the following functional groups: C-H (CH_3), C-H (CH_2), C-C, C=O, C-O. The FTIR spectra for poly(methyl methacrylate) nanofibers are summarized in Table 4-2. Table 4-2 shows the frequencies and proposed assignment of functional groups of PMMA nanofibers. The asymmetric and symmetric stretching bands of the C-H (CH_3) groups appear at 2979 and 2900 cm^{-1} respectively. The bands at 1482 and 1456 cm^{-1} can be assigned to deformation mode of the C-H (CH_3) groups. The bands at 1142 and 1059 cm^{-1} are assigned to the twisting mode of the C-H (CH_3). The bands at 1194 cm^{-1} are assigned to the wagging mode of the C-H (CH_3). The band at 1770 cm^{-1} is a characteristic of carbonyl (C=O) stretching. The band at 749 cm^{-1} is assigned to C=O in the plane and out of the plane. The bands at 1242 cm^{-1} are assigned to C-O stretching mode. The band at 3674 cm^{-1} is assigned to O-H group stretching mode due to adsorbed water vapour.

Table 4-2: Summary of wavenumber (cm^{-1}) and functional group of PMMA/Metal Oxide (Selenide) nanofibers.

Observed frequency (cm^{-1})	***Assigned functional group***
3674	*O-H group stretching*
2979	*C-H asym stretching in CH_3*
2900	*C-H asym stretching in CH_3*
1770	*C=O stretching*
1723	*O-H group bending*
1482	*CH_3 deformation*
1456	*CH_3 deformation*
1393	*CH_2 deformation*
1242	*C-O stretching*
1194	*CH3 wagging*
1142	*CH_3 twisting*
1059	*CH_3 twisting*
896	*C-C stretching*
802	*CH_2 rocking*
749	*C=O out of plane bending*

4.3.1 **Synthesis of PMMA-AgO**

Figure 4 31 shows the FTIR spectra for PMMA-AgO nanofibers. The nanofibers for both pure PMMA and PMMA-AgO show similar FTIR spectra. Hence, there are no major changes in the poly(methyl methacrylate) as a result of the incorporation of silver oxide nanoparticles except carbonyl group. There is a decrease in the intensity of carbonyl for PMMA-AgO nanofibers. This can be associated with carbon-oxygen bond being involved in bonding with silver oxide nanoparticles.

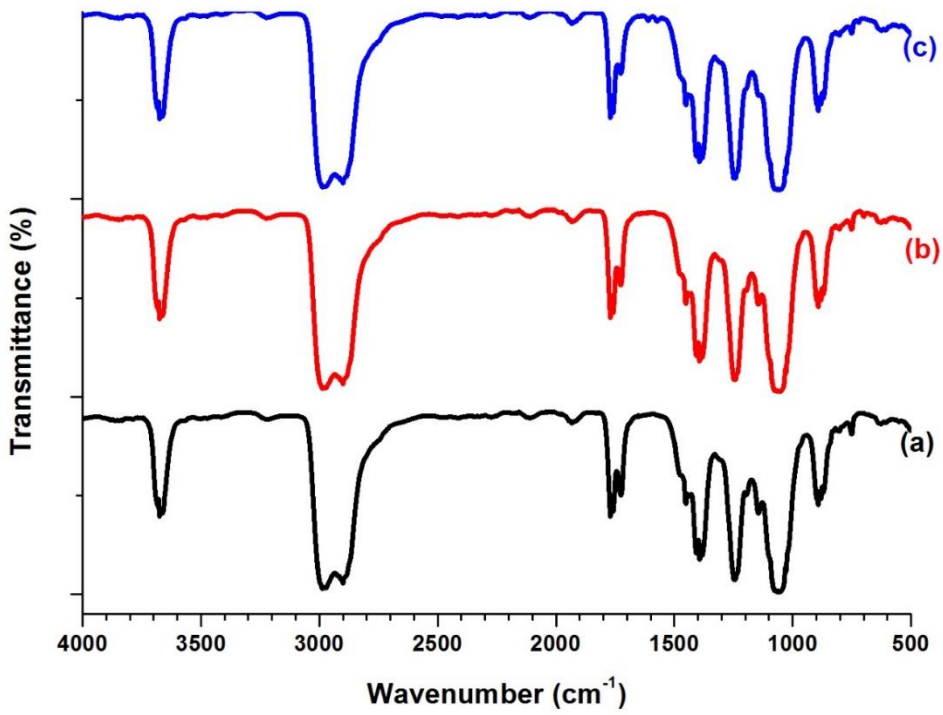


Figure 4-31: The FTIR for PMMA-AgO nanofiber prepared by varying weight of AgO nanoparticles: 0 % (a), 0.1% (b), 2 % (c).

Figure 4-32 shows the thermogravimetric analysis of nanofibers prepared by PMMA incorporated with silver oxide nanoparticles. This complex decomposes into two steps. The first decomposition occurs at about 100 °C for Figure 4-32 (a). This small decomposition can be associated with water molecules. The second decomposition (major) occurs at about 350-410 °C. At this position, the Poly (methyl methacrylate) moiety decomposes to form silver oxide and leave a residue of about 2%. Figure 4-32(b) like Figure 4-32(a) show a two steps decomposition. The first decomposition occurs at between 250 and 310 °C. This decomposition can be associated with decomposition of some polymer compounds. This decomposition is very small, and a second start before is finished. Hence, second decomposition occurs at about 310-420 °C. The decomposition can be associated the rest of poly (methyl methacrylate) moiety. This results in a final residue of 10% of the compound. The residue can be associated with silver oxide nanoparticles. The silver oxide is very stable at this temperature range. Hence, there is slightly increase in thermal stability of the nanofiber composites as the silver nanoparticles is increased.

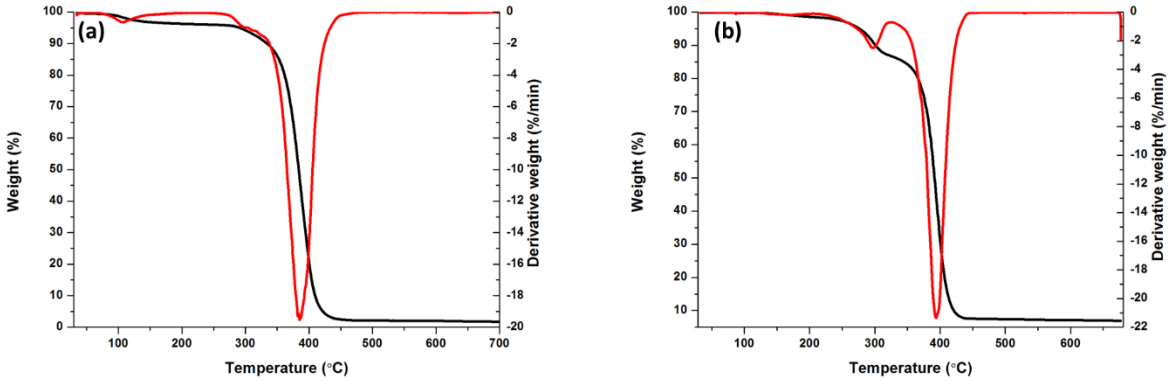


Figure 4-32: The TGA graph of PMMA-AgO nanofibers prepared by varying weight of AgO: 1% (a), and 2% (b).

Figure 4-33 shows the SEM images of nanofibers prepared by poly(methyl methacrylate) incorporated with silver oxide nanoparticles. PMMA nanofiber shows smooth, and uniform nanofibers (Figure 4-33 (a)). The nanofibers size is in the range of 61.77 to 96.21 nm with an average size of 79.24 nm. Figure 4-33 (b) shows the images of PMMA-0.1% AgO nanofiber. The PMMA-0.1% AgO nanofibers have a particle size with an average of 116.15 ± 21.43 nm. The images show nanofibers with some particles on the surface and formation of small beads. Figure 4-33 (c) shows an image of nanofibers with some bigger beads. However, the diameter of the nanofibers has slightly decreased in size. The size of the nanofibers is in the range of 76.71 ± 29.99 nm.

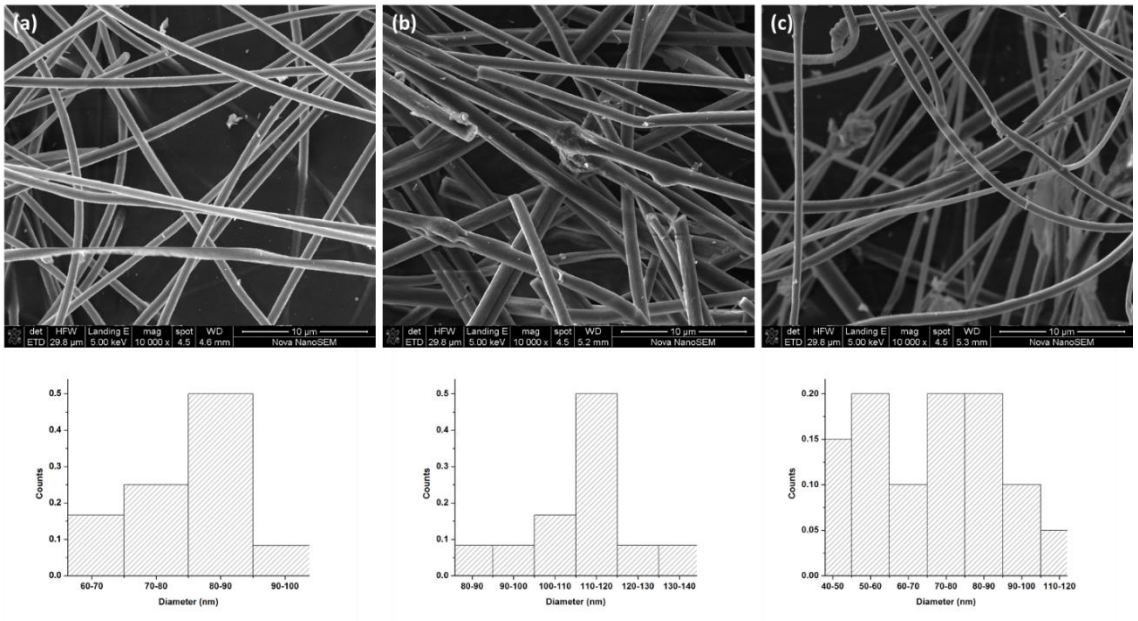


Figure 4-33: The SEM image of PMMA-AgO nanofibers prepared by varying the weight of AgO: 0% (a), 0.1% (b), 2 % (c).

4.3.2 **Synthesis of PMMA-AgSe**

Figure 4-34 shows the FTIR spectra of nanofibers prepared from poly(methyl methacrylate) incorporated with silver selenide nanoparticles. All the spectra for pure PMMA and PMMA-AgSe show comparable results. However, bands associated with a carbonyl (C=O) are less intense in PMMA-AgSe compared to PMMA. This can be due to carbonyl group used in bonding to silver selenide nanoparticles.

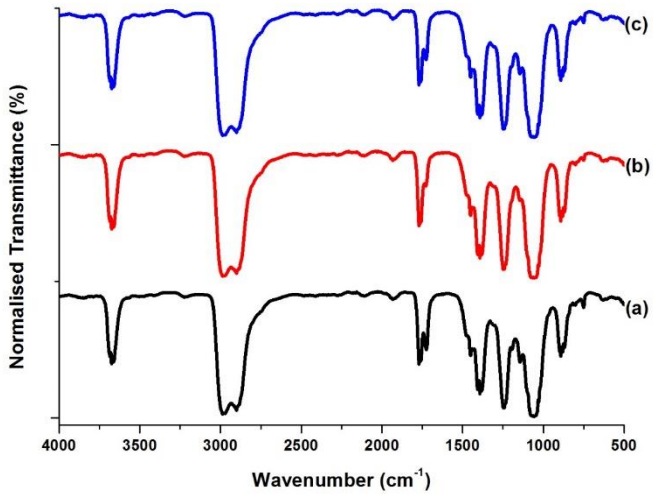


Figure 4-34: The FTIR spectra for PMMA-AgSe prepared by varying the weight of AgSe: 0% (a), 0.1% (b), 2 % (c).

Figure 4-35 (a) shows single step decomposition. The decomposition occurs at about 325 to 410 °C. This decomposition leads to a residue of about 4%. Figure 4-35 (b) shows two decomposition steps. The first small decomposition occurs at about 300 °C. This can be due to decomposition of some parts in the polymer. The second decomposition (major) occurs at about 330 to 425 °C. This can be associated with decomposition of all the organic material in the PMM-AgSe. This leads to a final residue of about 10 %. The residue is stable and can be associated with silver selenide.

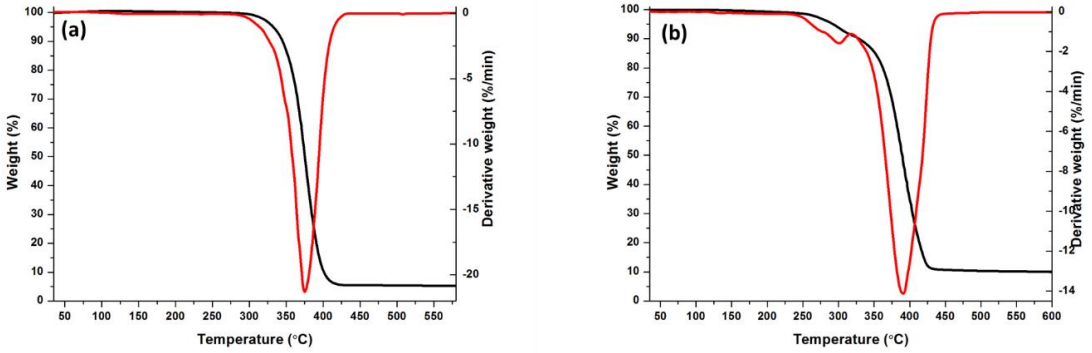


Figure 4-35: The TGA graph of PMMA-AgSe prepared by PMMA loaded with 0.1 % AgSe (a), and 2 % AgSe.

Figure 4-36 (a-c) show SEM images of nanofibers prepared with poly(methyl methacrylate) and poly(methyl methacrylate) incorporated with silver selenide nanoparticles. The SEM images for Figure 4-36 (a) has be outline in Figure 4-33 (a). Figure 4-36 (b) shows the SEM image of PMMA-0.1% AgSe nanofibers. The image shows smooth nanofibers with no beads. However, there are small particles on the surface of nanofibers. The size of nanofibers is widely distributed from 30 to 100 nm. The average size of the nanofibers is 57.51 ± 27.92 nm. The particle is dominated by the size of 30-40 and 60-70 nm. Figure 4-36 (c) shows the SEM images of PMMA-2% AgSe nanofiber. The image shows a nanofiber with small particles on their surface. These nanofibers have uneven surface without any formation of beads. These nanofibers have an average size of 92.06±18.04 nm. The formed nanofibers are well distributed and dominated by 90-100 nm.

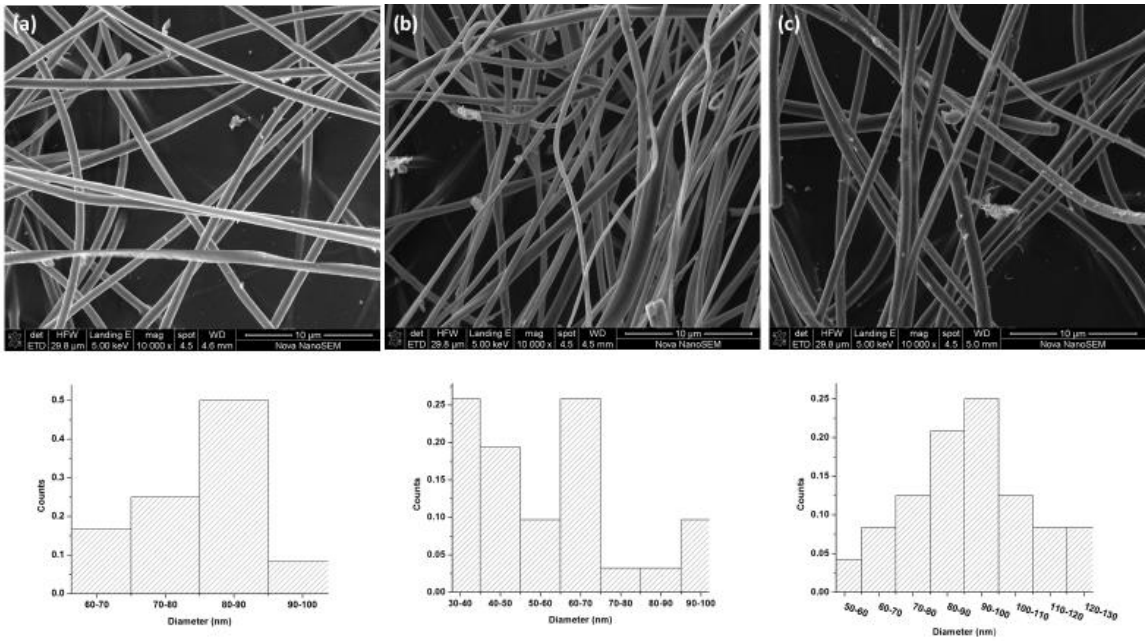


Figure 4-36: The SEM image of PMMA-AgSe prepared by PMMA loaded with varying weight of AgSe: 0% (a), 0.1% (b), 2 % (c).

4.3.3 **Synthesis of PMMA-CuO**

Figure 4-37 represents the FTIR spectra of nanofibers fabricated using poly(methyl methacrylate) incorporated with copper oxide nanoparticles. All the PMMA-CuO spectra are like the one for PMMA nanofibers. However, there is a lightly decrease in intensity of the carbon-oxygen group. This can be due to carbonyl group used in interacting with copper oxide nanoparticles.

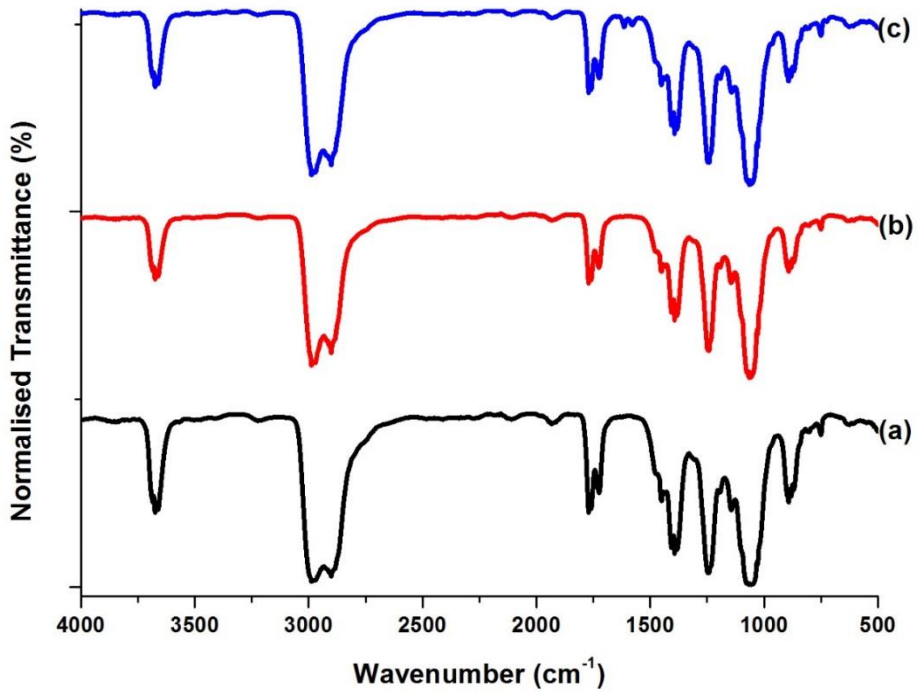


Figure 4-37: The FTIR spectra of PMMA (a), PMMA-0.1% CuO (b), and PMMA-2% CuO (c).

Figure 4-38 (a) shows TGA decomposition pattern of PMMA-CuO. The nanofibers decomposed into two steps. The first decomposition occurs at about 100-120 °C. This decomposition is associated with dehydration or moisture in the nanofibers. The second and major decomposition occurs at 300-400 °C. This decomposition is due to the decomposition of the poly(methyl methacrylate) moiety. This results in a final residue of about 1% and can be associated to copper oxide. Figure 4-38 (b) shows three steps decompositions. The first decomposition occurs at about 90-115 °C. This percentage loss account to 10% and can be associated with water or moisture. The second decomposition step occurs at about 315 to 325 °C. This decomposition is due to dissociation of organic compounds. The third decomposition occurs at about 390-425 °C. This results to a final residue of about 1%, can be due to copper oxide.

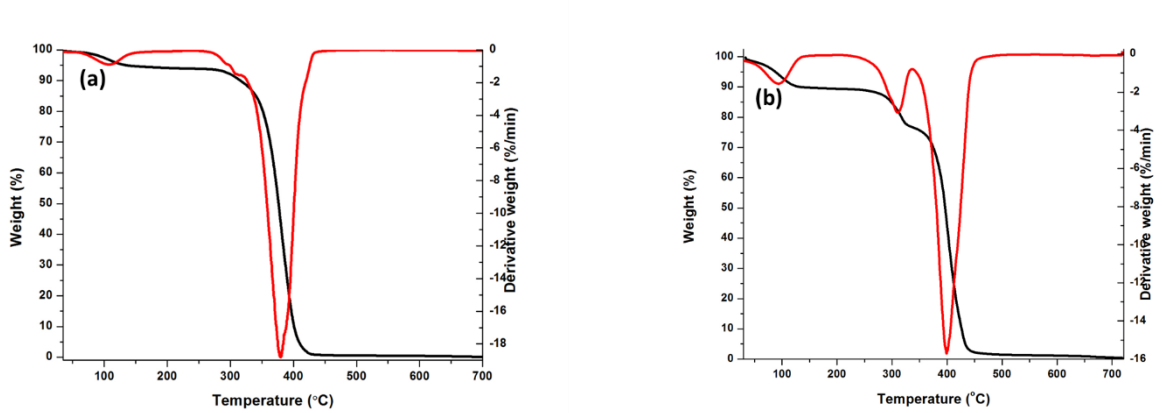


Figure 4-38: The TGA graph of PMMA-CuO prepared by PMMA incorporated with 0.1% CuO (a), and 2% CuO (b).

Figure 4-39 shows the SEM image of nanofiber prepared by PMMA incorporated with copper oxide nanoparticles. Figure 4-39 (a) SEM images has be outline in Figure 4-33 (a). Figure 4-39 (b) shows nanofibers with a smooth surface without any beads. The nanofibers show an average diameter of 76.77 ± 31.29 nm. These nanofibers are widely distributed and dominated with a size of 40-50 nm and 90-100 nm. Figure 4-39 (c) shows smooth surface and bead free nanofibers. The nanofibers have an average diameter of 94.08 ± 9.19 nm. These nanofibers are well distributed and dominated with nanofibers of 95-100 nm in diameter.

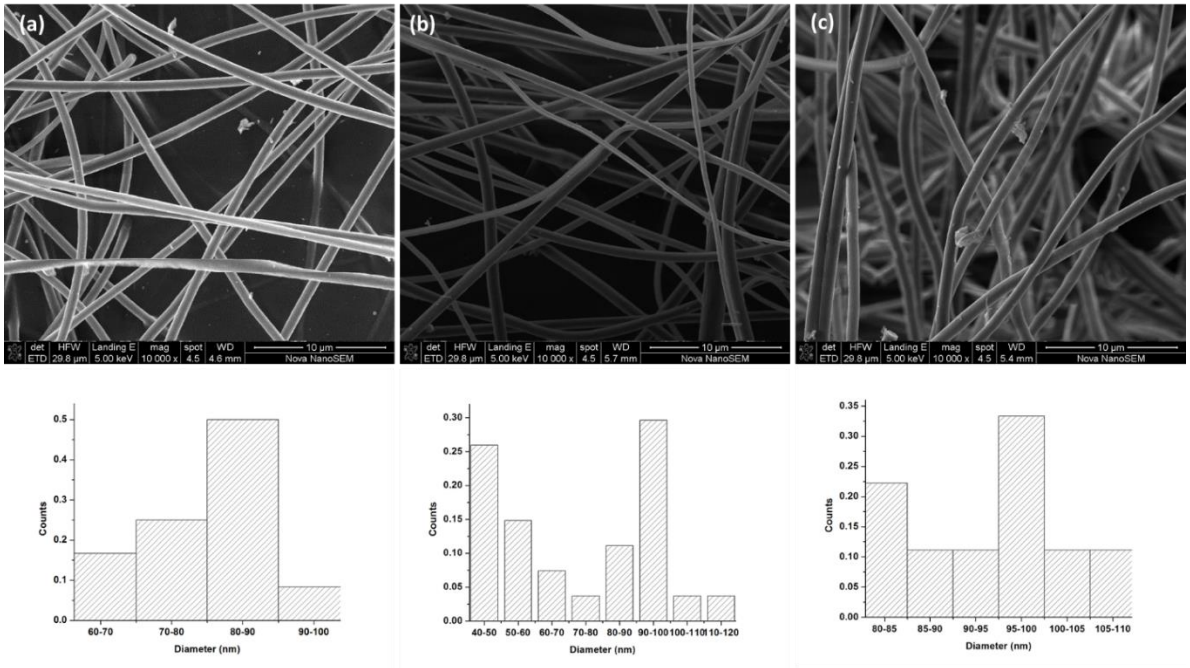


Figure 4-39: The SEM image of PMMA (a), PMMA-CuO (b), and PMMA-0.2% CuO (c).

4.3.4 **Synthesis of PMMA-CuSe**

Figure 4-40 shows the FTIR spectra of nanofiber prepared from poly(methyl methacrylate) solution combined with copper selenide nanoparticles. The FTIR show similar structure as for pure PMMA nanofibers. Nevertheless, the intensity of carbonyl functional groups is slightly less than for PMMA nanofibers. This suggests that carbon-oxygen group are involved in bonding to copper selenide nanoparticles.

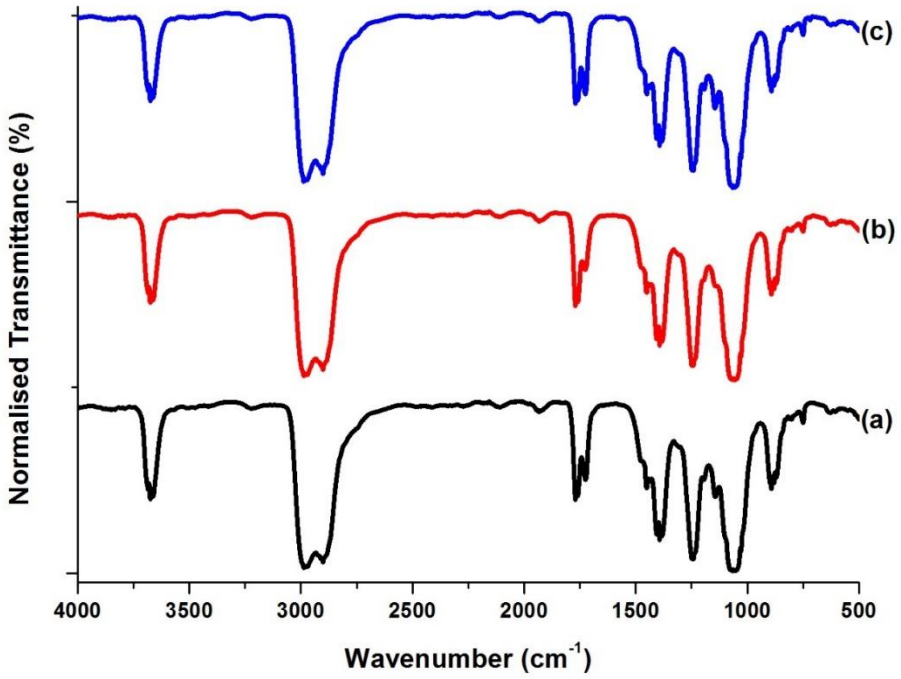


Figure 4-40: The FTIR spectra of PMMA (a), PMMA-0.1% CuSe (b), and PMMA-2% CuSe (c).

Figure 4-41 shows the TGA decomposition pattern of nanofibers papered by poly(methyl methacrylate) incorporated by 0.1% and 2% of copper selenide nanoparticles. In Figure 4-41 (a), the TGA shows a small decomposition at about 90 °C and can be associated with absorbed moisture. This decomposition leads to a percentage weight of about 1%. The next decomposition occurs at about 300 °C and have a small decomposition. The major decomposition occurs about 300-460 °C. This decomposition leads to a loss of some of the less thermal state organic compound from PMMA moiety. The decomposition results in a final residue of about 0.2% and can be associated with copper selenide. Figure 4-41 (b) shows a similar decomposition pathway. The first decomposition occurrs at about 90 °C. This decomposition is accompanied by a mass loss of about by 3% weight, which can be due to

water attached on the surface. The second decomposition occurs at about 300 °C and has mass loss of 10 % weight percent. This is due to decomposition of most organic components. The third decomposition occurs at about 390-420 °C. This composition can be associated with decomposition of poly(methyl methacrylate) moiety. This leads to a final residue of 3% weight and can be due to copper selenide.

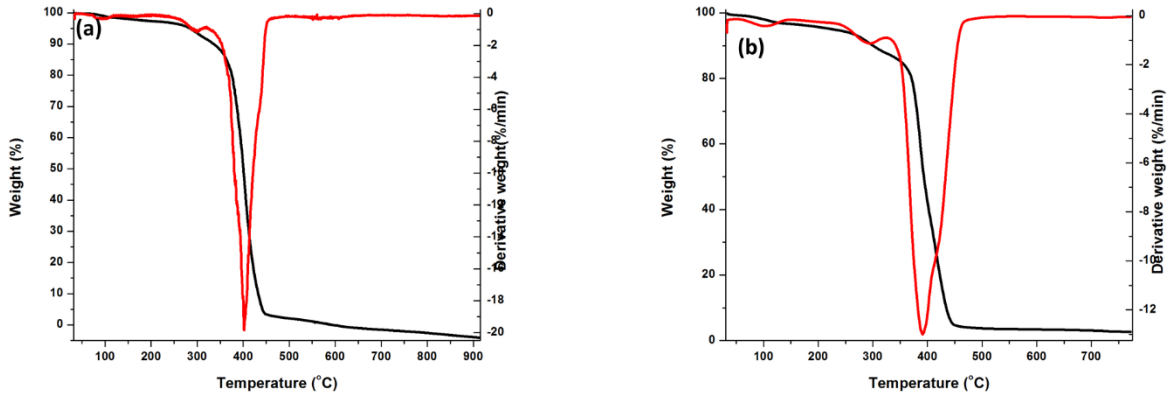


Figure 4-41: The TGA graph of PMMA-0.1% CuSe (a), and PMMA-2% CuSe (a).

Figure 4-42 shows the SEM image of nanofibers prepared by PMMA incorporated with copper selenide nanoparticles. Figure 4-42 (b) shows a smooth surface, coiled and bead free nanofibers. The nanofibers show an average diameter of 47.33 ± 11.45 nm. The nanofibers have a well-distributed histogram with most particles at 45-50 nm. Figure 4-42 (c) show nanofibers with small particles on the surface. The nanofibers have an average diameter of 92.18 ± 25.27 nm. The nanofiber size is widely distributed and dominated by the size of 80-90 nm.

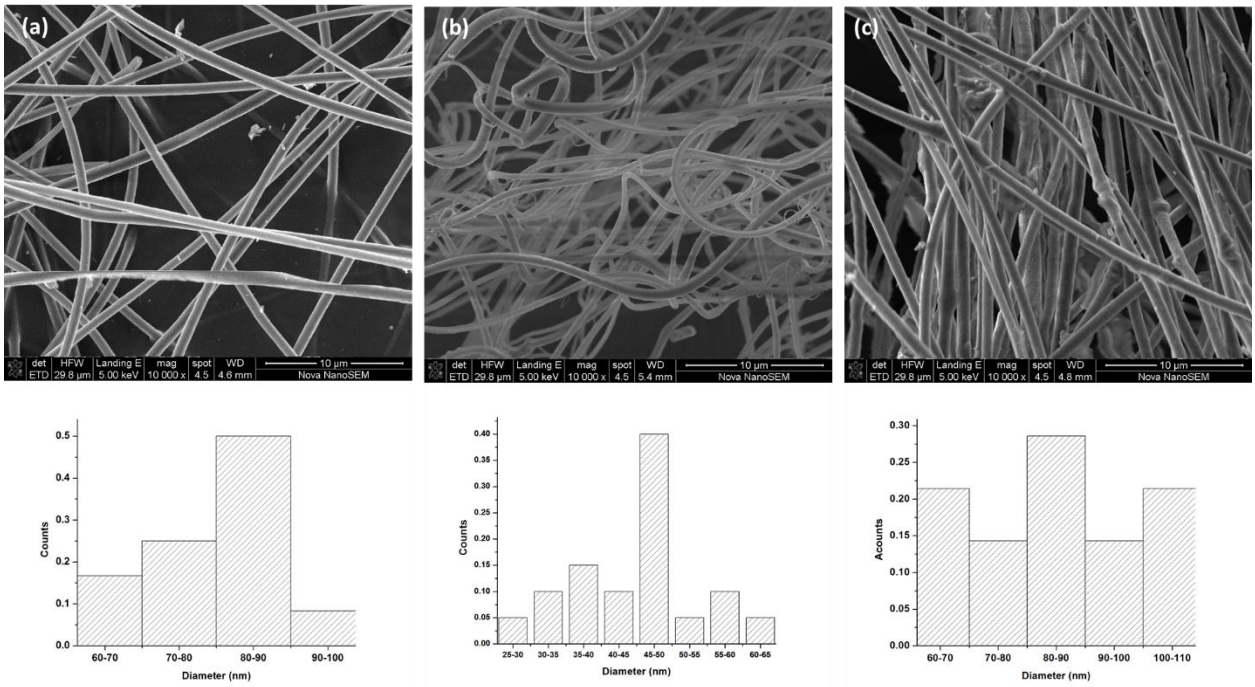


Figure 4-42: The SEM image of PMMA (a), PMMA-CuSe (b), and PMMA-0.2% CuSe (c).

4.3.5 **Synthesis of PMMA-FeO**

Figure 4-43 shows the FTIR spectra for nanofibers prepared using poly(methyl methacrylate) solution impregnated with iron selenide nanoparticles. The three spectra have similar peaks, except for carbonyl peak at 1762 cm^{-1}. This peak is very strong for PMAA nanofibers, whereas it is very weak in PMMA-FeO nanofibers. This confirms that the carbon-oxygen double bond is weakened and is used in bonding with iron oxide nanoparticles.

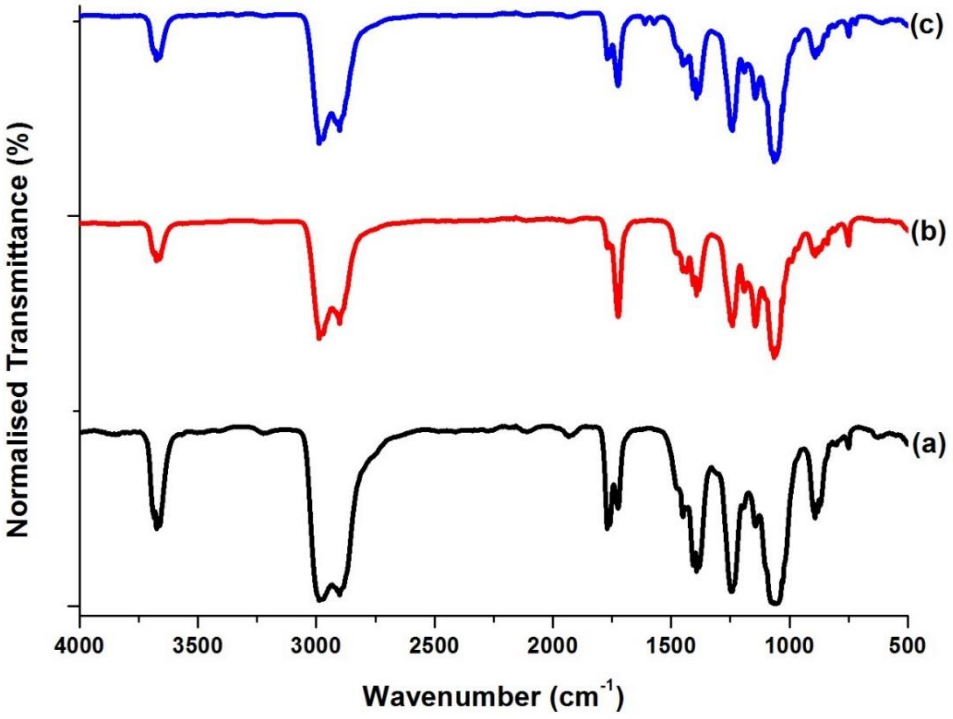


Figure 4-43: The FTIR spectra of PMMA (a), PMMA-0.1% FeO (b), PMMA-2% FeO (c).

Figure 4-44 shows the TGA graph of PMMA-FeO nanofibers prepared by poly(methyl methacrylate) incorporated with iron oxide nanoparticles: 0.1% (a), and 2% (b). The TGA graph show that the nanofibers thermal decomposed into two steps. Figure 4-44 (a) shows small decomposition at about 100 °C. This small decomposition can be associated with removal moisture from the nanofiber. The second decomposition occurs at about 350 °C to 418 °C. This major decomposition can be associated with degradation of poly(methyl methacrylate) moiety. This decomposition leads to a residue of about 0.1% weight. However, in Figure 4-44 (b) similar decomposition pattern has occurred. The first decomposition occurs at about 100 °C. This decomposition is due to moisture or adsorbed water molecules. The second decomposition occurs at about 300 °C to 423 °C. This major decomposition leads to a final residue of 6% weight due to degradation of poly(methyl methacrylate) moiety. The residue can be associated with iron oxide. The derivative show that there can be an overlap of two decompositions at about 300 °C and 400 °C.

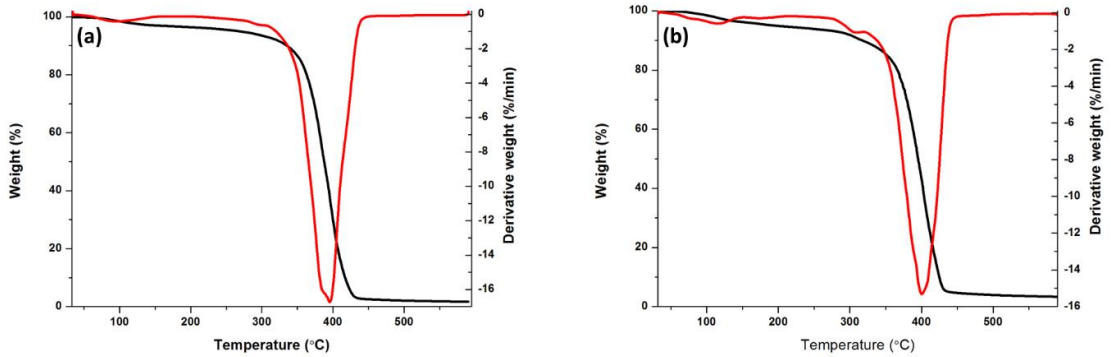


Figure 4-44: The TGA graph of PMMA-0.1% FeO (a), and PMMA-2% FeO (b).

Figure 4-45 (a) shows smoothly surfaced nanofibers without any beads. The nanofibers have an average diameter of 70.36 ± 18.91 nm. The nanofibers sizes are widely distributed and dominated with a size of 50-60 nm. Figure 4-45 (b) show nanofibers with a smooth surface with beads in some areas. The nanofibers have an average diameter of 59.97 ± 15.40 nm. The size diameter of the nanofibers is well distributed and dominated by 50-60 and 60-70 nm.

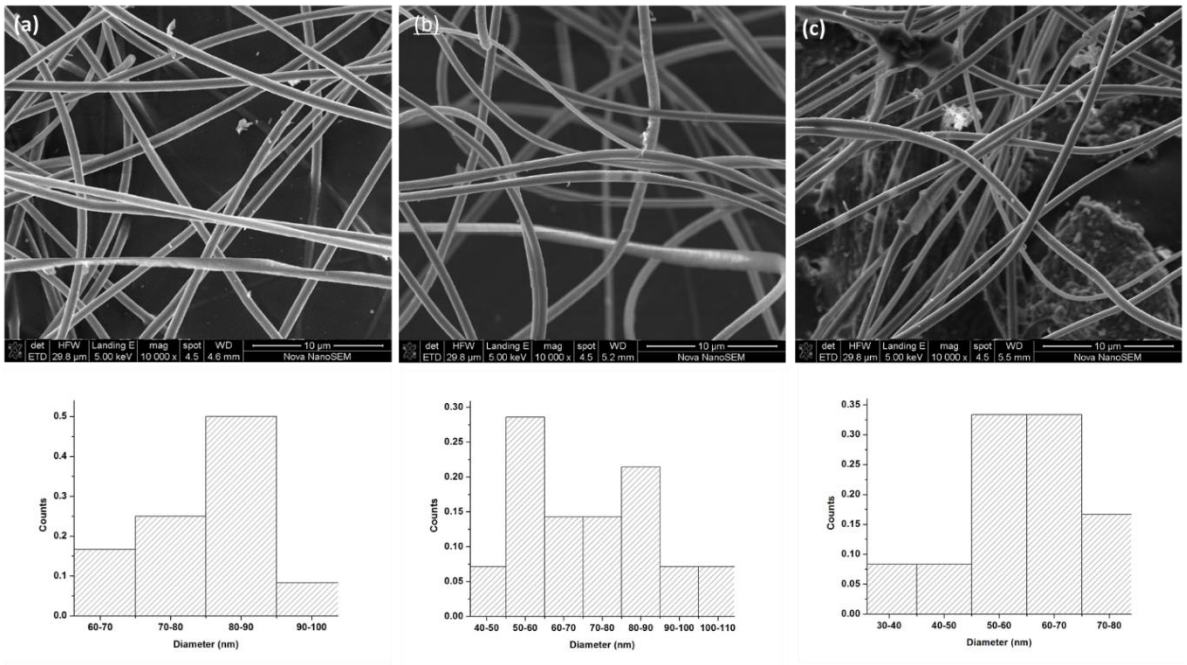


Figure 4-45: The SEM image of PMMA (a), PMMA-FeO (b), and PMMA-0.2% FeO (c).

4.3.6 **Synthesis of PMMA-FeSe polymer fibres**

Figure 4-46 shows the FTIR spectra of nanofibers prepared from poly(methyl methacrylate) solution and incorporated by iron selenide nanoparticles. The PMMA and PMMA-FeSe nanofibers show similar spectra. However, the peaks associated with the carbon-oxygen double bond are weakened for PMMA-FeSe. This is due to the carbonyl group being used in interacting with iron selenide nanoparticles.

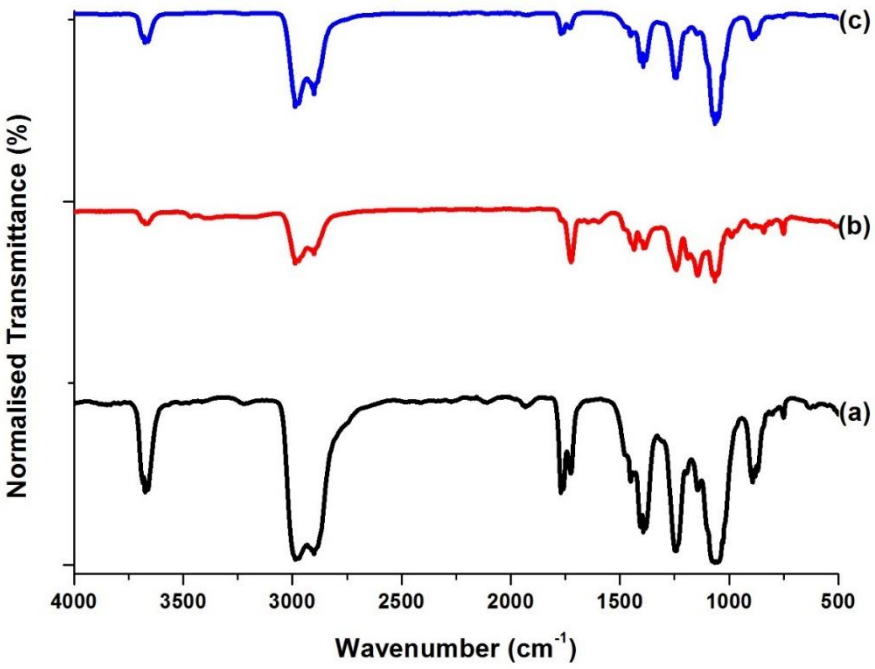


Figure 4-46: The FTIR spectra of PMMA (a), PMMA-0.1% FeSe (b), PMMA-2% FeSe (c).

Figure 4-47 shows the thermogravimetric spectra of nanofibers prepared from poly(methyl methyacrylate) impregnated with iron selenide nanoparticles. Figure 4-47 (a) shows two step decomposition of PMMA-FeSe. The first decomposition occurs at 90-130 °C. This small decomposition can be associated with water molecules on the surface of the nanofibers. The second decomposition occurs at about 277-446 °C. This decomposition can be associated with degradation of polymer moiety. This leads to a residual at about 5 % weight and can be due to iron selenide. Figure 4-47 (b) shows that PMM-FeSe decomposes into two steps. The first small decomposition occurs at about 90-125 °C. This decomposition can be associated with water molecules attached to nanofibers. The second major decomposition occurs at about 290-466 °C. This decomposition results in a residue of about 7 % weight and is due to iron selenide.

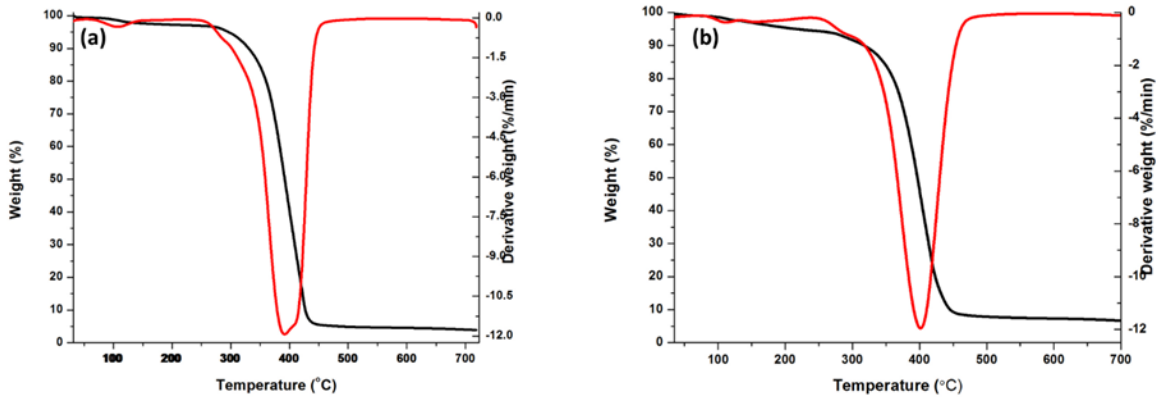


Figure 4-47: The TGA graph of PMMA-FeSe prepared by PMMA incorporated with 0.1%FeSe (a), and 2% FeSe (b).

Figure 4-48 (a) shows nanofibers with a smooth surface with beads. The nanofibers have an average diameter of 86.25 ± 10.03 nm. The nanofibers are widely distributed and dominated with a particle diameter of 75-80 nm. Figure 4-48 (b) shows nanofibers with a rough surface, bigger in size, and without any beads. The nanofibers have an average diameter of 207.30 ± 128.25 nm. However, the nanofibers are well distributed with most particles in the diameter of 100-200 nm.

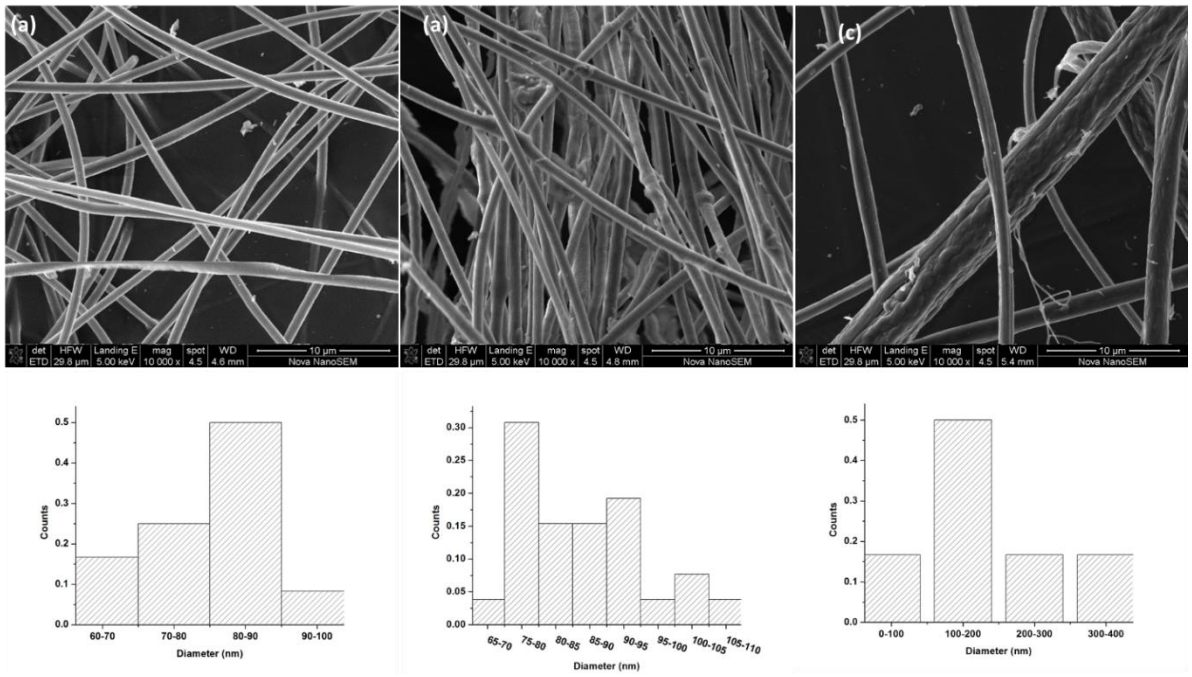


Figure 4-48: The SEM image of PMMA (a), PMMA-FeSe (b), and PMMA-0.2% FeSe (c).

4.4 Applications of the Nanoparticles: Antibacterial and Antifungal Activities

The bacteria activity of nanoparticles (copper selenide, copper oxide, iron selenide, iron oxide, silver selenide, silver oxide) was performed on gram-positive (S. aureus,and E. faecalis) and gram-negative (K. pneumoniae, and P. aeruginosa). The silver oxide nanoparticles show the antibacterial activity in both gram-positive and negative bacteria. The silver oxide shows the highest activity on the gram-positive even at lowest concentration (0.39 mg/mL). However, K.pneumonia, and P. aeruginosa have the MIC of 3.125, and 1.56 mg/mL respectively. The silver selenide shows lowest activity in both gram-positive and negative bacteria. The silver selenide shows an MIC of 25 mg/mL for three bacteria K. pneumoniae, P. aeruginosa, S. aureus, and of 6.25 mg/mL for E. faecalis. The copper oxide shows more activity on the gram positive, and relatively less activity on the gram-negative bacteria. The copper oxide show an MIC of 0.39, 6.25, 6.25, and 25 mg/mL for S.aureus, E. faecallis, K.pneumonia, and, P.aeruginosa respectively. The copper selenide shows the best activity for both gam-positive and negative bacteria. The copper selenide has an MIC of 0.39, 1.56, 3.125, and 3.125 mg/mL respectively. The iron oxide shows the best activity for gram-positive, less activity for the gram-negative bacteria. The MIC for both gram-positive and negative are 0.39 and 25 mg/mL respectively. The iron selenide shows the best activity on the gram-positive, and poor activity on the gram-negative bacteria. The MIC for S.aureus, E. faecalis, K.pneumonia, and P.aerugonosa were 0.39, 0.78, 50, 0 mg/mL respectively.

The antifungal activity of nanoparticles (copper oxide, copper selenide, solver oxide, silver selenide, iron oxide, and iron selenide) are studied against yeasts (C.neoformans, and C.albicans). All the nanoparticles show the highest activity to both yeasts as outlined in Table 4-3. All the nanoparticles show the lowest MIC (0.39 mg/mL) against C. neoformans. However, silver selenide and copper oxide performs worst against C.albicans with an MIC of 3.125 mg/mL. On the contrary the copper selenide, iron selenide, and iron oxide show the smallest MIC against C.albicans.

Table 4-3: MIC (mg/mL) of metal oxide and metal selenide nanoparticles against various microorganisms

Culture	Silver Selenide	Copper Selenide	Iron Selenide	Silver Oxide	Iron Oxide	Copper Oxide
S.aureus	6.25	0.39	0.39	0.39	0.39	0.39
E.faecallis	25	1.56	0.78	0.39	0.39	6.25
K.pneumonia	25	3.125	50	3.125	25	6.25
P.aeruginosa	25	3.125	0	1.56	25	25
C.neoformans	0.39	0.39	0.39	0.39	0.39	0.39
C.albicans	3.125	0.39	0.39	0.78	0.39	3.125

Chapter five

5 Conclusions and Recommendations

5.1 Conclusion

The nanofibers are prepared with poly(methyl methacrylate) mixed with metal oxide and metal selenide nanoparticles. The poly(methyl methacrylate) coordinate to the metal oxide and metal selenide though oxygen atom of the carbonyl group. Hence, the C=O show a weak peak at 1723 cm^{-1} for nanofibers prepared by PMMA incorporating with nanoparticles. The thermal stability of PMMA is improved by incorporating metal oxide and metal selenide nanoparticles. Themogravimetric analysis show that the major decomposition of PMMA-MO/MSe nanofibers occurs at 350-410 °C. The SEM images of nanofibers prepared show that pure PMMA has smooth, uniform without any beads. The SEM image of nanofibers prepared with PMMA-MSe/MO show nanofibers with uneven surface and small beads. The surface becomes more rough and large beads are observed as the percentage of nanoparticles is increased. However, the diameter of the nanofibers is decreased as the percentage nanoparticles is increased. The PMMA-MSe/MO nanofibers have a diameter in the range of 30-200 nm.

The complexes are prepared by using oxygen (urea) and selenium (diphenyldiselenide) ligands with metals salts (iron, copper, and silver). The TGA show that the complexes are very stable. These complexes decompose and form metal oxide/oxide and metal. The nanoparticles of metal oxide and metal selenide are prepared by thermal decomposition of the complexes. The optical properties show that all the formed nanoparticles have smaller size. The XRD show the crystallinity and phases of nanoparticles. Most oxide show a mixture of metal oxide and metal nanomaterials. All the spectra are well indexed. The TEM image show rod, and many spherical nanoparticles with the size in the range of 1-36 nm. The formed nanoparticles show the best activity in gram positive than gram negative bacteria. The silver oxide shows the best activity to both bacteria. However, the gram negative was relatively less active to other metal oxide and metal selenide nanoparticles. All the nanofibers show the best antifungal properties even at lowest concentrations.

5.2 Recommendations

Further research needs to be done on the biocidal effect of these nanofibers. These nanofibers are only soluble to solvent such as toluene, acetone, and some alcohols that have antibacterial properties. Hence the antibacterial text could not be done in solution. Other nanofibers can be prepared using water soluble polymer so that their biocidal properties can be easily tested. The toxicity of the nanofibers and nanoparticles need to tested before these materials can be applied in biological related fields.

Chapter six

6 References

1. Ghosh SK. Kubo Gap as a Factor Governing the Emergence of New Physicochemical Characteristics of the Small Metallic Particulates. *Sci Technol*. 2011;7:114-121.

2. Smith AM, Nie S. Semiconductor Nanocrystals: Structure, Properties, and Band Gap Engineering. *Acc Chem Res*. 2010;43(2):190–200. doi:10.1021/ar9001069.Semiconductor

3. Faraday M. The Bakerian lecture: experimental relations of gold (and other metals) to light. *Phil Trans R Soc*. 1857;147(0):145-181. http://rstl.royalsocietypublishing.org/cgi/doi/10.1098/rstl.1857.0011%5Cnfile:///Files/DD/DD08DF14-D0BF-4F2E-9D31-5C6438CC1559.pdf%5Cnpapers3://publication/doi/10.1098/rstl.1857.0011.

4. Rossetti R, Ellison JL, Gibson JM, Brus LE. Size effects in the excited electronic states of small colloidal CdS crystallites. *J Chem Phys*. 1984;80(9):4464. doi:10.1063/1.447228

5. Alonso a, Macanás J, Davies GL, Gun YK. Environmentally-safe polymer-metal nanocomposites with most favorable distribution of catalytically active and biocide nanoparticles. *Adv Nanocomposite Technol*. 2011. http://www.intechopen.com/books/advances-in-nanocomposite-technology/environmentally-safe-catalytically-active-and-biocide-polymer-metal-nanocomposites-with- enhanced-str%5CnInTech.

6. Rao CNR, Kulkarni GU, Thomas PJ, Edwards PP. Metal nanoparticles and their assemblies. *Chem Soc Rev*. 2000;29(1):27-35. doi:10.1039/a904518j

7. Bawendi MG, Steigerwald ML, Brus LE. The Quantum Mechanics Of Larger Semiconductor Clusters (. *Annu Rev Phys Chem*. 1990;41(4):477-496. doi:10.1146/annurev.physchem.41.1.477

8. Min Y, Akbulut M, Kristiansen K, Golan Y, Israelachvili J. The role of interparticle and external forces in nanoparticle assembly. *Nat Mater*. 2008;7:1-12.

papers2://publication/uuid/839B27D5-CD3A-4B35-825A-17FF2D8CA96A.

9. Domènech B, Bastos-Arrieta J, Alonso A, Macanás J, Muñoz M, Muraviev DN. Bifunctional Polymer-Metal Nanocomposite Ion Exchange Materials. In: *Ion Exchange Technologies*. ; 2012:35-72.

10. Doyle TJ, Zheng W, Cerhan JR, et al. The association of drinking water source and chlorination by- products with cancer incidence among postmenopausal women in Iowa: a prospective cohort study. *AmJPublic Heal*. 1997;87(7):1168-1176.

11. Ren G, Hu D, Cheng EWC, Vargas-reus MA, Reip P, Allaker RP. Characterisation of copper oxide nanoparticles for antimicrobial applications. *Int J Antimicrob Agents*. 2009;33:587-590. doi:10.1016/j.ijantimicag.2008.12.004

12. Richards HL, Baker PGL, Iwuoha E. Metal Nanoparticle Modified Polysulfone Membranes for Use in Wastewater Treatment: A Critical Review. *J Surf Eng Mater Adv Technol*. 2012;02(03):183-193. doi:10.4236/jsemat.2012.223029

13. Ochoa NA, Masuelli M, Marchese J. Effect of hydrophilicity on fouling of an emulsified oil wastewater with PVDF/PMMA membranes. *J Memb Sci*. 2003;226(1-2):203-211. doi:10.1016/j.memsci.2003.09.004

14. Ludvik J, Nygard B. Electrochemistry and metal complex formation of organic diselenides. *ELSEVIER J Electroanal Chem*. 1997;423:1-11.

15. Smyth WF, Jan MR. A study of the differential pulse voltammetric behaviour of organic and inorganic selenium compounds and its analytical applications. *Fresenius J Anal Chem*. 1993;346(10-11):947-951. doi:10.1007/BF00322756

16. Pesarico AP, Sartori G, dos Santos CFA, et al. 2,2'-Dithienyl diselenide pro-oxidant activity accounts for antibacterial and antifungal activities. *Microbiol Res*. 2013;168(9):563-568. doi:10.1016/j.micres.2013.04.009

17. Baracos V, Bauer J, Bhasin S, et al. Sarcopenia With Limited Mobility: An International Consensus John. *J Am Med Dir Assoc*. 2016;12(6):403-409. doi:10.1016/j.jamda.2011.04.014.Sarcopenia

18. Mathews SM, Spallholz JE, Grimson MJ, Dubielzig RR, Gray T, Reid TW. Prevention of bacterial colonization of contact lenses with covalently attached selenium and effects

on the rabbit cornea. *Cornea*. 2006;25(7):806-814. doi:10.1097/01.ico.0000224636.57062.90

19. Plano D, Baquedano Y, Moreno-Mateos D, et al. Selenocyanates and diselenides: A new class of potent antileishmanial agents. *Eur J Med Chem*. 2011;46(8):3315-3323. doi:10.1016/j.ejmech.2011.04.054

20. Tentori L, Prete SP, Pepponi R. Effects of diheptyldiselenide (DDS) on human tumor cell lines and on peripheral blood mononuclear cells. *J Chemother*. 1993;5(5):325-333. doi:10.1080/1120009X.1993.11741078

21. Kumar R, Tuck DG. The direct electrochemical synthesis of phenylselenolato complexes of some main group and late transition elements. *Can J Chem*. 1989;67(1):127-129. doi:10.1139/v89-021

22. Klauke K, Hahn B, Schütte K, Barthel J, Janiak C. Nano-Structures & Nano-Objects Bis ((dialkylamino) alkylselenolato) metal complexes as precursors for microwave-assisted synthesis of semiconductor metal selenide nanoparticles of zinc and cadmium in the ionic liquid [BMIm][BF 4]. *Nano-Structures & Nano-Objects*. 2015;1:24-31. doi:10.1016/j.nanoso.2015.06.001

23. Rastogi R, Srivastava SK, Asolia S, Butcher RJ. Synthesis , Spectral Characterization and Ligation of N - [2- (Phenylseleno) ethyl] phthalimide. 2013;2013(January):31-35.

24. Kampf J, Kumar R, Oliver JP. Electrochemical Synthesis and the Molecular Structure of a Benzeneselenolato Complex of Copper, Ph3PCu(μ-SePh)2Cu(PPh3)2.CH3CN, Containing Both Three- and Four-Coordinate Copper. *Inorg Chem*. 1992;31(17):3626-3629.

25. Lobana TS, Hundal R, Turner P. Metal-Selenium Interactions. Synthesis and Crystal Structure of [Diiodo{1,1′-Methylene-Bis (Diphenyl Phosphine Selenide)}] Zinc(Ii). *J Coord Chem*. 2001;53(4):301-309. doi:10.1080/00958970108022616

26. Al-majthoub MM, Salman M. Infrared spectroscopic interpretations on the reaction products resulted from the interaction between Co (II), Cu (II), Fe (III), Mn (II), Ni (II) and Zn (II) phosphate salts with urea at 85 o C. *J Chem Pharm Res*. 2012;4(3):1856-1863.

27. Ibrahim OB. Complexes of urea with Mn (II), Fe (III), Co (II), and Cu (II) metal ions. *Adv Appl Sci Res*. 2012;3(6):3522-3539.

28. Ibrahim OB, Refat MS, Salman M. Chemical Studies on the Uses of Urea Complexes to Synthesize Compounds Having Electrical and Biological Applications. *Int J Mater Sci*. 2012;2(3):67-82.

29. George S, Chellapandian M, Sivasankar B, Jayaraman K. A new process for the treatment of fertilizer effluent using immobilized urease. *Bioprocess Eng*. 1997;16(2):83-85. doi:10.1007/s004490050292

30. Gnewuch CT, Sosnovsky G. A critical appraisal of the evolution of N-nitrosoureas as anticancer drugs. *Chem Rev*. 1997;97(3):829-1014. doi:10.1021/cr941192h

31. Harvey PD. Structural and spectroscopic of metal-urea complexes. 1987;76:237-264.

32. Vaughan P, Donohue J. The Structure of Urea. Interatomic Distances and Resonance in Urea and Related Compounds. *Acta Crystallogr, Sect A Found Crystallogr*. 1952;5(c):530-535. doi:10.1107/S0365110X52001477

33. Pauling L, Brockway LO, Beach JY. The Dependence of Interatomic Distance on Single Bond-Double Bond Resonance. *J Am Chem Soc*. 1935;57(12):2705-2709. doi:10.1021/ja01315a105

34. Kumler WD, Fohlen GM. The Dipole Moment and Structure of Urea and Thiourea. *J Am Chem Soc*. 1942;64(8):1944-1948. doi:10.1021/ja01260a054

35. Caron A, Donohue J. Redetermination of Thermal Motion and Interatomic Distances in Urea. *Acta Crystallogr, Sect B Struct Sci*. 1969;25:404. doi:10.1107/S0567740869002330

36. Kellner L. The Vibrations and the Molecular Structure of Urea and Guanidonium. *Proc R Soc A Math Phys Eng Sci*. 1941;177(971):456-475. doi:10.1098/rspa.1941.0035

37. Megahed AS, Ibrahim OB, Adam AMA, Al-Majthoub MM. Synthesis and structural characterization of urea metal complexes with Cu(II), Zn(II), Ag(I), Cd(II) and Hg(II) ions at high temperature. *Int J Chem Sci*. 2014;12(2):335-343.

38. Ibrahim OB, Refat MS, Salman M, Al-majthoub MM. Chemical Studies on the Uses of

Urea Complexes to Synthesize Compounds Having Electrical and Biological Applications. *Int J Mater Sci*. 2012;2(3):67-82.

39. Drakopoulou L, Raptopoulou CP, Terzis A, Papaefstathiou GS. Hydrogen-Bonded Networks Based on Cobalt(II), Nickel(II), and Zinc(II) Complexes of N,N'-Diethylurea. *Bioinorg Chem Appl*. 2010;2010:1-12. doi:10.1155/2010/618202

40. Sagatys DS, Bott RC, Smith G, Byriel KA, Kennard CHL. The preparation and crystal structure of a polymeric (1 : 1)-silver nitrate-urea complex, [(AgNO3)2(CH4N2O)2]n. *Polyhedron*. 1992;11(1):49-52. doi:10.1016/S0277-5387(00)83258-1

41. Lines MG. Nanomaterials for practical functional uses. *J Alloys Compd*. 2008;449(1-2):242-245. doi:10.1016/j.jallcom.2006.02.082

42. Rao CNR, Kulkarni GU, John Thomas P, Edwards PP. Size-dependent chemistry: Properties of nanocrystals. *ChemEurJ*. 2002;8(1):28-35.

43. Caruso F. *Front Matter*. Vol 14.; 2005. doi:10.1002/3527603824.fmatter

44. Ma D, Zhang M, Xi G, Zhang J, Qian Y. Fabrication and Characterization of Ultralong Ag / C Nanocables , Carbonaceous Nanotubes , and Chainlike -Ag 2 Se Nanorods inside Carbonaceous Nanotubes. *Society*. 2006;45(12):4845-4849.

45. Brus LE. Electron–electron and electron-hole interactions in small semiconductor crystallites: The size dependence of the lowest excited electronic state. *J Chem Phys*. 1984;80(9):4403. doi:10.1063/1.447218

46. Brus LE. A simple model for the ionization potential, electron affinity, and aqueous redox potentials of small semiconductor crystallites. *J Chem Phys*. 1983;79(1983):5566. doi:10.1063/1.445676

47. Zhang JZ. Ultrafast Studies of Electron Dynamics in Semiconductor and Metal Colloidal Nanoparticles: Effects of Size and Surface. *Acc Chem Res*. 1997;30(10):423-429. doi:10.1021/ar960178j

48. Jesson DA, Watts JF. The Interface and Interphase in Polymer Matrix Composites: Effect on Mechanical Properties and Methods for Identification. *Polym Rev*. 2012;52(3-4):321-354. doi:10.1080/15583724.2012.710288

49. Branagan DJ, Tang Y. Developing extreme hardness (. 15 GPa) in iron based nanocomposites. *Society*. 2002;33:855-859.

50. Choa YH, Yang JK, Kim BH, et al. Preparation and characterization of metal/ceramic nanoporous nanocomposite powders. *J Magn Magn Mater*. 2003;266(1-2):12-19. doi:10.1016/S0304-8853(03)00450-5

51. Henrique P, Camargo C, Satyanarayana KG, Wypych F. Nanocomposites : Synthesis , Structure , Properties and New Application Opportunities. 2009;12(1):1-39.

52. Atchison JS, Schauer CL. Fabrication and characterization of electrospun semiconductor nanoparticle-polyelectrolyte ultra-fine fiber composites for sensing applications. *Sensors (Basel)*. 2011;11(11):10372-10387. doi:10.3390/s111110372

53. Bompilwar SD, Kondawar SB, Tabhane VA, Snehal R. Thermal stability of CdS / ZnS nanoparticles embedded conducting polyaniline nanocomposites. 2010;1(1):166-173.

54. Folarin OM, Sadiku ER, Maity A. Polymer-noble metal nanocomposites: Review. *Int J Phys Sci*. 2011;6(21):4869-4882. doi:10.5897/IJPS11.570

55. Khalil KA, Eltaleb H, Abdo HS, Al-Deyab SS, Fouad H. Carbon Nanofibers Containing Ag/TiO2 Composites as a Preliminary Stage for CDI Technology. *J Mater Sci Chem Eng*. 2014;02(01):31-37. doi:10.4236/msce.2014.21006

56. Bakis CE, Bank LC, Brown VL, et al. Fiber-reinforced polymer composites for construction - State-of-the-art review. *J Compos Constr*. 2002;6(2):73-87. doi:10.1061/(ASCE)1090-0268(2002)6:2(73)

57. Zamri MFA, Zein SHS, Abdullah AZ, Basir NI. Improved electrical conductivity of polyvinyl alcohol / multiwalled carbon nanotube nanofibre composite films with MnO2 as filler synthesised using the electrospinning process. *Int J Eng Technol*. 2011;11(6):20-26.

58. Yao J, Bastiaansen CWM, Peijs T. High Strength and High Modulus Electrospun Nanofibers. *Fibers*. 2014;2(2):158-187. doi:10.3390/fib2020158

59. Khalil KA, Fouad H, Elsarnagawy T, Almajhdi FN. Preparation and characterization of electrospun PLGA/silver composite nanofibers for biomedical applications. *Int J Electrochem Sci*. 2013;8(3):3483-3493.

60. Zhu J, Wei S, Rutman D, Haldolaarachchige N, Young DP, Guo Z. Magnetic polyacrylonitrile-Fe@FeO nanocomposite fibers - Electrospinning, stabilization and carbonization. *Polymer (Guildf)*. 2011;52(13):2947-2955. doi:10.1016/j.polymer.2011.04.034

61. Vaia RA, Wagner HD. Framework for nanocomposites. *Mater Today*. 2004;7(11):32-37. doi:10.1016/S1369-7021(04)00506-1

62. Qian Y, Su Y, Li X, Wang H, He C. Electrospinning of Polymethyl Methacrylate Nanofibres in Different Solvents. *Iran Polym J*. 2010;19(2):123-129.

63. Li D, Xia Y. Electrospinning of nanofibers: Reinventing the wheel? *Adv Mater*. 2004;16(14):1151-1170. doi:10.1002/adma.200400719

64. Karakas H. Electrospinning of Nanofibers and Their Applications. 2014;3:126-131.

65. Bhardwaj N, Kundu SC. Electrospinning: A fascinating fiber fabrication technique. *Biotechnol Adv*. 2010;28(3):325-347. doi:10.1016/j.biotechadv.2010.01.004

66. Koski A, Yim K, Shivkumar S. Effect of molecular weight on fibrous PVA produced by electrospinning. *Mater Lett*. 2004;58(3-4):493-497. doi:10.1016/S0167-577X(03)00532-9

67. Akduman Ç, Kumabasar EPA, Çay A. Effect of molecular weight on the morphology of electrospun poly (vinyl alcohol) nanofibers. In: *XIIIth International Izmir Textile and Apparel Symposium*. ; 2014:127-134.

68. Haider S, Al-Zeghayer Y, Ahmed Ali FA, et al. Highly aligned narrow diameter chitosan electrospun nanofibers. *J Polym Res*. 2013;20(4). doi:10.1007/s10965-013-0105-9

69. Haider A, Haider S, Kang I. A comprehensive review summarizing the effect of electrospinning parameters and potential applications of nanofibers in biomedical and biotechnology. *Arab J Chem*. 2015;11(8):1165-1188. http://dx.doi.org/10.1016/j.arabjc.2015.11.015.

70. James CM. Assessment of Electrospinning as an In-House Fabrication Technique for Blood Vessel Mimic Cellular Scaffolding. 2009;(August).

71. Zargham S, Bazgir S, Tavakoli A, Rashidi AS, Damerchely R. The Effect of Flow Rate

on Morphology and Deposition Area of Electrospun Nylon 6 Nanofiber. *J Eng Fiber Fabr*. 2012;7(4):42-49.

72. Fong H, Fong H, Chun I, Chun I, Reneker D, Reneker D. Beaded nano bers formed during electrospinning. *Polymer (Guildf)*. 1999;40:4585-4592.

73. Pillay V, Dott C, Choonara YE, et al. A Review of the Effect of Processing Variables on the Fabrication of Electrospun Nanofibers for Drug Delivery Applications. 2013;2013:22. doi:10.1155/2013/789289

74. Sill TJ, von Recum HA. Electrospinning: Applications in drug delivery and tissue engineering. *Biomaterials*. 2008;29(13):1989-2006. doi:10.1016/j.biomaterials.2008.01.011

75. Smith LA, Ma PX. Nano-fibrous scaffolds for tissue engineering. *Colloids Surfaces B Biointerfaces*. 2004;39(3):125-131. doi:10.1016/j.colsurfb.2003.12.004

76. Garg K, Bowlin GL. Electrospinning jets and nanofibrous structures. *Biomicrofluidics*. 2011;5(1). doi:10.1063/1.3567097

77. Sun B, Long YZ, Zhang HD, et al. Advances in three-dimensional nanofibrous macrostructures via electrospinning. *Prog Polym Sci*. 2014;39(5):862-890. doi:10.1016/j.progpolymsci.2013.06.002

78. Zong X, Kim K, Fang D, Ran S, Hsiao BS, Chu B. Structure and process relationship of electrospun bioabsorbable nanofiber membranes. *Polymer (Guildf)*. 2002;43:4403-4412. doi:10.1016/S0032-3861(02)00275-6

79. Jung YH, Kim HY, Lee DR, Park SY, Khil MS. Characterization of PVOH nonwoven mats prepared from surfactant-polymer system via electrospinning. *Macromol Res*. 2005;13(5):385-390. doi:10.1007/BF03218470

80. Zeng J, Xu X, Chen X, et al. Biodegradable electrospun fibers for drug delivery. *J Control Release*. 2003;92(3):227-231. doi:10.1016/S0168-3659(03)00372-9

81. Yang Q, Zhenyu LI, Hong Y, et al. Influence of solvents on the formation of ultrathin uniform poly(vinyl pyrrolidone) nanofibers with electrospinning. *J Polym Sci Part B Polym Phys*. 2004;42(20):3721-3726. doi:10.1002/polb.20222

82. Reneker JD and DH. Journal of. *J Electrostat*. 1995;35:151-160. doi:10.1111/joa.12037

83. Helmlinger J, Prymak O, Loza K, Gocyla M, Heggen M, Epple M. On the Crystallography of Silver Nanoparticles with Different Shapes. *Cryst Growth Des*. 2016;16(7):3677-3687. doi:10.1021/acs.cgd.6b00178

84. Zeleny J. The role of surface instability in electrical discharges from drops of alcohol and water in air at atmospheric pressure. *J Franklin Inst*. 1935;219(6):659-675.

85. Megelski S, S.Stephens J, Chase DB, F.Rabolt J. Micro-and Nanostructured Surface Morphology on Electrospum Polymer Fibers. *Macromolecules*. 2002;35(22):8456-8466. doi:10.1021/ma020444a

86. Matabola KP, Moutloali RM. The influence of electrospinning parameters on the morphology and diameter of poly(vinyledene fluoride) nanofibers- Effect of sodium chloride. *J Mater Sci*. 2013;48(16):5475-5482. doi:10.1007/s10853-013-7341-6

87. Ghelich R, Rad MK, Youzbashi AA. Study on morphology and size distribution of electrospun NiO-GDC composite nanofibers. *J Eng Fiber Fabr*. 2015;10(1):12-19.

88. Wang T, Kumar S. Electrospinning of polyacrylonitrile nanofibers. *J Appl Polym Sci*. 2006;102(2):1023-1029. doi:10.1002/app.24123

89. Ziabari M, Mottaghitalab V, Haghi AK. A new approach for optimization of electrospun nanofiber formation process. *Korean J Chem Eng*. 2010;27(1):340-354. doi:10.1007/s11814-009-0309-1

90. Zhang C, Yuan X, Wu L, Han Y, Sheng J. Study on morphology of electrospun poly(vinyl alcohol) mats. *Eur Polym J*. 2005;41(3):423-432. doi:10.1016/j.eurpolymj.2004.10.027

91. Huan S, Liu G, Han G, et al. Effect of Experimental Parameters on Morphological, Mechanical and Hydrophobic Properties of Electrospun Polystyrene Fibers. *Materials (Basel)*. 2015;8(5):2718-2734. doi:10.3390/ma8052718

92. Pelipenko J, Kristl J, Janković B, Baumgartner S, Kocbek P. The impact of relative humidity during electrospinning on the morphology and mechanical properties of nanofibers. *Int J Pharm*. 2013;456:125-134. doi:10.1016/j.ijpharm.2013.07.078

93. De Vrieze S, Van Camp T, Nelvig A, Hagström B, Westbroek P, De Clerck K. The effect of temperature and humidity on electrospinning. *J Mater Sci*. 2009;44(5):1357-1362. doi:10.1007/s10853-008-3010-6

94. Jeun J-P, Kim Y-H, Lim Y-M, et al. Electrospinning of Poly (L-lactide-co-D , L-lactide). *J Ind Eng Chem*. 2007;13(4):592-596.

95. Medeiros ES, Mattoso LHC, Offeman RD, Wood DF, Orts WJ. Effect of relative humidity on the morphology of electrospun polymer fibers. *Can J Chem*. 2008;86(6):590-599. doi:10.1139/v08-029

96. Bae HS, Haider A, Selim KMK, Kang DY, Kim EJ, Kang IK. Fabrication of highly porous PMMA electrospun fibers and their application in the removal of phenol and iodine. *J Polym Res*. 2013;20(7). doi:10.1007/s10965-013-0158-9

97. Chen HM, Yu DG. An elevated temperature electrospinning process for preparing acyclovir-loaded PAN ultrafine fibers. *J Mater Process Technol*. 2010;210(12):1551-1555. doi:10.1016/j.jmatprotec.2010.05.001

98. Desai K, Kit K. Effect of spinning temperature and blend ratios on electrospun chitosan/poly(acrylamide) blends fibers. *Polymer (Guildf)*. 2008;49(19):4046-4050. doi:10.1016/j.polymer.2008.07.012

99. Um IC, Fang D, Hsiao BS, Okamoto A, Chu B. Electro-spinning and electro-blowing of hyaluronic acid. *Biomacromolecules*. 2004;5(4):1428-1436. doi:10.1021/bm034539b

100. Yang G-Z, Li H-P, Yang J-H, Wan J, Yu D-G. Influence of Working Temperature on The Formation of Electrospun Polymer Nanofibers. *Nanoscale Res Lett*. 2017;12(1):55. doi:10.1186/s11671-016-1824-8

101. Kim CH, Jung YH, Kim HY, Lee DR, Dharmaraj N, Choi KE. Effect of collector temperature on the porous structure of electrospun fibers. *Macromol Res*. 2006;14(1):59-65. doi:10.1007/BF03219069

102. Wang B, Wang Y, Yin T, Yu Q. Applications of Electrospinning Technique in Drug Delivery. *Chem Eng Commun*. 2010;197(10):1315-1338. doi:10.1080/00986441003625997

103. Buschle-Diller G, Cooper J, Xie Z, Wu Y, Waldrup J, Ren X. Release of antibiotics from

electrospun bicomponent fibers. *Cellulose*. 2007;14(6):553-562. doi:10.1007/s10570-007-9183-3

104. Ranganath SH, Wang CH. Biodegradable microfiber implants delivering paclitaxel for post-surgical chemotherapy against malignant glioma. *Biomaterials*. 2008;29(20):2996-3003. doi:10.1016/j.biomaterials.2008.04.002

105. Chew SY, Wen J, Yim EKF, Leong KW. Sustained release of proteins from electrospun biodegradable fibers. *Biomacromolecules*. 2005;6(4):2017-2024. doi:10.1021/bm0501149

106. Liang D, Luu YK, Kim K, Hsiao BS, Hadjiargyrou M, Chu B. In vitro non-viral gene delivery with nanofibrous scaffolds. *Nucleic Acids Res*. 2005;33(19):1-10. doi:10.1093/nar/gni171

107. Kenawy ER, Bowlin GL, Mansfield K, et al. electrospun poly(ethylene-co-vinylacetate), poly(lactic acid), and a blendRelease of tetracycline hydrochloride from. *J Control Release*. 2002;81(1-2):57-64. doi:10.1016/S0168-3659(02)00041-X

108. Liao S, Li B, Ma Z, Wei H, Chan C, Ramakrishna S. Biomimetic electrospun nanofibers for tissue regeneration. *Biomed Mater*. 2006;1(3):R45-R53. doi:10.1088/1748-6041/1/3/R01

109. Qiu R-X, Li C-M, Ye L, et al. Electrospinning of synthesized triblock copolymers of epsilon-caprolactone and L-lactide for the application of vascular tissue engineering. *Biomed Mater*. 2009;4(4):044105. doi:10.1088/1748-6041/4/4/044105

110. Ma Z, Kotaki M, Yong T, He W, Ramakrishna S. Surface engineering of electrospun polyethylene terephthalate (PET) nanofibers towards development of a new material for blood vessel engineering. *Biomaterials*. 2005;26(15):2527-2536. doi:10.1016/j.biomaterials.2004.07.026

111. Zhu X, Cui W, Li X, Jin Y. Electrospun Fibrous Mats with High Porosity as Potential. *Biomacromolecules*. 2008;9:1795-1801. doi:10.1021/bm800476u

112. Chen JP, Chang GY, Chen JK. Electrospun collagen/chitosan nanofibrous membrane as wound dressing. *Colloids Surfaces A Physicochem Eng Asp*. 2008;313-314:183-188. doi:10.1016/j.colsurfa.2007.04.129

113. Prabhakaran MP, Venugopal J, Chan CK, Ramakrishna S. Surface modified electrospun nanofibrous scaffolds for nerve tissue engineering. *Nanotechnology*. 2008;19(45):1-8. doi:10.1088/0957-4484/19/45/455102

114. Kim HW, Kim HE. Nanofiber generation of hydroxyapatite and fluor-hydroxyapatite bioceramics. *J Biomed Mater Res - Part B Appl Biomater*. 2006;77(2):323-328. doi:10.1002/jbm.b.30376

115. Sahoo S, Ouyang H, Goh JC-H, Tay TE, Toh SL. Characterization of a Novel Polymeric Scaffold for Potential Application in Tendon/Ligament Tissue Engineering. *Tissue Eng*. 2006;12(1):91-99. doi:10.1089/ten.2006.12.ft-8

116. Palza H. Antimicrobial polymers with metal nanoparticles. *Int J Mol Sci*. 2015;16(1):2099-2116. doi:10.3390/ijms16012099

117. Jin W-J, Lee HK, Jeong EH, Park WH, Youk JH. Preparation of Polymer Nanofibers Containing Silver Nanoparticles by Using Poly(N-vinylpyrrolidone). *Macromol Rapid Commun*. 2005;26(24):1903-1907. doi:10.1002/marc.200500569

118. Son WK, Youk JH, Lee TS, Park WH. Preparation of antimicrobial ultrafine cellulose acetate fibers with silver nanoparticles. *Macromol Rapid Commun*. 2004;25(18):1632-1637. doi:10.1002/marc.200400323

119. Melaiye A, Sun Z, Hindi K, et al. Silver(I)-imidazole cyclophane gem-diol complexes encapsulated by electrospun tecophilic nanofibers: Formation of nanosilver particles and antimicrobial activity. *J Am Chem Soc*. 2005;127(7):2285-2291. doi:10.1021/ja040226s

120. Xie Z. Biomedical Materials Based on Electrospun Polymeric Fibers. 2010.

121. Gopal R, Kaur S, Feng CY, et al. Electrospun nanofibrous polysulfone membranes as pre-filters: Particulate removal. *J Memb Sci*. 2007;289(1-2):210-219. doi:10.1016/j.memsci.2006.11.056

122. Wang X, Chen X, Yoon K, Fang D, Hsiao BS, Chu B. High flux filtration medium based on nanofibrous substrate with hydrophilic nanocomposite coating. *Environ Sci Technol*. 2005;39(19):7684-7691. doi:10.1021/es050512j

123. Yoon K, Kim K, Wang X, Fang D, Hsiao BS, Chu B. High flux ultrafiltration membranes based on electrospun nanofibrous PAN scaffolds and chitosan coating.

Polymer (Guildf). 2006;47(7):2434-2441. doi:10.1016/j.polymer.2006.01.042

124. Ma M, Gupta M, Li Z, et al. Decorated electrospun fibers exhibiting superhydrophobicity. *Adv Mater*. 2007;19(2):255-259. doi:10.1002/adma.200601449

125. Han D, Steckl AJ. Superhydrophobic and oleophobic fibers by coaxial electrospinning. *Langmuir*. 2009;25(16):9454-9462. doi:10.1021/la900660v

126. Kaushik A, Kumar R, Arya SK, Nair M, Malhotra BD, Bhansali S. Nanostructured Gas Sensors for Health Care: An Overview. *J Pers NanoMedicine Rev*. 2015;1(1):4571-4606. doi:10.1021/cr400659h

127. Kessick R, Tepper G. Electrospun polymer composite fiber arrays for the detection and identification of volatile organic compounds. *Sensors Actuators, B Chem*. 2006;117(1):205-210. doi:10.1016/j.snb.2005.11.045

128. Yoon J, Jung YS, Kim JM. A combinatorial approach for colorimetric differentiation of organic solvents based on conjugated polymer-embedded electrospun fibers. *Adv Funct Mater*. 2009;19(2):209-214. doi:10.1002/adfm.200800963

129. Kowalczyk T, Nowicka A, Elbaum D, Kowalewski TA. Electrospinning of bovine serum albumin optimization and the use for production of biosensors. *Biomacromolecules*. 2008;9(7):2087-2090. doi:10.1021/bm800421s

130. Wang W, Huang H, Li Z, et al. Zinc oxide nanofiber gas sensors via electrospinning. *J Am Ceram Soc*. 2008;91(11):3817-3819. doi:10.1111/j.1551-2916.2008.02765.x

131. Kim H, Choi Y, Kanuka N, Kinoshita H, Nishiyama T, Usami T. Preparation of Pt-loaded TiO2 nanofibers by electrospinning and their application for WGS reactions. *Appl Catal A Gen*. 2009;352(1-2):265-270. doi:10.1016/j.apcata.2008.10.016

132. Xu X, Wang Q, Choi HC, Kim YH. Encapsulation of iron nanoparticles with PVP nanofibrous membranes to maintain their catalytic activity. *J Memb Sci*. 2010;348(1-2):231-237. doi:10.1016/j.memsci.2009.11.006

133. Zhang R, Wu H, Lin DD, Pan W. Photocatalytic and Magnetic Properties of the Fe-TiO2/SnO2 Nanofiber Via Electrospinning. *J Am Ceram Soc*. 2010;93(3):605-608. doi:DOI 10.1111/j.1551-2916.2009.03456.x

134. Sakai S, Yamaguchi T, Watanabe R, Kawabe M, Kawakami K. Enhanced catalytic activity of lipase in situ encapsulated in electrospun polystyrene fibers by subsequent water supply. *Catal Commun*. 2010;11(6):576-580. doi:10.1016/j.catcom.2009.12.023

135. Zhao L, Chu PK, Zhang Y, Wu Z. Antibacterial coatings on titanium implants. *J Biomed Mater Res - Part B Appl Biomater*. 2009;91(1):470-480. doi:10.1002/jbm.b.31463

136. Silver S, Phung LT, Silver G. Silver as biocides in burn and wound dressings and bacterial resistance to silver compounds. *J Ind Microbiol Biotechnol*. 2006;33(7):627-634. doi:10.1007/s10295-006-0139-7

137. Klassen HJ. A historical review of the use of silver in the treatment of burns. *Burns*. 2000;26_ _:117-130. doi:http://dx.doi.org/10.1016/S0305-4179(99)00116-3

138. Samuel U, Guggenbichler JP. Prevention of catheter-related infections: The potential of a new nano-silver impregnated catheter. *Int J Antimicrob Agents*. 2004;23(SUPPL. 1):75-78. doi:10.1016/j.ijantimicag.2003.12.004

139. Rupp ME, Fitzgerald T, Marion N, et al. Effect of silver-coated urinary catheters: Efficacy, cost-effectiveness, and antimicrobial resistance. *Am J Infect Control*. 2004;32(8):445-450. doi:10.1016/j.ajic.2004.05.002

140. Bosetti M, Massè A, Tobin E, Cannas M. Silver Coated Materials for External Fixation Devices : In-vitro Biocompatibility and Genotoxicity Silver coated materials for external fixation devices : in vitro biocompatibility and genotoxicity. *Biomaterials*. 2002;23(MARCH):887-892. doi:10.1016/S0142-9612(01)00198-3

141. Zhanjiang Z, Jinpei L. Synthesis and Characterization of Silver Nanoparticles by a Sonochemical Method. *Rare Met Mater Eng*. 2012;41(10):1700-1705. doi:10.1016/S1875-5372(13)60008-9

142. Cheng Y, Yan M, Jiang Z. Electrochemical Behavior and Reduction Mechanism of High Valence Silver Oxide in Alkaline Solution. *Electrochem Solid-State Lett*. 2007;10(3):F5. doi:10.1149/1.2422752

143. Ahmadi SJ, Outokesh M, Hosseinpour M, Mousavand T. A simple granulation technique for preparing high-porosity nano copper oxide(II) catalyst beads. *Particuology*. 2011;9(5):480-485. doi:10.1016/j.partic.2011.02.010

144. Khan SB, Chani MTS, Karimov KS, Asiri AM, Bashir M, Tariq R. Humidity and temperature sensing properties of copper oxide-Si-adhesive nanocomposite. *Talanta*. 2014;120:443-449. doi:10.1016/j.talanta.2013.11.089

145. Jin Y, Dai Z, Liu F, Kim H, Tong M, Hou Y. Bactericidal mechanisms of Ag2O/TNBs under both dark and light conditions. *Water Res*. 2013;47(5):1837-1847. doi:10.1016/j.watres.2013.01.003

146. Tselepis E, Fortin E. Preparation and photovoltaic properties of anodically grown Ag2O films. *J Mater Sci*. 1986;21(3):985-988. doi:10.1007/BF01117383

147. Her YC, Lan YC, Hsu WC, Tsai SY. Effect of constituent phases of reactively sputtered AgOx film on recording and readout mechanisms of super-resolution near-field structure disk. *J Appl Phys*. 2004;96(3):1283-1288. doi:10.1063/1.1767978

148. Tominaga J. The application of silver oxide thin films to plasmon photonic devices. *J Phys Condens Matter*. 2003;15(25):R1101-R1122. doi:10.1088/0953-8984/15/25/201

149. Fu HT, Zhao LM, Luo M, Zhang HY, Zhang J. Determination of chloracetic acids in drinking water by ion chromatography using silver oxide as precipitant eliminating interference of chlorate in matrix. *Fenxi Huaxue/ Chinese J Anal Chem*. 2008;36(10):1407-1410. doi:10.1016/S1872-2040(08)60076-6

150. Ananth A, Dharaneedharan S, Heo MS, Mok YS. Copper oxide nanomaterials: Synthesis, characterization and structure-specific antibacterial performance. *Chem Eng J*. 2015;262:179-188. doi:10.1016/j.cej.2014.09.083

151. Ge JP, Xu S, Liu LP, Li YD. A positive-microemulsion method for preparing nearly uniform Ag 2Se nanoparticles at low temperature. *Chem - A Eur J*. 2006;12(13):3672-3677. doi:10.1002/chem.200600006

152. Das VD, Karunakaran D. Variations of energy gap, resistivity, and temperature coefficient of resistivity in annealed -Ag2Se thin films. *Phys Rev B*. 1989;39(15):10872-10878. doi:10.1103/PhysRevB.39.10872

153. Glanville YJ, Narehood DG, Sokol PE, Amma a., Mallouk T. Preparation and synthesis of Ag2Se nanowires produced by template directed synthesis. *J Mater Chem*. 2002;12(8):2433-2434. doi:10.1039/b202913h

154. Ng MT, Boothroyd C, Vittal JJ. Shape and size control of Ag2Se nanocrystals from a single precursor [(Ph3P)3Ag2(SeC{O}Ph)2]. *Chem Commun (Camb)*. 2005;2(30):3820-3822. doi:10.1039/b506203a

155. Cui Y, Chen G, Ren J, Shao M, Xie Y, Qian Y. Solvothermal syntheses of b-Ag2Se crystals with novel morphologies. *J Solid State Chem*. 2003;172(1):17-21. doi:10.1016/S0022-4596(02)00040-3

156. Parish MM, Littlewood PB. Non-saturating magnetoresistance in heavily disordered semiconductors. *Nature*. 2003;426(September):162-165. doi:10.1038/nature02073

157. Xu R, Husmann a, Rosenbaum TF, Saboungi ML, Enderby JE, Littlewood PB. Large magnetoresistance in non-magnetic silver chalcogenides. *Nature*. 1997;390(6655):57-60. doi:10.1038/36306

158. Borkow G, Gabbay J. Copper, An Ancient Remedy Returning to Fight Microbial, Fungal and Viral Infections. *Curr Chem Biol*. 2009;3(3):272-278. doi:10.2174/187231309789054887

159. Wong TKS, Zhuk S, Masudy-Panah S, Dalapati GK. Current status and future prospects of copper oxide heterojunction solar cells. *Materials (Basel)*. 2016;9(4):1-21. doi:10.3390/ma9040271

160. Chiang C-Y, Shin Y, Ehrman S. Dopant Effects on Copper Oxide Photoelectrochemical Cell Water Splitting. *Energy Procedia*. 2014;61:1799-1802. doi:10.1016/j.egypro.2014.12.216

161. Jiang T, Wang Y, Meng D, Wu X, Wang J, Chen J. Controllable fabrication of CuO nanostructure by hydrothermal method and its properties. *Appl Surf Sci*. 2014;311:602-608. doi:10.1016/j.apsusc.2014.05.116

162. Sivaraj R, Rahman PKSM, Rajiv P, Narendhran S, Venckatesh R. Biosynthesis and characterization of Acalypha indica mediated copper oxide nanoparticles and evaluation of its antimicrobial and anticancer activity. *Spectrochim Acta Part A Mol Biomol Spectrosc*. 2014;129:255-258. doi:10.1016/j.saa.2014.03.027

163. Patidar D, Saxena NS. Characterization of single phase copper selenide nanoparticles and their growth mechanism. *J Cryst Growth*. 2012;343(1):68-72.

doi:10.1016/j.jcrysgro.2012.01.026

164. Garcia VM, Nair PK, Nair MTS. Copper selenide thin films by chemical bath deposition. *J Cryst Growth*. 1999;203:113-124.

165. Bhuse VM, Hankare PP, Garadkar KM, Khomane AS. A simple , convenient , low temperature route to grow polycrystalline copper selenide thin films. *Mater Chem Phys*. 2003;80:82-88.

166. Yu WW, Chang E, Sayes CM, Drezek R, Colvin VL. Aqueous dispersion of monodisperse magnetic iron oxide nanocrystals through phase transfer. *Nanotechnology*. 2006;17(17):4483-4487. doi:10.1088/0957-4484/17/17/033

167. Wu W, Wu Z, Yu T, Jiang C, Kim W-S. Recent progress on magnetic iron oxide nanoparticles: synthesis, surface functional strategies and biomedical applications. *Sci Technol Adv Mater*. 2015;16(2):1-43. doi:10.1088/1468-6996/16/2/023501

168. Sutka A, Lagzdina S, Juhnevica I, Jakovlevs D, Maiorov M. Precipitation synthesis of magnetite Fe3O4 nanoflakes. *Ceram Int*. 2014;40(7 PART B):11437-11440. doi:10.1016/j.ceramint.2014.03.140

169. Hasany SF, Rehman A, Jose R, Ahmed I. Iron oxide magnetic nanoparticles: A short review. *AIP Conf Proc*. 2012;1502(1):298-321. doi:10.1063/1.4769153

170. Hsu F-C, Luo J-Y, Yeh K-W, et al. Superconductivity in the PbO-type structure α-FeSe. *Proc Natl Acad Sci*. 2008;105(38):14262-14264. doi:10.1073/pnas.0807325105

171. Akhtar M, Malik MA, Raftery J, O'Brien P. Synthesis of iron selenide nanocrystals and thin films from bis (tetraisopropyldiselenoimidodiphosphinato) iron (II and bis (tetraphenyldiselenoimidodiphosphinato) iron (II) complexes. *J Mater Chem A*. 2014;2:20612-20620. doi:10.1039/C4TA04054F

172. Akhtar M. Synthesis of Iron Chalcogenide Nanocrystals and Deposition of Thin Films from Single Source Precursors. *Sch Chem Univ Manchester*. 2013.

173. Wu XJ, Zhang ZZ, Zhang JY, et al. Two-carrier transport and ferromagnetism in FeSe thin films. *J Appl Phys*. 2008;103(11):1-6. doi:10.1063/1.2936977

174. Wu XJ, Shen DZ, Zhang ZZ, et al. On the nature of the carriers in ferromagnetic FeSe.

Appl Phys Lett. 2007;90(11):88-91. doi:10.1063/1.2712497

175. Ali U, Karim KJBA, Buang NA. A Review of the Properties and Applications of Poly (Methyl Methacrylate) (PMMA). *Polym Rev*. 2015;55:678–705. doi:10.1080/15583724.2015.1031377

176. Ali U, Juhanni K, Abd B, Buang NA. A Review of the Properties and Applications of Poly (Methyl Methacrylate) (PMMA). 2017;3724(June). doi:10.1080/15583724.2015.1031377

177. Walsh EJ. Book & Media Reviews. 2000;77(2):93740.

178. Van Krevelen DW, Te Nijenhuis K. *Properties of Polymers*. Fourth Ed. (Krevelen DW van, Nijenhuis K te, eds.). Amsterdam; 2009. http://www.scopus.com/inward/record.url?eid=2-s2.0-0012576339&partnerID=tZOtx3y1.

179. Henri L. *Thermohygroelastic Properties of Polymethylmethacrylate*.; 2007.

180. Harper CA, Petrie EM. Plastics materials and processes - a concise encyclopedia - Book Review. *IEEE*. 2003. http://ieeexplore.ieee.org/lpdocs/epic03/wrapper.htm?arnumber=1307101.

181. Hashim H, Adam NI, Zaki NHM, et al. Natural Rubber-Grafted With 30 % Poly (Methylmethacrylate) Characterization for Application in Lithium polymer Battery. *IEEE*. 2010:485-488.

182. Ajibade PA, Mbese JZ. Synthesis and Characterization of Metal Sulfides Nanoparticles / Poly (methyl methacrylate) Nanocomposites. 2014;2014.

183. Nussbaumer RJ, Caseri WR, Smith P, Tervoort T. Polymer-TiO2 nanocomposites: A route towards visually transparent broadband UV filters and high refractive index materials. *Macromol Mater Eng*. 2003;288(1):44-49.

184. Chen LS, Huang ZM, Dong GH, et al. Development of a transparent PMMA composite reinforced with nanofibers. *Polym Compos*. 2009;30(3):239-247.

185. Han G, Huan S, Han J, Zhang Z, Wu Q. Effect of acid hydrolysis conditions on the properties of cellulose nanoparticle-reinforced polymethylmethacrylate composites.

Materials (Basel). 2014;7(1):16-29. doi:10.3390/ma7010016

186. Penland RB, Mizushima S, Curran C, Quagliano J V. Infrared Absorption Spectra of Inorganic Coördination Complexes. X. Studies of Some Metal-Urea Complexes 1a,b . *J Am Chem Soc*. 2005;79(7):1575-1578. doi:10.1021/ja01564a014

187. Drakopoulou L, Papatriantafyllopoulou C, Terzis A, Perlepes SP, Manessi-Zoupa E, Papaefstathiou GS. Synthesis, X-ray structure, and characterization of a complex containing the hexakis(urea)cobalt(II) cation and lattice urea molecules. *Bioinorg Chem Appl*. 2007;2007:1-7. doi:10.1155/2007/51567

188. Lin Z, Han D, Li S. Study on thermal decomposition of copper (II) acetate monohydrate in air. *J Therm Anal Calorim*. 2012;107:471-475. doi:10.1007/s10973-011-1454-4

189. Kawaguchi Y, Arakawa R, Kawasaki H. Formate-Free Metal-Organic Decomposition Inks of Copper Particles and Self-Reductive Copper Complex for the Fabrication of Conductive Copper Films. *J Coat Sci Technol*. 2016;3:56-61.

190. Bellini JV, Machado R, Morelli MR, Kiminami RHGA. Thermal , Structural and Morphological Characterisation of Freeze-dried Copper (II) Acetate Monohydrate. *Mater Res*. 2002;5(4):453-457.

191. Obaid AY, Alyoubi AO, Samarkandy AA, Deifallah E-HM. Kinetics of thermal decomposition of copper(II) acetate monohydrate. *J Therm Anal Calorim*. 2000;61:985-994.

192. Mansour SAA. Thermoanalytical investigation of the decomposition course of copper oxysalts - II. Copper (II) nitrate trihydrate. *J Therm Anal*. 1995;45(6):1381-1392. doi:10.1007/BF02547432

193. Fakhri MA, Bader BA, Khalid FG, Mohammed AZ, Shgathi AA. Optical Investigations and Optical Constants of Nano Silver Oxide Prepared By Pld Method. 2018;30(1):33-36.

194. Jain N, Bhargava A, Rathi M, Dilip RV, Panwar J. Removal of protein capping enhances the antibacterial efficiency of biosynthesized silver nanoparticles. *PLoS One*. 2015;10(7):1-19. doi:10.1371/journal.pone.0134337

195. Trivedi MK, Tallapragada RM, Branton A, et al. The Potential Impact of Biofield

Energy Treatment on the Physical and Thermal Properties of Silver Oxide Powder. *Int J Biomed Sci Eng*. 2015;3(5):62-68. doi:10.11648/j.ijbse.20150305.11

196. Pathan HM, Lokhande CD. Deposition of metal chalcogenide thin films by successive ionic layer adsorption and reaction (SILAR) method. *Bull Mater Sci*. 2004;27(2):85-111. doi:10.1007/BF02708491

197. Liu X, Geng B, Du Q, Ma J, Liu X. Temperature-controlled self-assembled synthesis of CuO, Cu2O and Cu nanoparticles through a single-precursor route. *Mater Sci Eng A*. 2007;448(1-2):7-14. doi:10.1016/j.msea.2006.08.104

198. Li D, Qin XY, Liu YF, et al. Chemical synthesis of nanostructured Cu2Se with high thermoelectric performance. *RSC Adv*. 2014;4(17):8638. doi:10.1039/c3ra47015f

199. Martinez AI, Garcia-Lobato MA, Perry DL. Study of the properties of iron oxide nanostructures. In: *Research in Nanotechnology Developments*. ; 2009:183-194.

200. Sharma G, Jeevanandam P. Synthesis of self-assembled prismatic iron oxide nanoparticles by a novel thermal decomposition route. *RSC Adv*. 2013;3(1):189-200. doi:10.1039/c2ra22004k

201. McGrath AJ, Yu C, Fiedler H, Butkus J, Hodgkiss JM, Halpert JE. Dual-Functional Optoelectronic and Magnetic Pyrite/Iron Selenide Core/Shell Nanocrystals. *J Phys Chem C*. 2017;121(14):8220-8226. doi:10.1021/acs.jpcc.7b02643